Power law signatures of cosmic rays, star formation, and interstellar turbulence

Marco Smolla

München 2022

Power law signatures of cosmic rays, star formation, and interstellar turbulence

Marco Smolla

Dissertation
an der Fakultät für Physik
der Ludwig–Maximilians–Universität
München

vorgelegt von
Marco Smolla
aus München

München, den 01.08.2022

Erstgutachter: Prof. Dr. Harald Lesch
Zweitgutachter: Prof. Dr. Jochen Weller
Tag der mündlichen Prüfung: 10. Oktober 2022

Zusammenfassung

Potenzgesetze sind typische Signaturen von komplexen Systemen und in der Astrophysik gibt es zahlreiche Beispiele dafür. Die Ursachen dafür zu ergründen ist eine herausfordernde Aufgabe, für die es unterschiedliche Herangehensweisen gibt. In dieser Dissertation beginne ich mit einer mathematischen Betrachtung von Potenzgesetzen und der definierenden Eigenschaft der Skalen-Invarianz. Für physikalische Systeme ist diese Abwesenheit von charakteristischen Skalen lediglich in einem begrenzten Bereich erfüllt. Durch mehrere Beispiele zeige ich, dass Potenzgesetze als Lösungen von Differenzialgleichungen auftreten können, wobei ihre Gültigkeit üblicherweise durch die Anfangs- und Randbedingungen bestimmt wird. Für die beobachteten Massefunktionen, $\mathrm{d}N/\mathrm{d}M \sim M^{-\alpha}$ mit $\alpha \sim 2$, diskutiere ich ein sehr allgemeingültiges Modell hierarchischer Fragmenation gegenüber einem mehr physikbasierten Modell der Sternentstehung.

Cosmic Rays haben Energieverteilungen welche über viele Größenordnungen durch Potenzgesetze gekennzeichnet sind, im Gegensatz zu den exponentiell abfallenden Verteilungsfunktionen, die in der statistischen Mechanik für Systeme im Gleichgewicht charakteristisch sind. Superstatistics ist eine mögliche Verallgemeinerung der statistischen Mechanik für Nichtgleichgewichts-Systeme. Hier sind die auftretenden Potenzgesetze in den Verteilungsfunktionen das Ergebnis einer Überlagerung von Gleichgewichtsverteilungen mit unterschiedlichen Temperaturen. Ich untersuche die physikalischen Grundlagen dieses Modells, um es auf die beobachteten Energieverteilungen der Cosmic Rays anzuwenden. Dafür ist ein mathematischer Zusammenhang zwischen den beobachteten differentiellen Intensitäten und der aus Superstatistics hergeleiteten Verteilungsfunktion notwendig, was in vorausgehenden Studien fehlerhaft behandelt wurde. Insofern bietet diese Abhandlung eine Verbesserung der theoretischen Grundlagen des Superstatistics-Modells mit Anwendung in der Teilchenphysik. Dieses Modell nutze ich, um damit aus den Beobachtungsdaten von AMS für primäre (He, C, O) und sekundäre (Li, Be, B) Cosmic Rays die besten Fit-Parameter zu bestimmten. Smolla et al. (2020) führen die zwei beobachten Universalitätsklassen an Cosmic Ray Spektren auf die für QCD-Streuprozessen charakteristische Energieskala $\sim 200\,\mathrm{MeV}$ und zwei unterschiedlichen Arten der Überlagerung von Temperaturfluktuationen zurück. Zu den Ergebnissen dieser Arbeit ergänze ich eine kritische Diskussion dieser neuartigen Interpretation und dem Superstatistics-Modell im Allgemeinen.

Interstellare Turbulenz, die initiale Massenverteilung der Sterne, das Sternentstehungsgesetz, und die Ferninfrarot-Radio Korrelation sind Beispiele für nahezu universelle Potenzgesetze, in dem Sinn, dass sie überraschend schwach auf die Variation der detaillierten Parameter des jeweiligen physikalischen Systems reagieren. Ich fasse jeweils die Beobachtungsdaten zusammen und diskutiere physikalische Modelle, um das Auftreten der Potenzgesetze zu erklären. Die Sternentstehung zeigt sich als ein zentraler Treiber hinter all diesen Phänomenen. Ich präsentiere ein neues schematisches Galaxien-Modell, bei dem thermisches Gas, turbulentes Gas, Magnetfelder und Cosmic Rays vergleichbare Energiedichten haben. Die beobachteten Potenzgesetze kennzeichnen die Kopplungen zwischen diesen vier Hauptkomponenten und der Sternentstehung. Aufgrund der Komplexität und der Bandbreite an physikalischen Skalen in unserer Galaxie, ignoriert dieses Modell viele Details absichtlich. Das Ziel ist auf diese Weise die selbstregulierenden Mechanismen aufzudecken, welche für die beobachteten Potenzgesetze und die Gleichverteilung der Energie verantwortlich sind.

Abstract

Power laws are typical signatures of complex systems and examples in astrophysics are manifold. Understanding their origin is challenging and can be approached in very different ways. In this thesis, I first provide a mathematical treatment of power laws which starts from the defining property of scale-invariance. For physical systems this absence of scales holds only over a finite range. Power laws can be found as solutions to differential equations whereas their validity is usually constrained by initial and boundary conditions which I demonstrate with several examples. An almost physics-free interpretation for the origin of observed mass functions, $dN/dM \sim M^{-\alpha}$ with $\alpha \sim 2$, is given by a simple hierarchical fragmentation model which I discuss next to a more physical model of star formation.

Cosmic ray energy spectra are power laws over many orders of magnitude in contrast to exponentially decaying energy distribution functions which are typical for equilibrium statistical mechanics. Superstatistics is a particular generalization of statistical mechanics for nonequilibrium systems. It generates power law distribution functions from a superposition of equilibrium distributions with variable temperatures. I carefully assess the physical motivation for this model in order to apply it to the observed energy spectra of cosmic rays. This requires a relation between the superstatistical distribution function and the observed differential intensity which has been treated inaccurately by previous studies of superstatistics. Hence, the provided derivation clarifies and improves the theoretical basis of superstatistical models applied to particle physics. I apply this model to recent AMS data for primary (He, C, O) and secondary (Li, Be, B) cosmic rays in order to determine the best fit parameters. Smolla et al. (2020) interpret the two observed universality classes of cosmic ray spectra as resulting from the characteristic energy scale $\sim 200\,\mathrm{MeV}$ in QCD scattering processes and two distinct types of superpositions of temperature fluctuations. In addition to presenting these results, I also provide a critical discussion for this novel interpretation and the superstatistical model in general.

Interstellar turbulence, stellar initial mass function, star formation law, and far-infrared–radio correlation are examples for nearly universal power laws, in the sense that they are remarkably insensitive to variations in parameters of the respective physical system. For each case I review the available observational data and discuss models which account for their origin. Star formation turns out being an essential driver behind all these phenomena. I present a new schematic version of a galaxy model where thermal gas, turbulent gas, magnetic fields and cosmic rays all have comparable energy densities. The observed power laws characterize the interconnections between these four components and star formation. Due to the complexity and multi-scale nature of the galaxy, this model deliberately ignores many details. Its aim is to identify the self-regulating mechanisms which give rise to the observed power laws and the equipartition of energy.

Contents

List of Figures

Acronyms

BC boundary condition

CMF core mass function

CR cosmic ray

FRC far-infrared – radio correlation

IC initial condition

IMF (stellar) initial mass function

ISM interstellar medium

ODE ordinary differential equation

PDE partial differential equation

PDF probability density function

SF star formation

SFR star formation rate

SN supernova

SNR supernova remnant

Chapter 1

Introduction

Power laws are found in a broad variety of physical but also non-physical systems. If you count how often each word appears in this thesis and list all words according to their rank (most, second most, etc.) then you will discover a power law. And even if you translate this thesis and count the frequency of words in the foreign language you will again find a power law (e.g., Ferrer i Cancho, 2005). Further examples range from the number of animals in the ocean vs. their mass (e.g., Hatton et al., 2021), the frequency of earth quakes vs. their strength (e.g., Sornette et al., 1996) or the fractal coast line of Britain (e.g., Mandelbrot, 1967). Not only the examples are very diverse but also the proposed explanations for the origin of the observed power laws are manifold. Here, we focus on power laws in the realm of astrophysics and in particular on the following:

- Cosmic ray energy spectrum (chapter 3);
- Interstellar electron density power spectrum (chapter 4);
- Stellar initial mass function (section 5.1);
- Star formation law (section 5.2);
- Far-infrared–radio correlation (section 5.3).

All these phenomena are characterized by power laws which are remarkably insensitive to variations in the parameters of the respective systems. The cosmic ray energy spectrum is characterized by $\sim E^{-\gamma}$ where $\gamma = 2.7$ or $\gamma = 3.0$ hold for a large class of atomic nuclei with very different histories. The spectral slope of the electron density power spectrum appears to be identical when measured as a sort of galactic average via interstellar scintillation in radio waves or when measured in situ by the Voyager space probe in the local interstellar medium. Because stars form out of cool gas and the cooling rate of gas clouds increases with larger metallicity, it is reasonable to expect metallicity to be an important factor for star formation. However, both the stellar initial mass function and the star formation law appear to be largely unaffected by changes in metallicity. The far-infrared–radio correlation is connected to star formation and is observed in spiral galaxies like our own Milky Way but also in galaxies with very different masses, luminosities and star formation rates. Evidently, explaining the origin of the observed power laws requires mechanisms which are to some extent insensitive to the details of the system. It is in this sense that we use the term *universal* in the following.

Figure 1.1 shows a nearby spiral galaxy which is thought to be very similar to our own galaxy which we can only observe from the inside. Here, we focus on such type of regular disk galaxies and use characteristic properties and scales based on observations for the Milky Way. Our galaxy consists not only of stars and dark
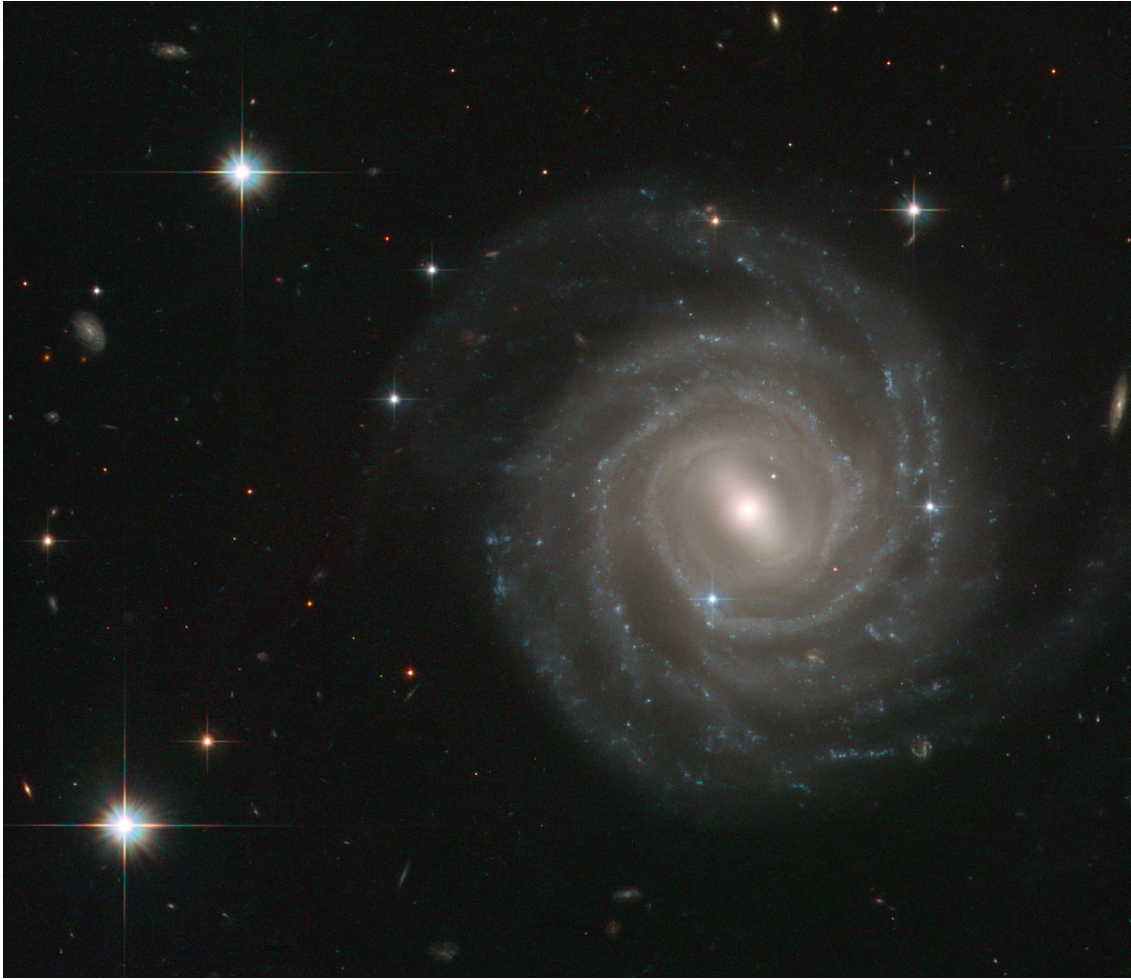
Figure 1.1: This barred spiral galaxy UGC 12158 is thought to have a lot in common with our own galaxy. Its diameter is $\sim 40\,\mathrm{kpc}$. Image credit: NASA/ESA Hubble Space Telescope, `https://esahubble.org/images/potw1035a/`

matter but also of interstellar gas, dust, radiation, and relativistic particles which can be summarized as interstellar medium (ISM). Most of the stellar and ISM mass are located in a thin disk which is approximately axisymmetric. In general and on large scales the density decreases with radius, however, for most of our considerations here we consider galactic averages. The interstellar gas can be found in multiple phases which are thought to coexist in an approximate pressure equilibrium (e.g., three phase model by McKee and Ostriker, 1977). The characteristic densities, temperatures and ionization degrees are presented in figure 1.2.

In order to calculate energy densities and energy dissipation rates for our galaxy we need to specify the total volume and an average density. Because we are mainly interested in processes that occur in the interstellar medium we consider a simple cylindrical disk model for the galaxy. We use $r = 15\,\mathrm{kpc}$ for the disk radius and $h = 300\,\mathrm{pc}$ for a constant disk height. We assume an average temperature of $T \sim 10^4\,\mathrm{K}$ (warm medium) and an average density of one proton per cm^3, which corresponds to a thermal pressure of

$$\frac{3}{2}nk_{\mathrm{B}}T \approx 2 \times 10^{-12}\,\mathrm{erg/cm^3} \tag{1.1}$$

and a total gas mass within the disk of $M_{\mathrm{gas}} \approx 5 \times 10^9\,\mathrm{M_\odot}$ which is of the order of fifty percent of the total gas mass and one percent of the total mass (baryons and

Component	Temperature (K)	Density (cm^{-3})	Fractional ionization
Molecular gas	10–20	$> 10^2$	$< 10^{-6}$
Cold neutral medium (CNM)	50–100	20–50	$\sim 10^{-4}$
Warm neutral medium (WNM)	6000–10000	0.2–0.5	~ 0.1
Warm ionized medium (WIM)	~ 8000	0.2–0.5	1.0
Hot ionized medium (HIM)	$\sim 10^6$	$\sim 10^{-2}$	1.0

Figure 1.2: A significant fraction of the total gas mass is bound in cold atomic and molecular hydrogen filling a rather small volume within the galactic disk. The warm medium occupies a larger volume inside and outside of the disk. The hot medium fills most of the volume outside of the disk. Table taken from Girichidis et al. (2020).

dark matter) of the galaxy. These values are in reasonable agreement with recent observations for the Milky Way (e.g. McMillan, 2017; Everall et al., 2022; Wang et al., 2022).

Considering the flow of energy within the galaxy the stars are a major driver which continuously convert gravitational and nuclear binding energy into other forms of energy (i.e., mostly radiation, but also kinetic energy in the form of relativistic particles and nonrelativistic gas motion). The luminosity of our galaxy today is of the order of a hundred billion solar luminosities or

$$\Gamma_{\mathrm{gal}} \sim 10^{45} \, \mathrm{erg/s}. \tag{1.2}$$

Most of this energy is carried by electromagnetic radiation emitted from stars and will ultimately leave the galaxy. The most extreme luminosities from individual stars are due to supernovae (SNe) with about $\sim 10^{53} \, \mathrm{erg/s}$ (Woosley and Janka, 2005). However, this power holds only for a very short time and most of the energy is carried by neutrinos which play an important role in the early evolution of SNe but hardly interact with the ISM. For large scale ($\gtrsim 100 \, \mathrm{pc}$) considerations of the galaxy and on long time scales ($\gtrsim \mathrm{Myr}$) we are interested in the average power from SNe which interacts with other components of the galaxy. Most importantly that is the kinetic energy carried by the expanding SNR. Woosley and Janka (2005) estimate the average release of kinetic energy per core collapse SN as $\sim 10^{51} \, \mathrm{erg}$. Given that in our galaxy about three SNe occur per century, the mean power contribution to kinetic energy is

$$\Gamma_{\mathrm{SN}} \sim 10^{42} \, \mathrm{erg/cm}^3. \tag{1.3}$$

This allows for an order of magnitude estimate about the power available to drive phenomena like interstellar turbulence or cosmic ray acceleration.

Figure 1.3 shows a schematic diagram for the basic architecture of our galaxy model together with the observed power laws which we investigate throughout this thesis. Evidently, this model ignores many of the details which are certainly relevant for accurately describing the small scale physical processes. The advantage of the model's simplicity is the possibility to consider the entire galaxy as a dynamical system in which energy flows between its components such that a stationary state of dynamical equilibrium can be achieved. Furthermore, it allows for a more visual and comprehensive investigation about the self-regulating mechanisms which are

responsible for the observed power laws and order of magnitude equipartition of energy densities in thermal gas, turbulent gas, magnetic fields, and cosmic rays (e.g., Draine, 2010; Seta and Beck, 2019; Sun et al., 2020; Ballesteros-Paredes et al., 2020). The model is not yet implemented numerically and for the given thesis it mainly serves as a guide for our intuition when discussing the origin of the respective power law. A more detailed version of the given diagram is presented in the concluding chapter 6.
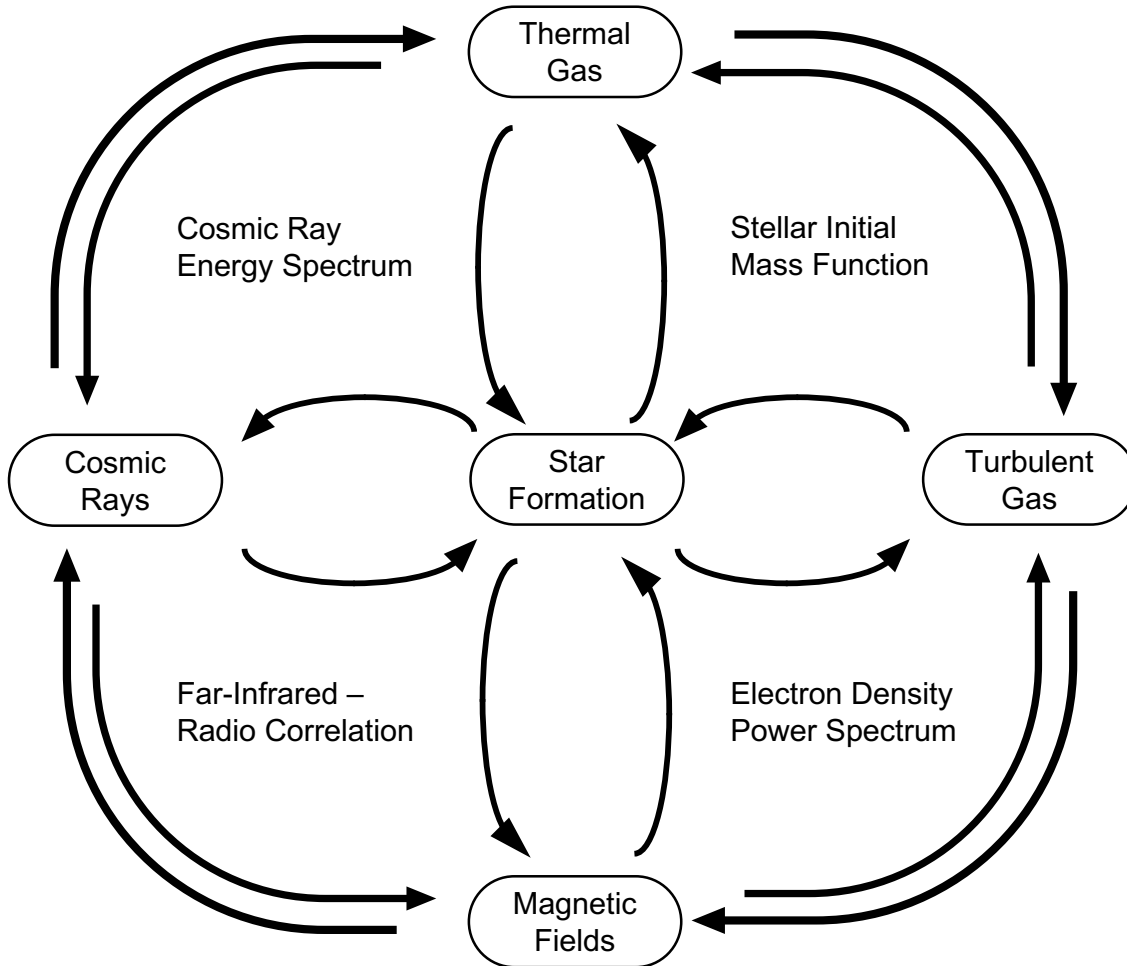
Figure 1.3: Schematic diagram of the main components in our galaxy model and the couplings (arrows) which are inspired by the observed power laws. The cosmic ray energy spectrum reveals a characteristic power law shape while covering more than ten orders of magnitude (see chapter 3). Stars appear to be formed according to a universal mass distribution, the stellar initial mass function, which includes a power law spanning two orders of magnitude in mass (see section 5.1). The fluctuations in the interstellar electron density reveal a power spectrum following a power law over eleven orders of magnitude in wave number with a spectral index close to a simple hydrodynamic turbulence model (see chapter 4). The far-infrared–radio correlation tightly connects two seemingly distinct parts of the electromagnetic spectrum (see section 5.3). Star formation is an essential driver which transfers nuclear binding energy to all the other galactic components which in turn also back-react on the star formation process.

Chapter 2

Mathematical Treatment of Power Laws

2.1 Characterizing power laws

2.1.1 Scale invariance

Scale invariance or *self-similarity* is a property tightly connected to power laws which can be illustrated quite simply. Sornette (2004) defines scale invariance in the following way. Consider an observable $\mathcal{O}$ which depends on some variable x. The observable is said to be scale-invariant if there is some number $\mu(\lambda)$ for all λ such that rescaling the variable, $x \rightarrow \lambda x$, yields to the following change of the observable

$$\mathcal{O}(\lambda x) = \mu \mathcal{O}(x). \tag{2.1}$$

This equation can be solved with the following Ansatz

$$\mathcal{O}(x) = C x^\alpha \tag{2.2}$$

which is the definition for a *power law*, with constant (independent of x) numbers C and α. Inserting equation (2.2) into equation (2.1) gives

$$\begin{aligned}
\mathcal{O}(\lambda x) &= C(\lambda x)^\alpha \\
&= \lambda^\alpha \mathcal{O}(x) \tag{2.3}
\end{aligned}$$

which allows us to express the power law exponent as $\alpha = \ln \mu / \ln \lambda$. *Self-similarity* or *scale invariance* is best illustrated by considering the ratio of rescaled-observable to original observable

$$\frac{\mathcal{O}(\lambda x)}{\mathcal{O}(x)} = \lambda^\alpha \tag{2.4}$$

which is independent of the variable x. The terminology *self-similarity* is mostly used when x is some length scale that is characteristic for the system such that $x \rightarrow \lambda x$ effectively produces a larger or smaller version of the system which is self-similar to the original one with respect to a given observable $\mathcal{O}(x)$. A simple geometrical example are two triangles with different size but identical measures in all three angles. Such triangles are self-similar and can be transformed into one another by an appropriate rescaling parameter λ. However, the concept of scale

invariance is quite general and the transformation $x \to \lambda x$ is not constrained to x being some length scale of the problem. For example it could also be a time- or velocity-scale upon which the observable depends.

  When we talk about *power laws* we are referring to functions defined by equation (2.2) which is actually a *monomial* because it consists of only one term with the given variable to some power. Physical observables which are of the form

$$\mathcal{O}'(x) = C_0 + C_1 x^\alpha, \tag{2.5}$$

with two constants C_0 and C_1, can simply be translated into a power law by introducing a new observable by subtracting the constant additive term, that is $\mathcal{O}(x) = \mathcal{O}'(x) - C_0$, such that $\mathcal{O}(x)$ is again a true power law. However, more general polynomials like $\mathcal{O}(x_1, x_2, x_3, ...) = \sum_i c_i x^{n_i}$ are in general not scale invariant or power laws. Of course, in reality most observables will not depend only on a single parameter x but on many different parameters like pressure, density, temperature, etc. In this case there is still hope that $\mathcal{O}(x)$ holds as an approximation at least for a certain range of values in the other parameters or at least when all other parameters are held constant. However, there are also many cases where the effect of the other parameters cannot be ignored and the scale invariance property becomes broken due to variation in the other parameters. Additionally, for any real physical system, scale invariance will only hold over a finite range in the parameter x. These boundaries (and/or initial conditions) effectively introduce characteristic scales into the problem which we discuss further in section 2.2.4.

2.1.2 Log-log plots

Double-logarithmic plots are frequently used in astrophysics and there are at least two reasons for this. First, it allows representing a large range of scales visually on a limited area for the given plot. Second, power laws turn into straight lines as is illustrated by figure 2.1. This is yet another visual demonstration of power laws being scale invariant.

  This property of power laws can also be demonstrated in mathematical terms. Consider for example the following kind of mass function (see chapter 5 on star formation) $N(M) = CM^{-\alpha}$ which can equivalently be written in logarithmic quantities $\tilde{M} = \log(M)$ (and therefore $M = 10^{\tilde{M}}$) as follows

$$\begin{aligned} \log N &= \log[CM^{-\alpha}] \\ &= \log[C(10^{\tilde{M}})^{-\alpha}] \\ &= \log C - \alpha \tilde{M} \log 10 \\ &= \log C - \alpha \log(M). \end{aligned} \tag{2.6}$$

This simple calculation shows why power laws turn into straight lines when both observable and variable are used in logarithmic scaling. The slope is given by the power law index, which for our example yields

$$\frac{\mathrm{d}(\log N)}{\mathrm{d}(\log M)} = -\alpha. \tag{2.7}$$
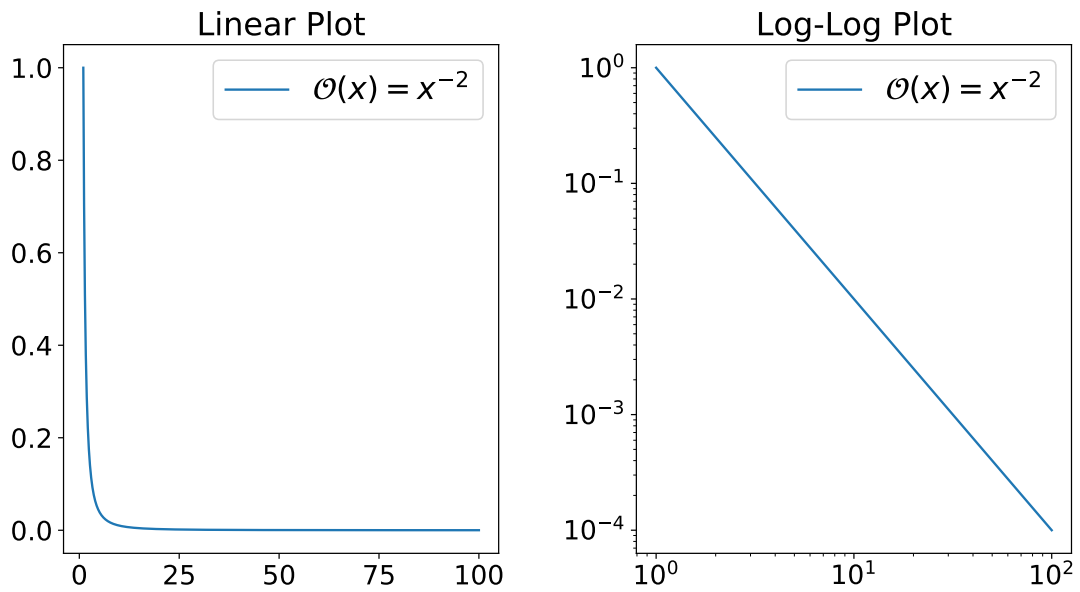
(a) Both axes in a linear scaling. (b) Both axes in a logarithmic scaling.

Figure 2.1: Whenever a power law observable, $\mathcal{O}$, or its variable, x, cover a larger range it is not very useful to use a linear scaling as illustrated by the left plot. Using a logarithmic scaling on both axes (right plot) allows to better visualize the entire range. Another benefit is that power laws reveal a characteristic property as they turn into straight lines where the slope is given by the power law index.

2.2 Differential equations

2.2.1 Some examples

In the following we present a few examples of ordinary differential equations (ODEs) in order to gain some intuition on how power laws can be generated as solutions to differential equations. It is a useful exercise because most physical laws are expressed by differential equations. For astrophysical applications fluid equations like Euler and Navier-Stokes are particularly relevant *partial* differential equations (PDEs) and will be addressed in the subsequent section.

Finding a solution to a *first* order ODEs leads to *one* constant of integration. This constant has to be specified via an extra condition, for example the initial condition. We denote the respective constant with C in the following and consider some ODEs for the observable $\mathcal{O}(x)$ depending on some variable x.

Consider the following kind of linear homogeneous ODE where the relative change of the observable is simply a function of the variable to some power, that is

$$\frac{\mathrm{d}\mathcal{O}(x)}{\mathrm{d}x} = \alpha \frac{1}{x^{\gamma}} \tag{2.8}$$

with constant factor α. Solutions to this ODE are obtained simply by integration as follows

$$\mathcal{O}(x) = \mathcal{O}(x_0) + \alpha \int_{x_0}^{x} \tilde{x}^{-\gamma} \mathrm{d}\tilde{x}. \tag{2.9}$$

The solutions to this ODE can be separated into two classes for $\gamma = 1$ and $\gamma \neq 1$. The former condition yields logarithmic solutions[1] whereas the latter requirement yields the following power law[2]

$$\mathcal{O}(x) = C + \frac{\alpha}{1-\gamma}x^{1-\gamma} \qquad (\gamma \neq 1) \tag{2.11}$$

where $C = \mathcal{O}(x_0) - \alpha/(1-\gamma)x_0^{1-\gamma}$. Equation (2.8) describes the relative change of the observable with respect to the variable as proportional to some power of the variable itself and *independent* of the value for the observable itself. Its form is therefore quite general and it generates power law solutions where the power law index $(1-\gamma)$ can take any value for $\gamma \neq 1$.

Another relevant example for a linear homogeneous ODE is obtained by multiplying the r.h.s. of equation (2.8) with the observable $\mathcal{O}(x)$ which yields

$$\frac{\mathrm{d}\mathcal{O}(x)}{\mathrm{d}x} = \alpha\frac{\mathcal{O}(x)}{x^\gamma}. \tag{2.12}$$

For $\gamma \neq 1$ the solutions are exponential functions.[3] For $\gamma = 1$ this ODE directly reflects the scale invariance of the solutions because the infinitesimal change of observable $\mathcal{O}$ with respect to the variable x is simply proportional to the ratio of the respective absolute quantities, that is

$$\frac{\mathrm{d}\mathcal{O}(x)}{\mathrm{d}x} = \alpha\frac{\mathcal{O}(x)}{x}. \tag{2.14}$$

Hence, it comes as no surprise to recover a power law solution, that is

$$\mathcal{O}(x) = Cx^\alpha \tag{2.15}$$

with constant $C = \mathcal{O}(x_0)/x_0^\alpha$.

A physical example for this ODE stems from the field of cosmic ray (CR) research. The energy spectra of these electrically charged particles reaching Earth from space turn out to be close to a single power law index over many orders of magnitude. We discuss this topic in greater depth in chapter 3 but for now we only want to present a very simple argument presented by Syrovat-Skii (1961) which connects the observed spectrum with our given ODE (2.14) and on the equipartition of energy.

---

[1]For $\gamma = 1$ the solutions to equation (2.8) are

$$\mathcal{O}(x) = C + \alpha\ln x \tag{2.10}$$

with constant $C = \mathcal{O}(x_0) - \alpha\ln x_0$.

[2]This equation is strictly speaking not a power law because of the additive constant C. However, this term can simply be removed by subtracting the constant and considering this new observable which is a true power law as defined in section 2.1.

[3]For completeness we provide the solution to the ODE (2.12) for $\gamma \neq 1$ which is

$$\mathcal{O}(x) = C\exp\left(\frac{\alpha}{1-\gamma}x^{1-\gamma}\right) \tag{2.13}$$

with constant $C = \exp\left(-\alpha x_0^{1-\gamma}/(1-\gamma)\right)\mathcal{O}(x_0)$. For $\gamma = 0$ the solution describes simply an exponential increase or decay (depending on the signature of α) and for $\gamma = -1$ and $\alpha = -\sigma^2$ the solution turns into the normal distribution $\sim \exp(-x^2/(2\sigma^2))$ provided the appropriate choice of normalization constant C.

The argument aims to explain the power law index of the number of cosmic ray particles N scaling with energy E as follows

$$N(E) \sim E^{-3/2} \tag{2.16}$$

or equivalently

$$\frac{\mathrm{d}N(E)}{\mathrm{d}E} \sim E^{-5/2}. \tag{2.17}$$

Syrovat-Skii (1961) makes the following assumptions in order to explain this scaling.

1. The total internal energy, U, of the CR accelerator is distributed equally among the following three components: cosmic ray energy, U_{CR}, turbulent energy, U_{turb}, magnetic energy, U_{mag}, such that $U = 3U_{\mathrm{CR}}$.

2. The CRs are ultra-relativistic such that the kinetic energy is approximately equal to the total energy of the CR particle, E, and we have $U_{\mathrm{CR}} = NE$ and $U = 3NE$. Hence $\mathrm{d}U = \mathrm{d}(3NE) = 3E\mathrm{d}N + 3N\mathrm{d}E$.

3. Energy losses occur only due to diffusion of CR particles (i.e. neglecting radiative losses) and therefore $\mathrm{d}U = E\mathrm{d}N$.

The last two equations for $\mathrm{d}U$ can be combined and arranged to

$$\frac{\mathrm{d}N(E)}{\mathrm{d}E} = -\frac{3}{2}\frac{N(E)}{E} \tag{2.18}$$

which is the ODE presented in equation (2.14) upon identifying $\mathcal{O}(x) \to N(E)$ and $\alpha = -3/2$ and consequently yields the solution $N(E) = CE^{-3/2}$ in agreement with equation (2.16) for the observations which we aimed to explain.[4]

From these simple examples we would like to emphasize the following learnings:

1. Both ODEs, that is equations (2.8) and (2.12), are *linear* and hence the sum of particular solutions is also a solution to the respective ODE. This *superposition principle* holds irrespective of the given value of γ and hence for both power law and exponential or logarithmic solutions presented here.

2. One initial condition is required to specify a particular solution to first order ODEs. However, the initial condition is represented in the particular solution merely as an additive constant or constant factor. The functional form (e.g., power law or exponential) is not affected by the initial condition.

These properties are in general not fulfilled when we consider *nonlinear* ODEs. To demonstrate this we consider the following example

$$\frac{\mathrm{d}\mathcal{O}}{\mathrm{d}x} = -\alpha\mathcal{O}^3(x) \tag{2.19}$$

---

[4]Evidently the desired power law index $-3/2$ is connected to the internal energy of the CR accelerator being distributed among *three* components. If the internal energy was distributed among four components, $\mathrm{d}U = \mathrm{d}(4NE)$, the analogous derivation would result in $N(E) = CE^{-3/4}$ which is a spectrum significantly shallower than observed. Radiation or thermal pressure would be two potential candidates for a fourth component. Their relative significance depends on the environment under consideration.

with constant $\alpha > 0$. A solution to this nonlinear ODE is

$$\mathcal{O}(x) = \sqrt{\frac{1}{2\alpha}} \left(\tilde{C} + x \right)^{-1/2} \tag{2.20}$$

with constant $\tilde{C} = \mathcal{O}(x_0)/(2\alpha) - x_0$. It is straight forward to verify that the sum of two solutions with different values of $\tilde{C}$ does not yield another solution to the ODE (2.19). The superposition principle is not valid because of the nonlinear term $\mathcal{O}^3(x)$. Another point to outline here is that the solution is *not a power law* in general but it converges to a power law only asymptotically as

$$\mathcal{O}(x) \xrightarrow{x \gg \tilde{C}} \sim x^{-1/2}. \tag{2.21}$$

Evidently, for a given value of α it is the initial condition $\mathcal{O}(x_0)$ which determines the scale (via the requirement $x \gg \tilde{C} = \mathcal{O}(x_0)/(2\alpha) - x_0$) above which the solution converges to a power law. The relevance of initial conditions in nonlinear ODEs therefore goes beyond some simple multiplication or addition of a constant as we demonstrated before with the examples for linear ODEs. For nonlinear ODEs the initial conditions can actually alter the shape of the solutions.

In fluid mechanics one usually deals with *partial* differential equations (PDEs) that is equations with derivatives of more than one variable in general, for example one time and three spatial derivatives. Depending on the complexity of the flow these equations are linear or nonlinear. In the following we introduce the (in general nonlinear) Euler and Navier-Stokes equations and investigate their connection to scale invariance and power law solutions.

2.2.2 Euler equations

For a non-viscous fluid with density $\rho = \rho(\boldsymbol{r}, t)$, pressure p, and velocity $\boldsymbol{v} = \boldsymbol{v}(\boldsymbol{r}, t)$, the continuity equation is

$$\frac{\partial \rho}{\partial t} = -\nabla \cdot (\rho \boldsymbol{v}), \tag{2.22}$$

and in the presence of an external field, with force density $\boldsymbol{f}$ (note $[\boldsymbol{f}] = \text{Force/Volume} = ML^{-2}t^{-2}$), the Euler equations (in plural because one equation for each vector component) are given as the following set of *nonlinear* PDEs

$$\rho \left(\frac{\partial \boldsymbol{v}}{\partial t} + (\boldsymbol{v} \cdot \nabla)\boldsymbol{v} \right) = \boldsymbol{f} - \nabla p. \tag{2.23}$$

Together these equations describe the kinematics and dynamics of an incompressible fluid with zero viscosity under the influence of pressure and gravity. In the context of star formation these equations are frequently used to model the gravitational collapse of a gas cloud. For fluids with non-zero viscosity the Navier-Stokes equations need to be considered.

2.2.3 Navier-Stokes equations

For a compressible viscous fluid with density ρ, pressure p, viscosities η and ξ (with $[\eta] = [\xi] = ML^{-1}t^{-1}$)[5] and in the presence of some force field density $\boldsymbol{f}$ (with $[\boldsymbol{f}] =$

---

[5]For compressible fluids there are two kinds of viscosity. The first, η, is also known as dynamic viscosity and corresponds to the shear stress of the fluid. The second viscosity, ξ, arises from the

Force/Volume $= ML^{-2}t^{-2}$) the Navier Stokes equations are given (e.g., Bestehorn, 2006) by

$$\rho\left(\frac{\partial \boldsymbol{v}}{\partial t} + (\boldsymbol{v}\cdot\nabla)\boldsymbol{v}\right) = -\nabla p + \boldsymbol{f} + \eta\nabla^2\boldsymbol{v} + \left(\xi + \frac{\eta}{3}\right)\nabla(\nabla\cdot\boldsymbol{v}) \qquad (2.24)$$

together with the continuity equation (2.22).

These equations are quite general but also contain some restrictive assumptions. For example both viscosities are assumed to be constant for all locations in the fluid. In general a fluid's viscosity depends on its temperature and consequently equation (2.24) is, at least strictly speaking, constrained to *isothermal* compressible and viscous fluids.

For an incompressible fluid $\partial\rho/\partial t = 0$ reduces the continuity equation (2.22) to $\nabla\cdot\boldsymbol{v} = 0$ and the Navier Stokes equations (2.24) simplify (e.g., Bestehorn, 2006) to

$$\rho\left(\frac{\partial \boldsymbol{v}}{\partial t} + (\boldsymbol{v}\cdot\nabla)\boldsymbol{v}\right) = -\nabla p + \boldsymbol{f} + \eta\nabla^2\boldsymbol{v}. \qquad (2.25)$$

Just like any other set of dynamical equations the Navier-Stokes equations can be brought into a dimensionless form by a change of variables. Therefore we apply the following transformations

$$t' = \frac{t}{t_c} \text{ and therefore } \frac{\partial}{\partial t} = \frac{1}{t_c}\frac{\partial}{\partial t'}, \qquad (2.26)$$

$$\boldsymbol{x}' = \frac{\boldsymbol{x}}{l_c} \text{ and therefore } \nabla = \frac{1}{l_c}\nabla', \qquad (2.27)$$

$$\rho' = \frac{\rho}{\rho_c}, \qquad (2.28)$$

$$\boldsymbol{v}' = \frac{\boldsymbol{v}}{v_c}, \qquad (2.29)$$

$$p' = \frac{p}{p_c}, \qquad (2.30)$$

$$\boldsymbol{f}' = \frac{\boldsymbol{f}}{f_c}, \qquad (2.31)$$

where we have introduced the following characteristic and constant scales: a length scale l_c, a velocity scale v_c, a density ρ_c, a pressure[6] p_c, and a force density scale f_c. The new primed variables, t' for time, $\boldsymbol{x}'$ for position, ρ' for density, $\boldsymbol{v}'$ for velocity, p' for pressure, and $\boldsymbol{f}'$ for the force field density, are all dimensionless by construction. Applying this change of variables to equation (2.24) and multiplying both sides of the equation with $l_c/(v_c^2\rho_c)$ yields the compressible Navier-Stokes equations in the following dimensionless form

$$\rho'\left(\text{St}\frac{\partial \boldsymbol{v}'}{\partial t'} + (\boldsymbol{v}'\cdot\nabla')\boldsymbol{v}'\right) = -\text{Eu }\nabla'p' + \text{Fr}^{-2}\boldsymbol{f}' + \text{Re}^{-1}\nabla'^2\boldsymbol{v}' + \text{Re}_2^{-1}\nabla'(\nabla'\cdot\boldsymbol{v}').$$

$$(2.32)$$

---

tension due to compression of the fluid. The numerical factors in front of the second viscosity in the Navier-Stokes equations vary depending on the given definition of the shear stress tensor, commonly labeled as τ_{ij}, from which the two viscosities are derived ultimately.

[6]The pressure scale is also frequently denoted as Δp because it refers to a pressure difference. Here we simply write p_c to follow a coherent and simple notation.

Here we have introduced the following four dimensionless numbers[7]

$$\text{St} = \frac{l_{\text{c}}}{t_{\text{c}} v_{\text{c}}} \quad \text{(Strouhal number)}, \tag{2.33}$$

$$\text{Eu} = \frac{p_{\text{c}}}{\rho_{\text{c}} v_{\text{c}}^2} \quad \text{(Euler number)}, \tag{2.34}$$

$$\text{Fr} = \frac{v_{\text{c}}}{\sqrt{l_{\text{c}} f_{\text{c}}/\rho_{\text{c}}}} \quad \text{(Froude number)}, \tag{2.35}$$

$$\text{Re} = \frac{l_{\text{c}} v_{\text{c}} \rho_{\text{c}}}{\eta} \quad \text{(Reynolds number)}. \tag{2.36}$$

The last term on the right hand side of equation (2.32) also carries a dimensionless factor, $\text{Re}_2^{-1} = \frac{\xi + \eta/3}{l_{\text{c}} v_{\text{c}} \rho_{\text{c}}}$, which is similar to the Reynolds number but to our best knowledge does not have a commonly accepted name. The continuity equation (2.22) in these dimensionless variables is

$$\text{St} \frac{\partial \rho'}{\partial t'} = -\nabla \left(\rho' \boldsymbol{v}' \right). \tag{2.37}$$

For astrophysical applications it is common practice to use a different set of dimensional parameters which we obtain by making the following identifications

$$\text{St} = \frac{l_{\text{c}}}{t_{\text{c}} v_{\text{c}}} \xrightarrow{t_{\text{c}} = l_{\text{c}}/v_{\text{c}}} \text{St} = 1, \tag{2.38}$$

$$\text{Eu} = \frac{p_{\text{c}}}{\rho_{\text{c}} v_{\text{c}}^2} \xrightarrow{p_{\text{c}} = c_s^2 \rho_{\text{c}}} \mathcal{M}^{-2} = \left(\frac{c_s}{v_{\text{c}}} \right)^2, \tag{2.39}$$

$$\text{Fr}^2 = \frac{v_{\text{c}}^2}{l_{\text{c}} f_{\text{c}}/\rho_{\text{c}}} \xrightarrow{f_{\text{c}} = \rho_{\text{c}} GM/l_{\text{c}} \sim G\rho_{\text{c}}^2 l_{\text{c}}^2} \alpha_{vir} = 2E_{kin}/|E_{grav}| \sim \frac{v_{\text{c}}^2}{G\rho_{\text{c}} l_{\text{c}}^3}. \tag{2.40}$$

With these new dimensionless numbers, namely the Mach number, $\mathcal{M} = v_{\text{c}}/c_s$, and the virial parameter, $\alpha_{vir} \sim v_{\text{c}}^2/(G\rho_{\text{c}} l_{\text{c}}^3)$, the Navier-Stokes equations can be written as

$$\rho' \left(\frac{\partial \boldsymbol{v}'}{\partial t'} + (\boldsymbol{v}' \cdot \nabla') \boldsymbol{v}' \right) = -\mathcal{M}^{-2} \nabla' p' + \alpha_{vir}^{-1} \boldsymbol{f}' + \text{Re}^{-1} \nabla'^2 \boldsymbol{v}' + \text{Re}_2^{-1} \nabla'(\nabla' \cdot \boldsymbol{v}'). \tag{2.41}$$

A clear benefit from introducing dimensionless numbers into the Navier-Stokes equations is demonstrated by the *similarity principle*. It allows for a connection between the dynamical and kinematical properties of a fluid. The dynamical properties of the fluid are characterized by the dimensionless numbers which determine the kinematical behavior of the fluid. This implies that two fluid streams can be *similar* although their absolute size or velocity are very different - provided that their dimensionless numbers are equal and they are characterized by similar initial

---

[7]Of course these dimensionless numbers can also be expressed in terms of other related quantities. The Reynolds number is also frequently expressed with respect to the dynamic viscosity $\nu = \eta/\rho_{\text{c}}$ as $\text{Re} = l_{\text{c}} v_{\text{c}}/\nu$. The Froude number with respect to the gravitational attraction $g_{\text{c}} = f_{\text{c}}/\rho_{\text{c}}$ is written as $\text{Fr} = v_{\text{c}}/\sqrt{g_{\text{c}} l_{\text{c}}}$. Alternatively the Froude number is also sometimes defined as $\text{Fr} = v_{\text{c}}^2/(g_{\text{c}} l_{\text{c}})$. In astrophysical applications the Froude number is less common and it is replaced by the virial paramter $\alpha_{vir} = 2E_{kin}/|E_{grav}| \sim v_{\text{c}}^2/(G\rho_{\text{c}} l_{\text{c}}^3)$ which can be obtained from the Froude number when identifying $f_{\text{c}} = \rho_{\text{c}} GM/l_{\text{c}}$ and $M = \rho_{\text{c}} l_{\text{c}}^3$.

and boundary conditions. We emphasize the importance of the latter requirement because it appears to be overlooked sometimes.

All quantities in equation (2.41) are dimensionless which has inspired some authors to refer to them as "scale-free equations" (e.g., Krumholz, 2014; Guszejnov et al., 2018). These equations are scale-free in the sense that physical scales like the size of the system or the velocity dispersion only enter into the equations in certain combinations via the dimensionless parameters. For example Krumholz (2014) points out that rescaling the density and length scales as

$$\rho \rightarrow \lambda\rho, \tag{2.42}$$

$$l \rightarrow \lambda^{-1/2}l \tag{2.43}$$

leaves Mach number, $\mathcal{M}$, and the virial parameter, α_{vir}, and the Reynolds number, Re, unchanged.[8] This property is what is commonly meant by "scale-free" dynamical equations: it is the possibility to rescale the system in a certain way such that the relevant dimensionless parameters are unchanged. However, there may very well be other physical quantities which are not invariant under these transformations like for example the mass of some sphere in the fluid changes as

$$M \sim \rho l^3 \rightarrow \tilde{M} \sim \lambda^{-1/2}M \tag{2.44}$$

Krumholz (2014) uses this example to point out that numerical simulations for star formation, which are based on equations like the Navier-Stokes equations (2.41), cannot be used to derive some characteristic mass scale - unless there are physical reasons which constrain the possibility to rescale the system. And that is precisely the point to emphasize here. The physical reality, in contrast to idealized models, introduces scales into these scale-free equations. This is unavoidable because there are physical processes which are more or less important on particular scales only, like for example heat and radiation transfer processes which are negligible for diffuse gas but dominate the thermal energy balance of a contracting gas cloud for larger densities. Other examples are dissipative processes due to the viscosity of a fluid which are dominant only on small scales (meaning "small" compared to some characteristic length scale of the system like its diameter).

Another subtlety we would like to comment here concerns the connection of *nonlinear* differential equations and *self-similar* solutions, that is power law solutions. The importance of initial and boundary conditions for finding particular solutions to differential equations appears to be sometimes not emphasized sufficiently. Großmann (2011) for example claims that nonlinear equations produce self-similar solutions[9] and concludes from it that one should expect self-similar flows[10] whenever the nonlinear term, $(\boldsymbol{v} \cdot \nabla)\boldsymbol{v}$, in the Navier-Stokes equations (2.25) dominates over the viscous term $\eta\nabla^2\boldsymbol{v}$. This argument suggests that the Euler equations (2.23) should produce self-similar solutions for $\boldsymbol{v}(\boldsymbol{r}, t)$. However, the analytic form of the solutions depends on the initial and boundary conditions. For example the so-called

---

[8] More generally the transformation $(t, \boldsymbol{x}, \boldsymbol{v}) \mapsto (\lambda^{2n}t, \lambda^n\boldsymbol{x}, \lambda^{-n}\boldsymbol{v})$ leaves the Euler equations (2.23) invariant for $n \in \mathbb{R}$ and for the Navier-Stokes equations (2.32) this holds true only for the single case where $n = 1$.

[9] "Nichtlineare Differentialgleichungen erzeugen selbstähnliche Lösungen!" on p. 92 in Großmann (2011)

[10] "Beispielsweise haben wir zu erwarten, dass die der Navier-Stokes-Gleichung genügenden Strömungen $u(x, t)$ von Flüssigkeiten selbstähnlich sind, solange der Term $\propto u^2$ das Dämpfungsglied $\propto \nu$ überwiegt" on p. 93 in Großmann (2011)

ABC flows (Arnold-Beltrami-Childress flows) are a simple steady-state solution to the Euler equations which is not self-similar (power laws) but spatially periodic (trigonometric functions) according to Dombre et al. (1986). Together with the above example for a nonlinear ODE (equation (2.19)) we have presented two counter examples to demonstrate that nonlinear ODEs do not necessarily produce power law solutions. It is equally true that power laws are not only generated by *nonlinear* ODEs but also by *linear* ODEs as demonstrated above with equation (2.14).

In the following we discuss the connection of dimensionless dynamical equations and power laws and the importance of initial and boundary conditions for finding solutions. Because the Navier-Stokes equations are very hard to solve in general we take some simpler partial differential equations in order to demonstrate that dimensionless equations do not necessarily lead to scale-free solutions and scaling relations. The reason for this is simply the necessity to include initial and boundary conditions in order to solve the equations. And that is how characteristic scales enter into these otherwise scale-free dynamical equations.

2.2.4   Initial and boundary conditions

In order to determine the evolution of some physical observable (e.g., density or velocity) with respect to some parameter (e.g., time) from the underlying dynamical equations it is necessary to specify the initial conditions (ICs) and boundary conditions (BCs). In general, these conditions affect whether or not a solution is self-similar or not. Here we consider two examples. First, a solution to the diffusion equation which is not self-similar and later a self-similar solution for the density profile of an isothermal gas cloud which is collapsing under its own gravity and described by Euler equations as inviscid flow.

The diffusion equation can be written as

$$\frac{\partial \boldsymbol{v}}{\partial t} = D\nabla^2 \boldsymbol{v} \tag{2.45}$$

with Diffusion coefficient $[D] = L^2 t^{-1}$ assumed to be constant. Using the same notation as in the previous section we can convert this equation the following dimensionless form

$$\frac{\partial \boldsymbol{v'}}{\partial t'} = D'\nabla'^2 \boldsymbol{v'} \tag{2.46}$$

where we have defined a dimensionless diffusion constant $D' = Dt_{\mathrm{c}}/l_{\mathrm{c}}^2$ with $D' > 0$. Considering only the dimensionless diffusion equation (2.46) it appears that any diffusive system could be characterized simply by its diffusion coefficient D'. And since the diffusion equation and D' are both invariant under the following set of transformations

$$x \to \lambda x \tag{2.47}$$
$$t \to \lambda^2 t \tag{2.48}$$

the characteristic length scales (e.g., the size of the system) are irrelevant and it is only the diffusion coefficient that determines the system's evolution. However, this statement was only true if the initial and boundary conditions would be invariant

under the same transformations. This is in general not the case. Consider for example the following initial condition

$$v(x', 0) = \sin\left(\frac{\pi}{L'}x\right), \qquad x' \in (0, L') \tag{2.49}$$

and boundary condition

$$v(0, t) = v(L', t') = 0, \qquad t' \in (0, \infty), \tag{2.50}$$

where the lengh scale L is dimensionless, i.e., expressed in units of l'. Together with these two conditions the diffusion equation (2.46) can be solved via separation of variables (p.991, Arens et al., 2010) which yields

$$v(x, t) = e^{-(\pi D'/L')^2 t'} \sin\left(\frac{\pi}{L'}x'\right). \tag{2.51}$$

Notably this solution is not scale-free but it contains a characteristic length scale, L', which has entered via the initial and boundary conditions.

A well known example for a self-similar solution can be found in the context of star formation. Consider an initially isotropic cloud of gas which collapses isothermally under its own gravity and we would like to determine the evolution of the density, $\rho(r)$, with respect to the radius from the center of the cloud, r. Shu (1977) investigated this problem by solving the Euler equations brought to the following one-dimensional form

$$\frac{\partial v}{\partial t} + v\frac{\partial v}{\partial r} = \frac{c_s^2}{\rho}\frac{\partial \rho}{\partial r} - \frac{GM}{r^2} \tag{2.52}$$

together with the continuity equation

$$\frac{\partial \rho}{\partial t} + \frac{1}{r^2}\frac{\partial}{\partial r}\left(r^2 \rho v\right) = 0 \tag{2.53}$$

where M is the total mass of the cloud and c_s is the speed of sound. There are different kinds of solutions (Shu (1977) present singular solutions, collapse solutions, expansion wave-collapse solutions) and one of them is the self-similar density profile

$$\rho(r) \sim r^{-2}. \tag{2.54}$$

Shu (1977) show that this scaling holds for the nearly static outer envelope of the collapsing cloud and that it results from requiring $v \to 0$ for $t \to 0$ which is a particular choice for the ICs.

These two examples, diffusion and isothermal collapse, are meant to illustrate that in general it is necessary to take into account the initial and boundary conditions in order to potentially infer scaling-laws from dynamical equations like Euler or Navier-Stokes equations. In chapter 4 we present Kolmogorov's 1941 turbulence model which is characterized by the velocity scaling $v \sim l^{1/3}$. This particular self-similar velocity scaling results from demanding a constant energy transfer rate in the velocity field of the flow provided that the fluid is incompressible, homogeneous and isotropic. Similar to the previous examples, homogeneity and isotropy of the flow requires appropriate initial and boundary conditions.
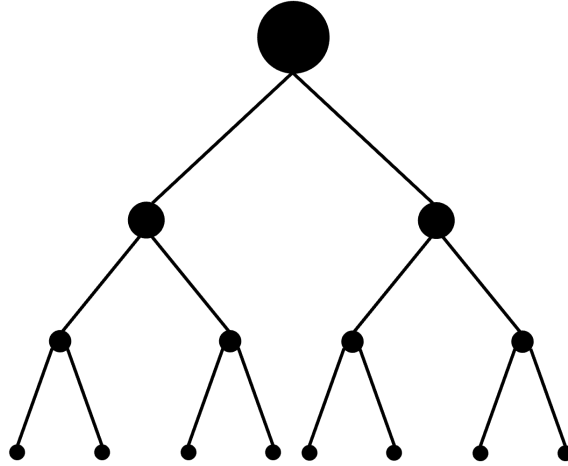
Figure 2.2: This hierarchical tree diagram illustrates the first three steps of a continuous fragmentation process of some large object into smaller pieces. For a perfectly self-similar process the number of branches is constant over all levels and the total mass of the initial object will be divided into equal parts among the fragments at each level.

2.3   Hierarchical fragmentation

A very simple and general way to obtain a power law is through a branching process where some object continuously fragments into pieces level by level as illustrated by figure 2.2.

   If the initial object has a mass M_0 and we assume it to continuously fragment into equally massive pieces at each level, n, then the number of pieces, N, with a certain mass, M_n, is given by

$$N(M_n) = \frac{M_0}{M_n} \tag{2.55}$$

provided that no mass is lost or left behind, meaning the total mass of all fragments at every level of the hierarchical tree is constant. Assume that the branching process occurs on a very short time scale compared to the life time of pieces, τ, before they fragment again into smaller pieces and assume that $\tau \approx$ const for all levels. Imagine a random sampling process of pieces from an ensemble of many ($\rightarrow \infty$) hierarchical trees then the number of pieces within a given mass interval is determined by equation (2.55) and therefore

$$\frac{\mathrm{d}N(M)}{\mathrm{d}M} \propto M^{-2}. \tag{2.56}$$

This particular scaling with the inverse square of the mass is close to the observed value for the high mass range of the stellar initial mass function (see chapter 5) and many other astrophysical objects (see section 5.1.2).

   In order to come a bit closer to the reality of star formation the fragmentation model can also be formulated with some additional features as presented by Guszejnov et al. (2018). Assume that at each step there is a probability ϵ with $0 < \epsilon < 1$ for the fragmentation cascade to terminate and the respective piece to turn its entire mass into a star. The total mass of stars $M_\star$ with mass M_n which formed at level n is then given by

$$\frac{M_\star(M_n)}{M_0} = \epsilon(1 - \epsilon)^n. \tag{2.57}$$

For a scale-free fragmentation cascade over a larger range we require $\epsilon \ll 1$. The number of fragments N produced per level is constant and we want it to be some small natural number. Then the mass of a fragment relative to its parent is $\kappa = M_n/M_{n-1} = N^{-1}$ with $0 < \kappa < 1$. With respect to the initial mass, M_0, we find

$$\frac{M_n}{M_0} = (1-\epsilon)^n \kappa^n. \tag{2.58}$$

In order to determine the scaling of the mass function

$$N(M_n) = \frac{M_\star(M_n)}{M_n} \tag{2.59}$$

we have to calculate $M_\star(M_n)$ for arbitrary level n. This requires a fair bit of algebra and some approximations in order to determine a solution without specifying the parameters κ and ϵ. Plugging equation (2.58) into equation (2.57) gives

$$\frac{M_\star(M_n)}{M_0} = \epsilon \kappa^{-n} \frac{M_n}{M_0}. \tag{2.60}$$

The level n can be expressed as

$$n = \frac{\ln(\frac{M_n}{M_0})}{\ln(1-\epsilon) + \ln(\kappa)} \tag{2.61}$$

and allows us to rewrite the κ-term as follows

$$\begin{aligned}
\kappa^{-n} &= \left(\kappa^{\frac{-1}{\ln(1-\epsilon)+\ln(\kappa)}} \right)^{\ln\left(\frac{M_n}{M_0}\right)} \\
&= \left(\frac{M_n}{M_0} \right)^{\ln\left(\kappa^{\frac{-1}{\ln(1-\epsilon)+\ln(\kappa)}} \right)} \\
&= \left(\frac{M_n}{M_0} \right)^{\frac{-\ln(\kappa)}{\ln(1-\epsilon)+\ln\kappa}}.
\end{aligned} \tag{2.62}$$

Plugging this into equation (2.60) gives

$$\begin{aligned}
\frac{M_\star(M_n)}{M_0} &= \epsilon \left(\frac{M_n}{M_0} \right)^{\frac{-\ln(\kappa)}{\ln(1-\epsilon)+\ln\kappa}} \frac{M_n}{M_0} \\
&= \epsilon \left(\frac{M_n}{M_0} \right)^{\frac{\ln(1-\epsilon)}{\ln(1-\epsilon)+\ln\kappa}} \\
&= \epsilon \left(\frac{M_n}{M_0} \right)^{\frac{1}{1+\ln\kappa/\ln(1-\epsilon)}}.
\end{aligned} \tag{2.63}$$

The latter exponent can be approximated for a reasonable range of values for the parameters ϵ and κ. For $0 < \epsilon \ll 1$, which we required in the first place in order to obtain a large range for the cascade, we have

$$\begin{aligned}
\ln(1-\epsilon) &= -\epsilon + \mathcal{O}(\epsilon^2) \\
&\approx -\epsilon.
\end{aligned} \tag{2.64}$$

The parameter $\kappa = N^{-1}$ represents the inverse of the number of fragments per fragmentation event. Here we do not bother to define a rigorous limit but simply argue that the minimum requirement $N \geq 2$ (otherwise there is no fragmentation at all) is sufficient to guarantee that $\ln(\kappa) \ll 0$ (because $\ln(1/2) \approx -0.7$ and the logarithm is monotonically decreasing for larger N) and therefore the fraction $\ln(\kappa)/(\ln(1 - \epsilon))$ will be some large number such that we can approximate the entire exponent as

$$
\begin{aligned}
\frac{1}{1 + \ln\kappa/\ln(1 - \epsilon)} &= \frac{1}{\ln\kappa/\ln(1 - \epsilon)} + \mathcal{O}\left(\left(\frac{1}{\ln\kappa/\ln(1 - \epsilon)}\right)^2\right) \\
&\approx \frac{\ln(1 - \epsilon)}{\ln\kappa} \\
&\approx \frac{-\epsilon}{\ln\kappa} \\
&\approx 0.
\end{aligned}
\tag{2.65}
$$

Applying this approximation to equation (2.63) we ultimately find

$$
\frac{M_\star(M_n)}{M_0} \approx \epsilon = \text{const.}
\tag{2.66}
$$

Plugging this result into (2.59) yields

$$
N(M_n) \propto M_n^{-1}
\tag{2.67}
$$

which holds for all levels $n \ll \epsilon^{-1}$ and therefore we recover the identical scaling as in equation (2.56) found for the less elaborate model.

This particular scaling, $N(M) = \alpha M^{-1}$, with constant α, guarantees an equal amount of mass contained in any logarithmic interval of mass which can be simply verified as follows

$$
\begin{aligned}
\int_{M_1}^{M_2} N(M)\mathrm{d}M &= \alpha \int_{M_1}^{M_2} M^{-1}\mathrm{d}M \\
&= \alpha \ln\left(\frac{M_2}{M_1}\right)
\end{aligned}
\tag{2.68}
$$

which is constant for $M_2/M_1 = \text{const.}$ A particular case is the frequently seen choice of a logarithmic mass bin which sets $M_2/M_1 = 10$. This scale invariant mass function is observed for a broad variety of astronomical objects as we discuss in section 5.1.2.

2.4   Statistical physics

### 2.4.1   Heavy tails in probability density functions

In the context of probability theory an essential property of power laws is their so-called *heavy tail*. Its significance can be illustrated by considering two standard examples for a probability density function (PDF), namely the *normal distribution*

$$
P_n(x) = \frac{1}{\sqrt{2\pi\sigma^2}} \exp\left(-\frac{(x - x_0)^2}{2\sigma^2}\right).
\tag{2.69}
$$

and the *lognormal distribution*

$$P_l(x) = \frac{1}{\sqrt{2\pi\sigma^2}} \frac{1}{x} \exp\left(-\frac{(\ln(x/x_0))^2}{2\sigma^2}\right).\tag{2.70}$$

In figure 2.3 the normal distribution and the lognormal distribution are plotted for $x_0 = 1$ and varying $\sigma \in (1, 3, 10)$. For the normal distribution x_0 represents the mean value and σ the standard deviation. Apparently the normal distribution remains quite narrow even for larger values of the standard deviation. The lognormal distribution however becomes a lot broader, meaning it does not fall off so quickly, in comparison to the normal distribution. It produces a *heavy tail* which is longer for larger values of σ. In this double-logarithmic plot the heavy tail resembles a straight line which is the characteristic property of a power law as argued above in figure 2.1.
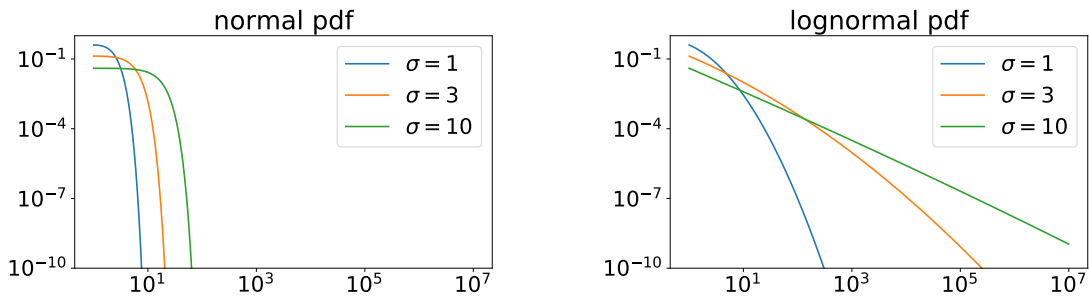
(a) Normal distribution as defined by equation (2.69) for $x > x_0$ and with $x_0 = 1$.

(b) Lognormal distribution as defined by equation (2.70) for $x > x_0$ and with $x_0 = 1$.

Figure 2.3: Here we plot only the range $x > x_0$ for a normal PDF (x_0 = mean value) and lognormal PDF (x_0 is the so-called median which separates lower half from higher half of the PDF). Evidently both PDFs become broader the larger the value for σ. However, in comparison to each other the normal PDF is a lot more narrow then the lognormal PDF. In fact the lognormal produces a *heavy tail* which is very close to a straight line in this double logarithmic plot which is a characteristic property of power laws.

There are two important learnings to take away from this example. First, heavy-tailed PDFs (power laws, lognormal distributions with large σ, ...) carry non-negligible likelihoods for large values in x. This property distinguishes them from the normal distribution which is more narrow around its mean value. Second, although being a characteristic property for power laws, something that looks like a straight line over multiple orders of magnitude in a log-log plot does not have to be generated from a true power law. There are other functions, like the lognormal distribution for example, which are very close to a power law over a large range in x, given the appropriate values of the parameters x_0 and σ.

Here we do not go into further detail but recommend Sornette (2004) for a more thorough treatment of power laws in the realm of probability theory because our main point was to demonstrate the significance of heavy tails and give some examples for their relation to power laws and other PDFs. In the next section we move on to review some essentials about canonical statistical physics which will be generalized in the subsequent chapter.

2.4.2   Boltzmann-Gibbs Statistics

The distribution function $P(\boldsymbol{p}, \boldsymbol{q})$ is a probability density which describes the density of states with respect to a set of variables that characterize the system. Commonly it accounts for the relative number of atoms in a finite volume of position and momentum phase space. The number of particles $\mathrm{d}N$ in the position and momentum interval $\mathrm{d}^3 p\, \mathrm{d}^3 q$ is given by

$$\mathrm{d}N \propto P(\boldsymbol{p}, \boldsymbol{q})\mathrm{d}^3 p\, \mathrm{d}^3 q. \tag{2.71}$$

A well known particular case in Boltzmann-Gibbs statistics is the canonical ensemble, which describes a system of many particles which are in thermal equilibrium with an embedding heat reservoir at constant temperature β^{-1}. The equilibrium distribution for this mechanical system is proportional to the Boltzmann factor $B(E) = e^{-\beta E}$, that is the spectral shape (dependence on energy) of the distribution is characterized by

$$P(\boldsymbol{p}, \boldsymbol{q}) = C(\beta) e^{-\beta E(\boldsymbol{p}, \boldsymbol{q})}, \tag{2.72}$$

which determines the relative frequency of particles with energy E for a given inverse temperature β. In many cases the total energy of a system can be split into a sum of two terms as $E(\boldsymbol{p}, \boldsymbol{q}) = E_{\mathrm{kin}}(\boldsymbol{p}) + E_{\mathrm{pot}}(\boldsymbol{q})$ then the number of particles $\mathrm{d}N$ in the position and momentum interval $\mathrm{d}^3 p\, \mathrm{d}^3 q$ is

$$\mathrm{d}N \propto C_p e^{-\beta E_{\mathrm{kin}}(\boldsymbol{p})} \mathrm{d}^3 p\, C_q e^{-\beta E_{\mathrm{pot}}(\boldsymbol{q})} \mathrm{d}^3 q \tag{2.73}$$

which illustrates the possibility to consider the distribution function separately in position, $P_{\boldsymbol{q}}$, and momentum space, $P_{\boldsymbol{p}}$, with respective normalization constants

$$C_x = \left(\int_{-\infty}^{+\infty} e^{-\beta E(\boldsymbol{x})} \mathrm{d}^3 x \right)^{-1} \tag{2.74}$$

in units of $[C_x]^{-1} = [\boldsymbol{x}]^3$ where x represents q or p. If the energy does not depend on the direction of $\boldsymbol{x}$ it is convenient to choose spherical coordinates where $\int_{-\infty}^{+\infty} \mathrm{d}^3 x = 4\pi \int_0^{+\infty} x^2 \mathrm{d}x$ and

$$C_x = \left(4\pi \int e^{-\beta E(x)} x^2 \mathrm{d}x \right)^{-1} \tag{2.75}$$

In many cases (e.g., ideal gas) the potential energy can be neglected and the kinetic energy depends only on the absolute value of the momentum such that

$$\mathrm{d}N \propto 4\pi C_p e^{-\beta E(p)} p^2 \mathrm{d}p \tag{2.76}$$

which for non-relativistic freely moving ($E_{\mathrm{pot}} = 0$) particles with mass m and kinetic energy $E(p) = p^2/(2m)$ yields the following normalization

$$C_p = \left(4\pi \int_0^\infty e^{-\frac{\beta p^2}{2m}} p^2 \mathrm{d}p \right)^{-1}$$

$$= \left(\frac{2\pi m}{\beta} \right)^{-\frac{3}{2}} \tag{2.77}$$

and is known as Maxwell-Boltzmann distribution in momentum space

$$\mathrm{d}N \propto P_{\boldsymbol{p}}\mathrm{d}^3p = C_p e^{-\frac{\beta p^2}{2m}}\mathrm{d}^3p$$
$$\propto P_p \mathrm{d}p = C_p e^{-\frac{\beta p^2}{2m}} 4\pi p^2 \mathrm{d}p. \tag{2.78}$$

This defines the PDF in momentum space for a non-relativistic particle as $P_p(p) = 4\pi p^2 C_p e^{-\beta p^2/(2m)}$ where the index in our notation[11] reminds us on the fact that $[P_p] = [p]^{-1}$. The analogous distribution in energy space can be calculated from the conservation condition $P_p \mathrm{d}p = P_E \mathrm{d}E$ which yields

$$P_E \mathrm{d}E = P_p \frac{\mathrm{d}p}{\mathrm{d}E}\mathrm{d}E$$
$$= P_p \sqrt{\frac{m}{2E}}\mathrm{d}E$$
$$= \frac{2}{\sqrt{\pi}}\beta^{\frac{3}{2}}e^{-\beta E}\sqrt{E}\mathrm{d}E \tag{2.79}$$

where it is worth emphasizing that in energy space $P_E \propto \sqrt{E} \propto p$ whereas in momentum space $P_p \propto p^2 \propto E$ which we refer to as phase space factor $\rho(p) = p^2$ or $\rho(E) = \sqrt{E}$ which accounts for the density of states in the respective phase space. It is thus important to clarify for a given distribution function which phase space we consider. In many cases this is momentum or another definition of energy.

The classical Maxwell Boltzmann distribution can be brought to a relativistic form where $E = p^2/(2m)$ is replaced by $E = \sqrt{p^2 + m^2}$ (in $c = 1$ units) which was presented by Jüttner (1911). The result for evaluating the integral for the normalization (2.75) can also be taken from Landau and Lifschitz (1979) which yields

$$C_p = \left(\int_0^\infty e^{-\beta\sqrt{p^2+m^2}}4\pi p^2 \mathrm{d}p\right)^{-1}$$
$$\sim \left(\frac{K_0\left(\beta m\right)}{\beta m} + \frac{2K_1\left(\beta m\right)}{(\beta m)^3}\right)^{-1}, \tag{2.80}$$

where K_0, K_1 are modified Bessel functions of the second kind also known as Mac-Donald-functions (p.528, Bronstein et al., 1977). The corresponding distribution function is known as Maxwell Jüttner distribution given by

$$\mathrm{d}N \propto \frac{e^{-\beta\sqrt{p^2+m^2}}}{(\beta m)^{-1}K_0\left(\beta m\right) + 2(\beta m)^{-3}K_1\left(\beta m\right)}\frac{p^2\mathrm{d}p}{m^3}. \tag{2.81}$$

Another more compact way to express the normalization upon ignoring constant factors is

$$C_p \sim \left(\frac{K_2(\beta m)}{\beta}\right)^{-1}, \tag{2.82}$$

---

[11]Some authors prefer a different notation where the distribution function is written as f_p with units $[f_p] = [p]^{-3}$ meaning that $\mathrm{d}N \propto f_p \mathrm{d}^3p$. We choose to include the phase space factor $\rho(p) = p^2$ (special case) or more generally $\rho(x)$ into the definition of our distribution function such that $\mathrm{d}N \propto P_x \mathrm{d}x$ and $P_x(E) = C_x\rho(x)e^{-\beta E(x)}$ is the distribution function where the variable x could be for example the particle's velocity, momentum or kinetic energy.

can be found in Chacón-Acosta et al. (2010). The classical Maxwell Boltzmann distribution and the relativistic Maxwell Jüttner equation differ from each other because of the respective relations between energy and momentum, that is $E = p^2/(2m)$ for classical and $E = \sqrt{p^2 + m^2}$ for relativistic particles.

In summary, the equilibrium distribution of states x (e.g., momenta) can be calculated from

$$P_x(x, \beta) = C_x(\beta)\rho(x)e^{-\beta E(x)} \tag{2.83}$$

with normalization $C_x(\beta) = (\int \rho(x)e^{-\beta E(x)}\mathrm{d}x)^{-1}$. In this notation the Maxwell Boltzmann distribution in momentum space is written as

$$P_p(E(p)) = C_p(\beta)\rho(p)e^{-\beta E(p)} \tag{2.84}$$

with $C_p(\beta) = (2\pi m/\beta)^{-3/2}$, phase space factor $\rho(p) = 4\pi p^2$ and energy $E(p) = p^2/(2m)$. In the following section we introduce superstatistics which allows us to treat non-equilibrium systems and determine the corresponding distribution functions.

2.4.3 Superstatistics

The general idea of superstatistics is that the observed nonequilibrium distribution results from a superposition of equilibrium distribution functions that are individually associated with an inverse temperatures β. Whereas the canonical ensemble in Boltzmann Gibbs statistics applies to a many particles system embedded within a larger heat bath at constant temperature, superstatistics addresses an ensemble of canonical ensembles by introducing a distribution of inverse temperature which can vary in time and/or space.

As a concrete example consider a cosmic ray detector which counts the number of particles within a given energy range. These particles originate from various cosmic environments with different temperatures. If there is a large enough spatial volume at constant temperature, and enough time to distribute the energy, then equilibrium thermodynamics would predict a distribution of energies characterized by $e^{-\beta E}$ energy dependence. Hence, for each energy distribution of cosmic rays coming from a particular equilibrium environment at constant temperature we associate a Boltzmann factor $B(E) = e^{-\beta E}$. Considering large enough environments, with different equilibrium temperatures, should then lead to observing superposition of equilibrium distributions because our detector here on Earth does not distinguish individual particles from different environments but only counts the total number of particles with energy E.

Drawing back on the previous section on Boltzmann Gibbs statistics, we can define a conditional PDF

$$p_E(E|\beta) = C(\beta)\rho(E)e^{-\beta E}. \tag{2.85}$$

which is essentially the Maxwell Boltzmann distribution for an ideal gas at constant temperature $T = \beta^{-1}$ (in units $[T] = \mathrm{eV}$) with the characteristic Boltzmann factor $B(E) = e^{-\beta E}$ and normalization constant

$$C_p(\beta) = \left(\int_{-\infty}^{+\infty} e^{-\beta E(\boldsymbol{p})}\mathrm{d}^3 p \right)^{-1}. \tag{2.86}$$

Superstatistics derives a generalized Boltzmann factor by superimposing the underlying conditional distributions $p_E(E|\beta)$ with an appropriate weight accounting for the distribution of β. Beck and Cohen (2003) distinguish between type-A and type-B superstatistics which differ in their respective weight when summing up the conditional distributions to obtain the accumulated and observable energy distribution. Here we use superstatistics type-B which integrates the locally normalized distribution functions (2.85) over the distribution of inverse temperatures in the following way

$$P_E(E) = \int_0^\infty g(\beta)p_E(E|\beta)\mathrm{d}\beta. \tag{2.87}$$

In order to solve this equation one needs to specify the relation between energy and momentum $E(\boldsymbol{p})$ and the distribution of inverse temperatures $g(\beta)$. Different classes of distributions were investigated in detail by Beck and Cohen (2003) who showed that χ^2-distributed inverse temperature distributions naturally generate asymptotic power laws in the resulting superimposed distribution function. That is, for a sum a of independent and identically distributed Gaussian random variables X_i with

$$\beta = \sum_{i=1}^n X_i^2, \tag{2.88}$$

the corresponding PDF is a χ^2-distribution (see Beck (2004)) written as

$$g(\beta) = \frac{1}{\Gamma(n/2)}\left(\frac{n}{2\beta_0}\right)^{\frac{n}{2}}\beta^{\frac{n}{2}-1}e^{-\frac{n\beta}{2\beta_0}}, \tag{2.89}$$

with the mean inverse temperature defined as

$$\beta_0 = \int_0^\infty \beta g(\beta)\mathrm{d}\beta = T_0^{-1}. \tag{2.90}$$

In order to calculate the normalization $C_p(\beta)$ one generally has to distinguish between three different regimes:

1. Newtonian: $E = \frac{p^2}{2m}$

2. Relativistic: $E = \sqrt{p^2 + m^2}$

3. Ultra-relativistic ($p \gg m$): $E = p$.

The normalization in the Newtonian regime was calculated in (2.77) for the example of the Maxwell Boltzmann distribution. For the relativistic case we identified the Maxwell Jüttner distribution with corresponding normalization (2.80). For cosmic rays we are only concerned with relativistic and ultra-relativistic particles. In agreement with Beck (2004), we use the ultra-relativistic energy momentum relation, which implies $p^2\mathrm{d}p = E^2\mathrm{d}E$, and allows to calculate the β-dependent normalization simply as

$$\begin{aligned}C_p(\beta)^{-1} &= \int_0^{+\infty} e^{-\beta E}E^2\mathrm{d}E \\ &= 2\beta^{-3}.\end{aligned} \tag{2.91}$$

Putting everything together we can determine the distribution function (2.87), given the particular normalization (2.91) and the χ^2-distributed inverse temperature distribution (2.89), with the following calculation.

$$
\begin{aligned}
P_E(E) &= \int_0^\infty g(\beta)p_E(E|\beta)\mathrm{d}\beta \\
&= \frac{1}{\Gamma(n/2)}\left(\frac{n}{2\beta_0}\right)^{\frac{n}{2}}\int_0^\infty \beta^{\frac{n}{2}-1}e^{-\frac{n\beta}{2\beta_0}}\frac{\beta^3}{2}\rho(E)e^{-\beta E}\mathrm{d}\beta \\
&= \rho(E)\frac{1}{2\Gamma(n/2)}\left(\frac{n}{2\beta_0}\right)^{\frac{n}{2}}\int_0^\infty \beta^{\frac{n}{2}+2}e^{-\beta\left(E+\frac{n}{2\beta_0}\right)}\mathrm{d}\beta \\
&= \rho(E)\frac{\Gamma(3+\frac{n}{2})}{2\Gamma(n/2)}\left(\frac{n}{2\beta_0}\right)^{\frac{n}{2}}\left(E+\frac{n}{2\beta_0}\right)^{-3-\frac{n}{2}} \\
&\sim \rho(E)\left(\frac{n}{2\beta_0}\right)^{\frac{n}{2}}\left(E+\frac{n}{2\beta_0}\right)^{-3-\frac{n}{2}}.
\end{aligned}
\tag{2.92}
$$

In the last line we have dropped the term with the Gamma functions because it is a constant global factor which is irrelevant for the spectral shape (energy dependence) of the distribution. Introducing $q = 1+2/(n+6)$ (equivalent to $n/2+3 = 1/(q-1)$) and $b = \beta_0/(4-3q)$, allows us to express the result as

$$
\begin{aligned}
P_E(E) &\sim \rho(E)\left(\frac{n}{2\beta_0}\right)^{-3}\left(\frac{n}{2\beta_0}\right)^{\frac{1}{q-1}}\left(E+\frac{n}{2\beta_0}\right)^{\frac{-1}{q-1}} \\
&\sim \rho(E)\left(\frac{n}{2\beta_0}\right)^{-3}\left(\frac{\frac{n}{2\beta_0}}{E+\frac{n}{2\beta_0}}\right)^{\frac{1}{q-1}} \\
&\sim \rho(E)\left(\frac{n}{2\beta_0}\right)^{-3}\left(\frac{1}{1+E\frac{2\beta_0}{n}}\right)^{\frac{1}{q-1}} \\
&\sim \rho(E)\left(1+(q-1)bE\right)^{\frac{1}{1-q}} = \rho(E)e_q^{-bE}.
\end{aligned}
\tag{2.93}
$$

In the last step we have again dropped an irrelevant constant factor, that is $(n/2\beta_0)^{-3}$, and we have introduced the q-exponential defined by

$$
e_q^x := (1+(1-q)x)^{\frac{1}{1-q}}.
\tag{2.94}
$$

The so-called *entropic index* q determines the high-energy behavior of the distribution (i.e., the fat tail of the PDF) since the q-exponential asymptotically approaches a power law

$$
\lim_{E\to\infty} e_q^{-bE} \propto E^\gamma
\tag{2.95}
$$

with spectral index $\gamma = 2 - 1/(q-1)$ for $q > 1$, whereas for $q = 1$ we recover the canonical Boltzmann factor

$$
\lim_{q\to 1} e_q^{-bE} = e^{-bE}.
\tag{2.96}
$$

We introduce a constant C for the global amplitude as physically meaningless fitting factor (because it is irrelevant for the spectral shape which is the focus of our

analysis) in order to write down the final expression for our distribution function based on χ^2-superstatistics as

$$P_E(E) = C\rho(E)e_q^{-bE} \tag{2.97}$$

and summarize the following formulae

$$\beta = \sum_{i=1}^{n} X_i^2, \tag{2.98}$$

$$\beta_0 = \int_0^\infty \beta g(\beta)\mathrm{d}\beta = T_0^{-1}, \tag{2.99}$$

$$b = \frac{\beta_0}{4 - 3q} = T^{-1}, \tag{2.100}$$

$$n = \frac{2}{q - 1} - 6., \tag{2.101}$$

which we exploit for interpreting the physical meaning of the parameters inferred from the observed for cosmic ray spectra in section 3.3.

Chapter 3

Cosmic Rays

3.1 Observations

Cosmic rays (CRs) are fast moving charged particles coming from space and carrying energies ranging from 10^6 eV to 10^{20} eV which is exceeding the most powerful human made particle accelerators by multiple orders of magnitude. Protons, meaning ionized hydrogen nuclei, are the most abundant CRs but all sorts of atomic nuclei, electrons and their corresponding anti particles are found. CRs can be detected directly in space (e.g., the Alpha Magnetic Spectrometer (AMS) on the International Space Station) outside of Earth's magnetic field and atmosphere which operate like a safety shield against CRs, or with ground based detectors via the secondary particle showers which are triggered when CRs collide with other particles in the atmosphere. With an extensive analysis the type of particle and its energy before colliding can be reconstructed (e.g., by the Pierre Auger Observatory in Argentina). The presence of CRs outside of our solar system can be inferred indirectly by investigating the electromagnetic radiation emitted due to acceleration or collision with other particles.

In the following we present an overview about the essential observable properties, the CR energy spectrum, the relative abundance of various particle species, and the spectrum of CR induced electromagnetic radiation, namely radio, x-rays and gamma rays. In the subsequent section 3.2 we present the so-called *standard paradigm* for the origin of galactic CRs (e.g., Gabici et al., 2019) and show how it builds on the observational evidence gathered in the previous section. Our main focus is to find a model which allows to interpret the origin of the observed power law energy spectrum. For this purpose we provide a novel interpretation by applying a model based on superstatistics, which was introduced in section 2.4.3.

3.1.1 Energy spectrum and isotropy of cosmic ray (CR) flux

Figure 3.1 presents the flux of CRs spanning eleven orders of magnitude in energy which resembles a single power law at first look (left plot) whereas many more details can be discovered when considering different energy ranges and particle types more closely (right plot). The observed spectrum here at Earth carries valuable information in particular about CR acceleration and transport because both processes are in general energy or rigidity (momentum per charge) dependent. For example a gradual shift to a steeper spectrum for larger energies could hint on either: a) less efficient acceleration for higher energetic particles or b) larger losses for higher
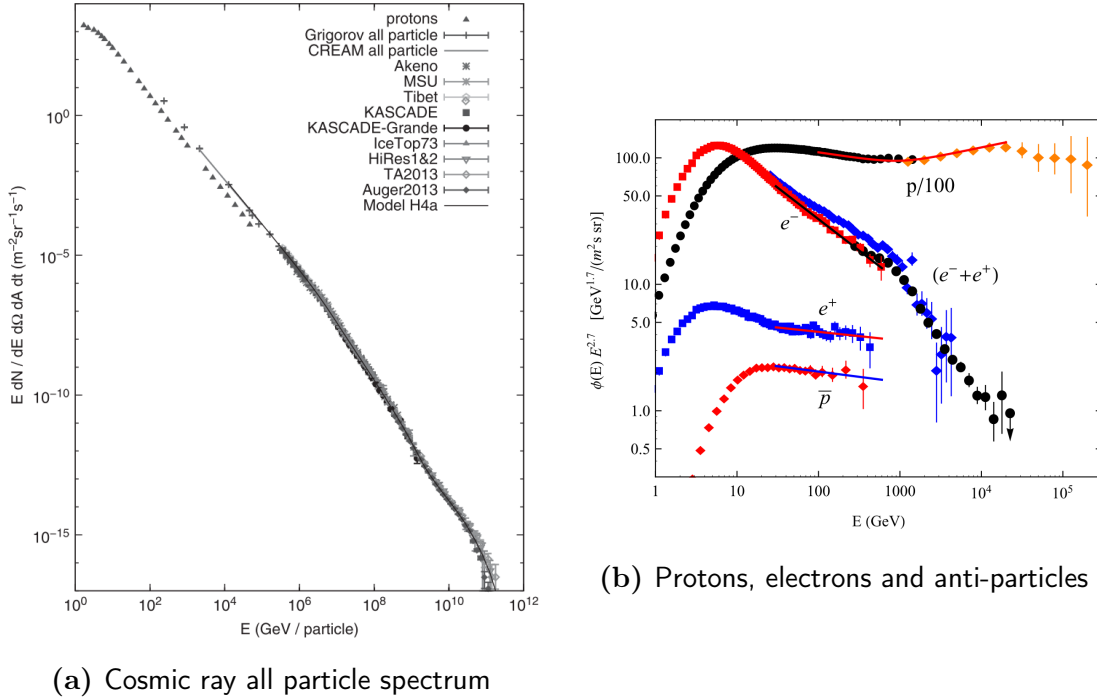
(a) Cosmic ray all particle spectrum

(b) Protons, electrons and anti-particles

Figure 3.1: The all particle cosmic ray flux illustrates a remarkably broad power law dependence on energy (left plot, taken from Gaisser et al., 2016). A closer look shows the spectrum becomes steeper for $E \gtrsim 1 \times 10^6 \, \text{GeV}$ (the so-called *knee*) and again flatter for $E \gtrsim 1 \times 10^9 \, \text{GeV}$ (the so-called *ankle*). Distinguishing between different types of particles (right plot, taken from Gabici et al., 2019) reveals more subtle spectral features.

energetic particles. The latter could result from energy losses during propagation or from escaping particles. Evidently the observed spectrum here at Earth can be affected by multiple processes along the way (e.g., diffusion, reacceleration, convection, collisions, radiative losses) and it is quite challenging to disentangle them. In general the particular spectral features of different particle types (e.g., electrons, protons, carbon, boron) provide strong constraints to any cosmic ray model.

The low energy range with $E \lesssim 10 \, \text{GeV}$ is affected by the influence of the solar wind and the sun's magnetic field (Moraal, 2014). The flux in this energy region thus becomes modified and time dependent and has to be corrected by applying solar modulation models (e.g., Boschini et al., 2017) or by Voyager 1 and 2 measurements (e.g., Cummings et al., 2016; Stone et al., 2019) in order to gain knowledge about the CR spectrum outside of the heliosphere.

Another important piece of the puzzle is the energy dependent degree of anisotropy of the flux. Impressively cosmic rays appear to reach Earth from all directions at nearly equal amplitude with deviations of only 10^{-4} for protons at tens of TeV (Gabici et al., 2019). Therefore cosmic ray models must explain both, the high degree of isotropy and the energy dependent low level of anisotropy.

3.1.2 Elemental and isotopic composition of CR flux

Figure 3.2 compares the abundance of different nuclei in CRs with the abundance of chemical elements in our solar system. Evidently there is a strong correlation for many chemical elements whereas for lithium, beryllium and boron, for example, their relative abundance exceeds the solar system reference value by at least four
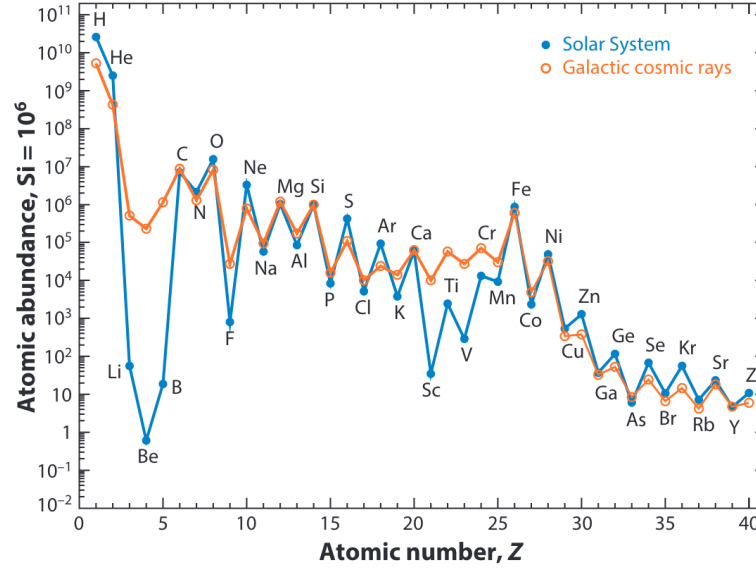
Figure 3.2: Comparing the relative abundance of chemical elements in our solar system with detected cosmic rays allows to infer essential information about their propagation. The overabundance of lithium (Li), beryllium (Be) or boron (B) in CRs can be explained as a product of CR collisions with interstellar gas. Plot taken from Tatischeff and Gabici (2018).

orders of magnitude. In fact, these elements are not among the typically produced elements from stellar nuclear fusion but they must be the result of CRs colliding with interstellar gas particles such that larger nuclei fragment into smaller ones. This so-called *spallation* process is the dominant production mechanism for elements like lithium, beryllium and boron, which are therefore called *secondary* cosmic rays.
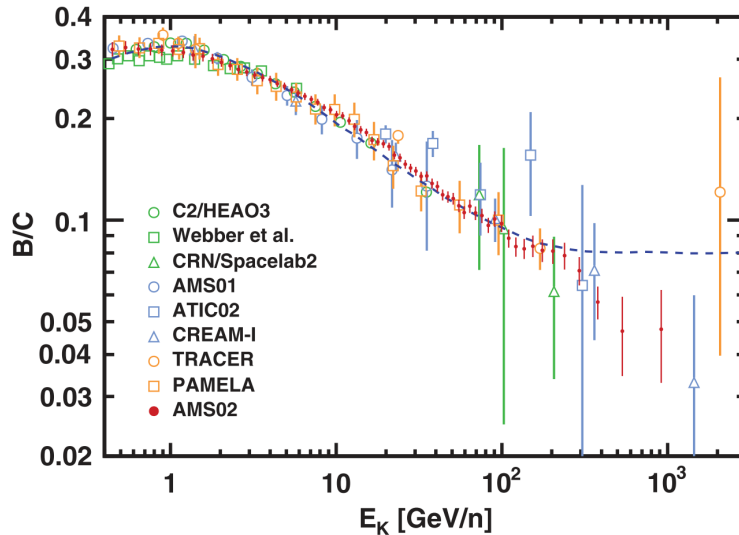
Figure 3.3: The flux ratio of boron to carbon with measurements since 1980 with AMS-02 (red points) providing the most recent and precise values. The dashed line corresponds to a CR propagation model with constant boron to carbon ratio for larger energies which is in contradiction to the AMS-02 data. The energy variable E_K is kinetic energy per nucleon. Plot taken from Aguilar et al. (2016).

Figure 3.3 shows the flux ratio of boron to carbon over three orders of magnitude in kinetic energy per nucleon and carries valuable information about CR propaga-

Figure 3.4: Secondary to primary ratio with scandium (Sc), titanium (Ti), vanadium (V) (all secondary) and primary iron (Fe). The decreasing flux ratio is similar to the behaviour of boron to carbon in figure 3.3. Graphic by Strong et al. (2007).

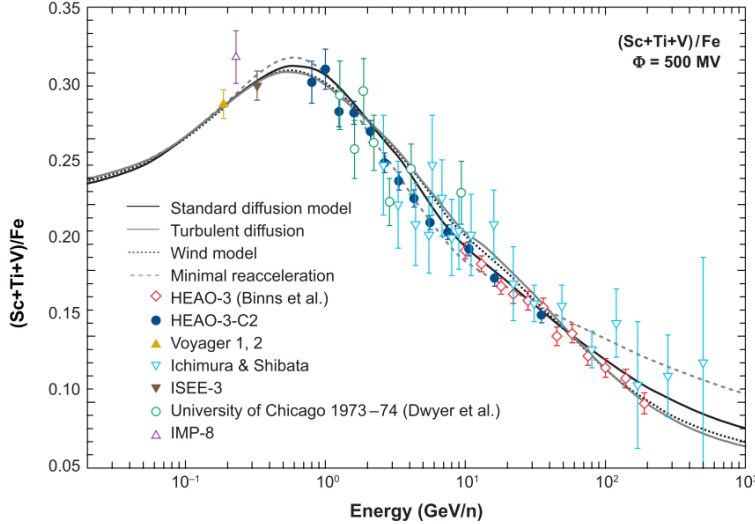tion. Whereas boron is entirely of secondary origin (a product from spallation) (Strong et al., 2007), carbon is dominantly of primary origin.[1] Next to nitrogen and oxygen, carbon is also one of boron's parent nuclei. When we speak of primary cosmic rays we refer to atomic nuclei which are accelerated at their sources and have maintained their identity (no spallation) until being observed, directly or indirectly (Strong et al., 2007). In general kinetic energy per nucleon is conserved in spallation reactions (e.g., Kachelriess and Semikoz, 2019) and therefore the spectrum of a type of primary CR will be inherited by their offspring, the secondary CRs, at least in the absence of further complications as for example multiple production channels. In this case a constant secondary to primary ratio would be expected when detecting the CRs shortly after their production. In reality we detect the secondary CRs at a random time sooner or later after their production. The observed spectrum is therefore modulated by energy dependent processes along the way. A decreasing secondary to primary flux could for example hint on either of the following two scenarios: a) higher energetic primary CRs are less abundant in the environments suitable for production of secondaries or b) the differential cross sections for producing secondaries decrease for higher energies. The latter explanation is usually rejected but to our best knowledge there is still a considerable uncertainty about the exact energy dependence of cross sections for all relevant (hadronic) production channels (e.g., Génolini et al., 2018). Considering further combinations of secondary to primary ratios (see figure 3.4), apart from boron to carbon, allows to test if the observed energy dependence of the decreasing flux truly carries information about CR transport in general, which we discuss further in section 3.2.2.

Unstable isotopes in secondary CRs can be used to infer knowledge about the propagation time. For that purpose the abundance of the unstable ^{10}Be isotope with a lifetime $\tau_{1/2} \sim 1\,\mathrm{Myr}$ can be compared to the abundance of stable ^{9}Be in CRs as shown in figure 3.5.

---

[1]For lower energies (at about $1\,\mathrm{GeV}$/nucleon) there can be a substantial ($\sim 20\%$) contribution of secondary carbon according to Génolini et al. (2018).
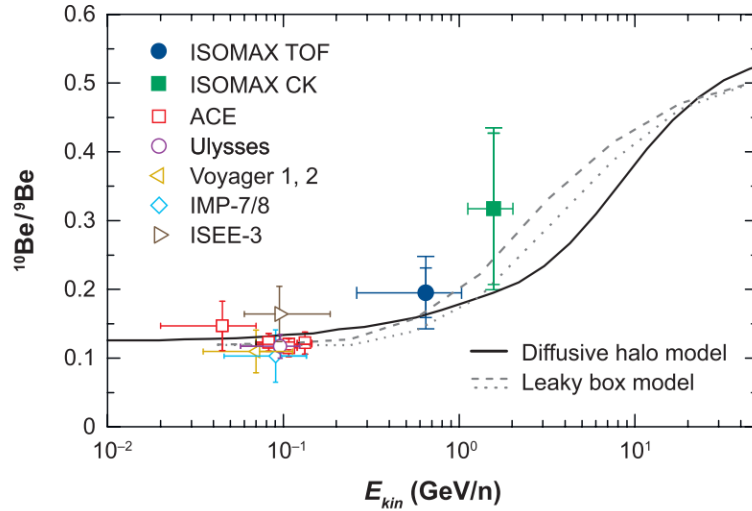
Figure 3.5: The ratio of unstable ^{10}Be to stable ^{9}Be carries information about the propagation time of secondary CRs. An increasing ratio with energy is expected due to increased half life for larger Lorentz factors. Graphic by Strong et al. (2007).

3.1.3 Radio, x-rays and gamma rays induced by CRs

There are two important mechanisms by which CRs can produce electromagnetic radiation, namely through collision with other particles or due to acceleration. CRs carry charge and therefore interact with electromagnetic fields like the magnetic field in our galaxy. Due to the Lorentz force, which acts on all charged particles moving (to some degree) perpendicular to a magnetic field, the CRs gyrate around the field lines and emit synchrotron radiation. Furthermore, CRs are also accelerated due to scattering with other charges or irregularities in the magnetic field and radiate bremsstrahlung. Another important mechanism is CR scattering off lower energy photons (background radiation) which is called inverse compton scattering when the momentum is transferred from CR to photon. Additionally, CRs can interact with other particles via the strong nuclear force and produce new hadrons (e.g., atomic nuclei or pions), leptons and ultimately photons (e.g., gamma rays). In order to infer the presence of CRs in far away regions it is necessary to develop models which calculate the spectrum of the radiation in dependence on parameters associated with the properties of the surrounding environment and the CRs. These models are commonly composed of two scenarios: a leptonic and a hadronic scenario.

Hadronic scenarios account for gamma ray emission due to proton-proton collisions which produce neutral pions that are unstable and decay into gamma ray photons with a spectrum parallel to their progenitors for large enough energies. This process has a characteristic peak at the rest mass energy of the neutral pion $m_{\pi^0} \approx 67.5\,\mathrm{MeV}$ which can be exploited to distinguish the gammas rays from an alternative origin like electron bremsstrahlung (e.g., Ackermann et al., 2013).

Leptonic scenarios account for synchrotron radiation, inverse compton scattering and thermal and nonthermal bremsstrahlung. Applying hadronic and leptonic models jointly to an observed spatially integrated radiation spectrum like in figure 3.6 allows to (partially) reconstruct the energy spectrum of leptons and hadrons which are responsible for the electromagnetic radiation.
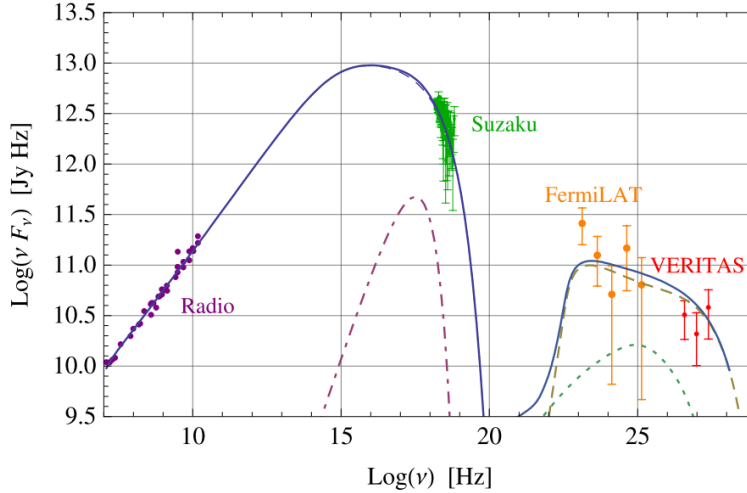
Figure 3.6: The spatially integrated spectral energy distribution of Tycho's SNR (purple), x-ray (green), GeV (orange) and TeV (red) gamma rays reveals the presence of accelerated charged particles, namely CRs. The solid line is the best fit with a model dominated by synchrotron radiation in the radio and x-ray and pion decay induced gamma radiation. Graphic by Morlino and Caprioli (2012).

3.1.4   Questions

Having discussed the observational data for CRs there are some fundamental questions which arise naturally as for example the following:

1) Where do CRs originate from?

2) How are CRs accelerated?

3) How do CRs propagate from sources to observation sites?

During the last fifty years a so-called *standard paradigm* (e.g., Gabici et al., 2019) has established for answering these (and many other) questions. In short the answers can be summarized as follows:

1) CRs with energies $E \lesssim 10^{15-17}$ eV are mainly of galactic origin

2) where they experience diffusive shock acceleration in supernova remnants until they escape into the surrounding medium and

3) propagate diffusively through the galactic disk and a magnetized halo with a few kiloparsec scale height.

Despite considerable progress in CR research there are still many open question that are actively under debate. Gabici et al. (2019) present a detailed review about the observational and theoretical pieces which are in tension with each other. The authors conclude that it is not yet clear if the paradigm can be maintained or if some of its cornerstones must be replaced. The improvements in observational techniques and accuracy have furthermore allowed to define much more specific questions than we consider here. We will mainly focus on the observed power law energy spectra here at Earth and aim to understand the dominant mechanisms behind it.

3.2 Standard paradigm interpretation of energy spectra

3.2.1 Diffusive shock acceleration

The overall shape of the CR energy spectrum, with its heavy tail, immediately tells us this is not a thermal distribution, meaning the momentum (or energy) distribution associated with an ideal gas at constant temperature, which is characterized by an exponential decay for larger energies (see section 2.4.2). In fact, regardless of the spectral shape but merely the presence of such enormously high energies in CRs could not be explained as thermal origin even with the hottest large scale gas reservoirs in our galaxy - like the hot ionized medium - with temperatures of $T \sim 10^6$ K are associated only with a mean kinetic energy per particle of $k_B T \sim 10^{-4}$ MeV and thus multiple orders of magnitude below the characteristic energies of CRs. Therefore a powerful source of nonthermal energy is needed to explain the energy distribution of cosmic rays.

Estimating the power required for CR acceleration sources to maintain a stationary state of cosmic ray energies relies on specifying the volume, V, with average CR energy density, $\mathcal{E}_{CR}$, and the mean time the CRs reside within that volume, τ_{res}. For our Galaxy the average CR energy density is roughly (e.g., Ferrière, 2001; Cummings et al., 2016)

$$\mathcal{E}_{CR} \sim 1 \, \text{eV} \, \text{cm}^{-3} \sim 1.6 \times 10^{-12} \, \text{erg/cm}^3. \tag{3.1}$$

Maintaining this energy density consequently requires a source which balances the average power carried away by the CRs escaping from the volume, which is

$$\Gamma_{CR} = \frac{\mathcal{E}_{CR} V}{\tau_{res}} \sim 5 \times 10^{40} \, \text{erg/s} \tag{3.2}$$

with CR residence timescale $\tau_{res} = 6$ Myr (see equation (3.15) in next section), a galactic disk with radius $r = 15$ kpc and scale height $h = 300$ pc. Evidently, the power required to maintain the observed energy density, $\mathcal{E}_{CR}$, is about ten percent of the galactic average power contribution to kinetic energy by SNe as calculated in equation (1.3).

For the acceleration of CRs it has become broadly accepted that shock fronts in SNRs provide a suitable environment (Reynolds, 2008).[2] Magnetic field irregularities and fluctuations (e.g., Alfvén waves) in the proximity of the shock front isotropise the particle distribution and eventually deflect some of the particles back across the shock front. The original idea of diffusive acceleration by reflecting CRs via magnetized clouds in the ISM goes back to Fermi (1949). Building on this approach Bell (1978) and Blandford and Ostriker (1978) both showed with quite different derivations that diffusive acceleration in strong shocks generate power law energy spectra with universal spectral index under quite general conditions. This process is generally (not only for strong shocks) known as diffusive shock acceleration (DSA). In the following we consider the derivation by Bell (1978) which is nicely presented in Gaisser et al. (2016).

---

[2]Not only super novae but also novae, caused by accreting white dwarfs in binary systems, are capable of accelerating cosmic rays as recent observational evidence presented by Aharonian et al. (2022) shows.
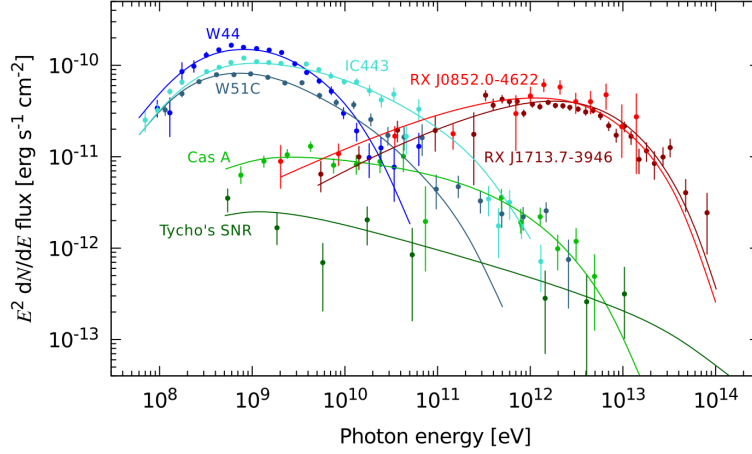
Figure 3.7: The gamma ray emission of various SNR presented as differential number density with the canonical E^{-2} scaling which implies that the spectrum predicted by DSA corresponds to a straight horizontal line. Given are three old SNRs (order 10.000 years, W44, IC443 and W51C) with low-energy cutoffs, young SNRs with flat spectra and high-energy cutoffs (Tycho and CasA) as well as flat sources with TeV-energy turnovers (RX J0852.0-4622 and RX J1713.7-3946). Graphic by Becker Tjus and Merten (2020).

Consider a charged particle moving in the vicinity of the expanding shock front in a supernova remnant. On either side of the shock the particle will encounter magnetic field irregularities or MHD (magneto-hydrodynamic) waves which deflect the particle. With a finite probability the particle will be deflected backwards such that it crosses the shock front another time. Each passage (going back and forth) increases the particle's momentum by a factor $\xi = \Delta E / E$ such that after n cycles a particle with initial energy E_0 has

$$E = E_0 (1 + \xi)^n \tag{3.3}$$

and solving this equation for the number of cycles yields

$$n = \frac{\ln\left(\frac{E}{E_0}\right)}{\ln(1 + \xi)}. \tag{3.4}$$

Given that the probability for the particle to escape during one passage is P_{esc} the probability for the particle to remain in the acceleration region for n passages until it has reached the energy E is given by $(1 - P_{\text{esc}})^n$. From this we can estimate the scaling of the number of particles which gain at least this amount of energy as [3]

$$N(\geq E) \propto \sum_{m=n}^{\infty} (1 - P_{\text{esc}})^m = \frac{(1 - P_{\text{esc}})^n}{P_{\text{esc}}} \tag{3.5}$$

---

[3]Usually we consider the number of particles $\mathrm{d}N$ in a finite energy interval $\mathrm{d}E$ instead of considering all particles with energies $\geq E$ but the difference in the following derivation is negligible because the contributions of $\sum_{m=k}^{\infty}(1 - P_{\text{esc}})^m \ll \sum_{m=n}^{k}(1 - P_{\text{esc}})^m$ for sufficiently large k which is guaranteed by considering a sufficiently broad energy range $\mathrm{d}E$ by which we define the particle density $\mathrm{d}N/\mathrm{d}E$.

where the latter equality holds generally for $|1 - P_{\text{esc}}| < 1$. We can then use equation (3.4) to eliminate n and find

$$N(\geq E) \propto \frac{(1 - P_{\text{esc}})^{\frac{\ln(E/E_0)}{\ln(1+\xi)}}}{P_{\text{esc}}} = \frac{1}{P_{\text{esc}}} \left(\frac{E}{E_0}\right)^{-\delta} \tag{3.6}$$

where we have used $x^{\ln(a)} = a^{\ln(x)}$ and introduced the spectral index

$$\delta = \frac{\ln\left(\frac{1}{1-P_{\text{esc}}}\right)}{\ln(1+\xi)} \approx \frac{P_{\text{esc}}}{\xi}. \tag{3.7}$$

The spectral index of the accelerated CRs can thus be calculated from the escape probability weighted by the average energy gain per passage. The derivation rests on applying the Lorentz transformations and integrating over all possible "scattering angles" (collisionless deflection) which is found in Gaisser et al. (2016) and yields

$$P_{\text{esc}} = \frac{4u_2}{c}$$
$$\xi \sim \frac{4}{3}\beta \tag{3.8}$$

with $\beta c = (u_1 - u_2)$ being the velocity of the unshocked gas "upstream" (u_1) relative to the shocked gas "downstream" (u_2) and c velocity of light. Introducing the compression factor $r = \rho_2/\rho_1$ and using the continuity equation $u_1/u_2 = \rho_2/\rho_1 = r$ yields

$$\delta = \frac{3}{r-1}. \tag{3.9}$$

The compression factor r depends on the adiabatic index $\kappa = c_p/c_v$ of the gas and the Mach number $M = u_1/c_s$ according to Shore (1992) as

$$r = \frac{(\kappa + 1)M^2}{(\kappa - 1)M^2 + 2}. \tag{3.10}$$

For a monoatomic nonrelativistic gas $\kappa = 5/3$ we find in the strong shock limit with $M \gg 1$ that $r = \frac{4}{1+3/M^2} \approx 4$ and thus

$$\delta \approx 1. \tag{3.11}$$

This result can be equivalently expressed with respect to the differential number density (with $\gamma = \delta + 1$) as

$$\mathcal{N}(E) = \frac{\text{d}N}{\text{d}E} \propto E^{-\gamma}, \tag{3.12}$$

where $\gamma \approx 2$. It is quite remarkable that the spectral index depends only the compression ratio of the shock. The acceleration spectrum is therefore fully determined by properties of the accelerator itself, that is the shock front and the surrounding ISM.

This prediction of DSA in the strong shock limit can be tested with the observed emission spectra of SNRs. As described above this is done by fitting models for leptonic and hadronic scenarios on the observed radio, x-ray and gamma ray spectra.

Figure 3.7 presents the gamma ray spectra (as tracers for the CR spectral index) for various older and younger SNRs and reveals that the spectral index is somewhere around $\gamma \sim 2$ as predicted by DSA but only for certain energies and types of SNRs. In fact these deviations are no surprise for various reasons. First, SNRs can be characterized by various evolutionary stages which differ strongly when comparing a few hundred years old SNRs (Tycho, Cas A) with ten thousand years old SNRs (W44, IC443, W51C) and furthermore there are different types of SNRs as illustrated by the diversity of images in figure 3.8. Second, the spectrum predicted by DSA corresponds to an average over time in contrast to the snapshot we take with our gamma ray observations. Third, the assumptions that went into the above derivation are highly idealized and ignore many other important aspects as we discuss in the following.
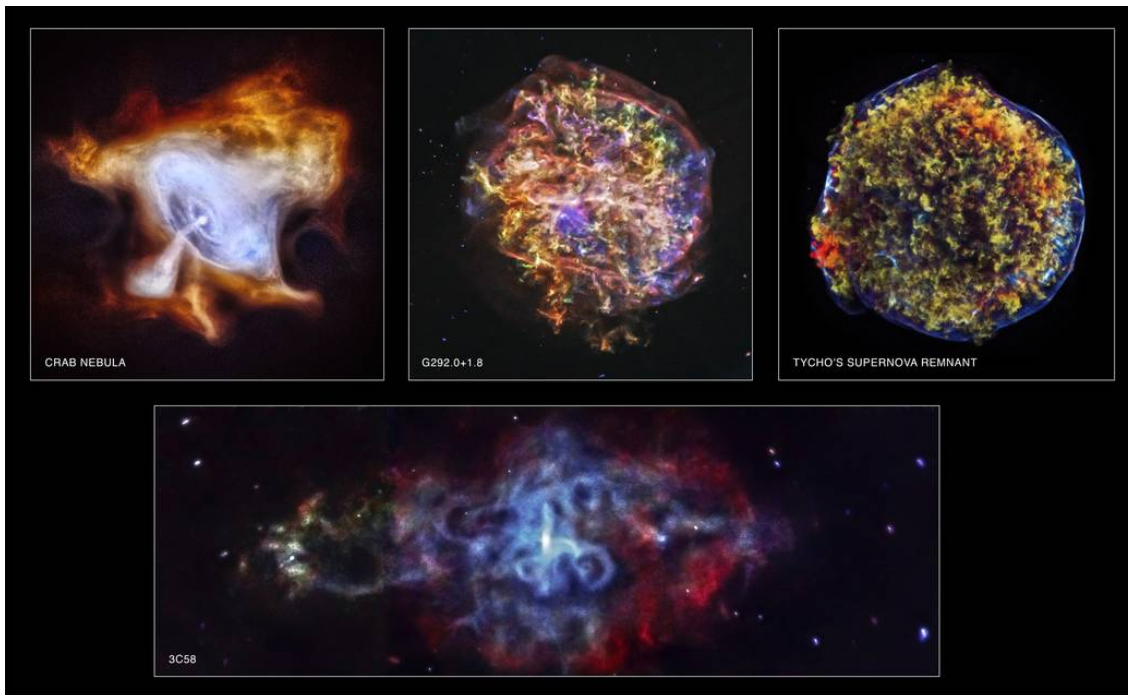
Figure 3.8: These Chandra x-ray images illustrate the diversity of super nova remnants. Image credit: NASA/CXC/SAO.

The above derivation for DSA treated CRs as test particles which become confined by MHD waves in the environment and accelerated by passing over the infinitely wide and plane shock front which propagates perpendicular to the regular ambient magnetic field. Basically all these assumptions are violated for real SNRs. Considering weaker shocks or SNRs at later times corresponds to lower mach numbers which leads to $\gamma > 2$ meaning steeper spectra. On the other hand the back reaction of cosmic rays on the shock front, which is accounted for in nonlinear DSA models (e.g., Malkov and Drury, 2001), could modify the spectrum (e.g., make it concave according to Recchia and Gabici, 2018). Using a semi-analytic model of nonlinear DSA Diesing and Caprioli (2021) derive injection spectra with $2.1 \leq \gamma \leq 3.0$ dependent on the particular properties of the SNRs and $\gamma \sim 2.2$ for average older SNRs with moderate expansion velocities which make a significant contribution in our Galaxy.

Another mechanism which is neglected in the simple test particle approach of DSA is the possibility of self generated Alfvén waves by the CRs via the streaming

instability which was already noted by Bell (1978) when introducing DSA. According to Malkov and Drury (2001) the following three conditions are required for DSA to work efficiently: "(i) at least a few thermal particles downstream must be able to return upstream; (ii) the accelerated particles must not propagate freely to keep crossing the shock; and (iii) if many particles are accelerated to high energies, their pressure must not smear out the shock completely".

Another questionable assumption in our derivation concerns the escape probability $P_{\text{esc}} \approx \xi$ depends only on the relative energy increase per passage that is

$$\xi = \frac{4(u_1 - u_2)}{3c} = \frac{4u_2}{c}. \tag{3.13}$$

The probability for the particle to escape the acceleration region is thus independent of its energy.[4] This property was already mentioned in the original paper by Bell (1978) but it is worth to be critically questioned because the mechanisms for diffusion and confinement typically are energy dependent as we will see in the next section. Other additional factors are the obliquity of the shock and the impact of turbulent magnetic field amplification in the vicinity of the shock as investigated by Xu and Lazarian (2022b).

Amato and Casanova (2021) describe how the escaping CRs may provide an important mechanism for self regulation of the acceleration system. In this perspective a large escape probability allows the escaping CRs to generate more Alfvén waves via the streaming instability which reacts back onto the CR current by confining the particles and thereby reducing the escape probability and consequently lowering the rate of self generated Alfvén waves which again increases the escape probability. In this way the acceleration system as a whole could self regulate the escape probability to a nearly constant value over time. However, CR confinement via self generated Alfvén waves is an energy dependent process and thus we would also expect an energy dependent escape probability in contrast to the DSA assumptions above.

In summary, diffusive shock acceleration provides important insights into the physical mechanisms behind CR acceleration. Nevertheless, many questions remain open like the effect of CR back reactions (e.g., Blasi, 2019a), magnetic field amplification (e.g., Bell, 2004; Schure et al., 2012) and the maximum acceleration energy (e.g., Tatischeff and Gabici, 2018). The observational evidence shows that SNRs in fact accelerate CRs and that the observed injection spectrum $E^{-2.1} - E^{-2.5}$ is slightly steeper than the strong shock limit prediction by DSA. On the other hand, CRs might additionally be accelerated in different environments like in shock fronts of super bubbles, in stellar wind or near the galactic centre, with possibly different spectra, and it is not yet decided if SNRs are indeed the dominant contributors to the galactic CRs observed at Earth (e.g., Gabici et al., 2019). Evidently there is yet not enough observational evidence for a universal source spectrum of CRs which could be simply compared to the observed spectrum at Earth in order to specify the spectral modification due to CR propagation which we address in the next section.

3.2.2 Diffusive transport

Cosmic rays do not propagate through the galaxy in straight lines because they carry electric charge and therefore unavoidably gyrate around the ambient magnetic

---

[4]More generally the escape probability would be $P_{\text{esc}} = 4u_2/v$ for a particle with velocity v whereas we have limited our treatment on the relativistic case where $v \approx c$.

field lines. Additionally they interact with the irregularities of the magnetic field lines and with MHD waves like magnetosonic or Alfvénic waves. Here we do not go into the details of diffusive transport but refer to a more complete treatment in the textbook Schlickeiser (2002). We follow a rather phenomenological approach and simply acknowledge that any CR transport model must account for (collisionless) diffusion and additionally for collisions of CRs with the ambient gas. Both processes are in general energy dependent and thus modulate the observed CR spectrum.
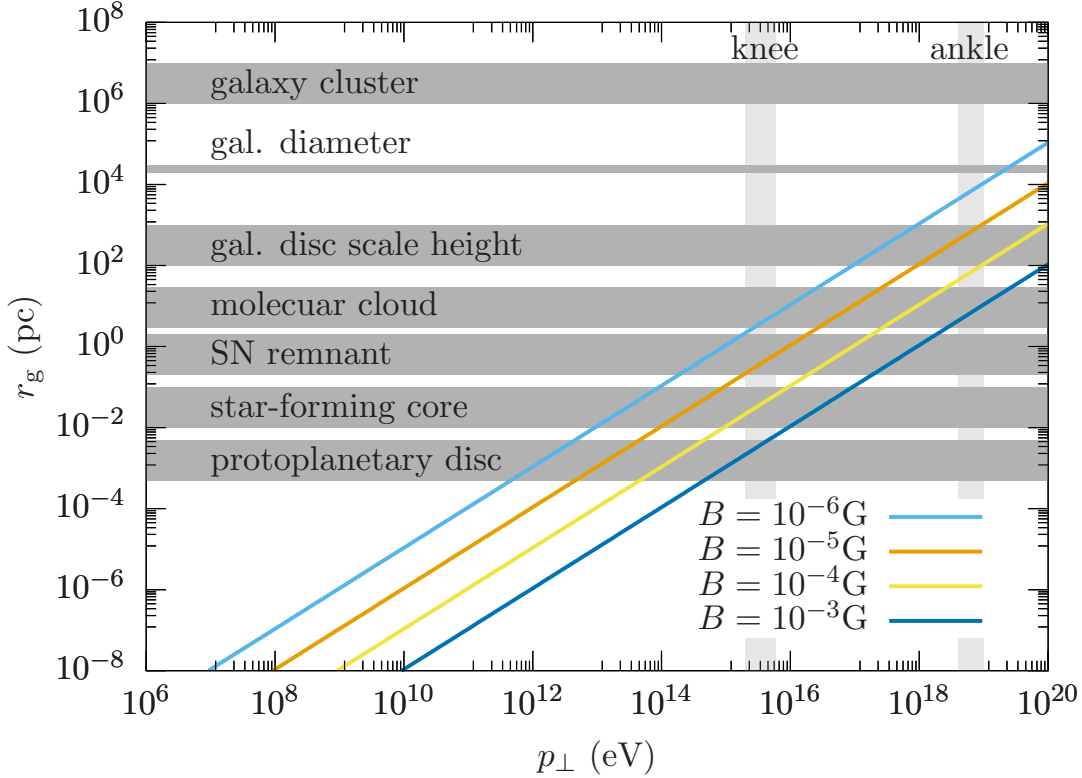

Figure 3.9: Cosmic ray gyro-radius, r_g, vs. momentum perpendicular to the magnetic field, $p_\perp$, for different field strengths. $10^{-6}\,\mathrm{G}$ represents a characteristic order of magnitude for the ISM in our Galaxy. Describing cosmic ray transport via a fluid description is reasonable on length scales sufficiently larger than their gyro-radii. Plot taken from Hanasz et al. (2021).

Whereas the diffusive motion of CRs prohibits to extract any information about the particle's origin from its arrival direction we can still learn a great deal about the time it has traveled, the confinement time and the average amount of matter it must have traversed, the so-called *grammage*, Λ. The latter can be inferred from the relative abundance of secondary CRs (see figure 3.2) when accounting for all possible production channels by collisions of primary CRs with the interstellar gas. There is some uncertainty in the differential cross sections but enough knowledge to provide a decent order of magnitude estimate for the grammage which yields $\Lambda \sim 10\,\mathrm{g/cm^2}$ (e.g., Gaisser et al., 2016; Tatischeff and Gabici, 2018). The grammage is given in units of mass density integrated over the CR path length which depends on the average density along the way. Given the mean ISM density in our galactic disk with $\rho_{disk} \sim m_p/\mathrm{cm^3}$ the corresponding path length is

$$l = \frac{\Lambda}{\rho_{disk}} \sim 2\,\mathrm{Mpc} \tag{3.14}$$

which exceeds even the largest dimension of the disk by more than an order of magnitude and thus provides another hint that CRs propagate diffusively. The path length l corresponds to a time scale

$$\tau_{\text{res}} = l/c \sim 6 \text{ Myr}, \tag{3.15}$$

the residence time, capturing the time CRs reside within the galactic disk.

There is yet another independent source of information to infer a time scale associated with the journey of CRs. The relative abundance of unstable to stable isotopes in cosmic rays can be used as atomic clocks in order to infer the average time the particles have existed before reaching our detector. For that purpose the unstable ^{10}Be isotope with a lifetime $\tau_{1/2} \sim 1 \text{ Myr}$ is well suited because beryllium is nearly exclusively produced by collision of heavier nuclei with interstellar gas and therefore the inferred time scale represents the propagation time through the ISM. Connell (1998) employ a leaky box model to the data collected by the Ulysses High Energy Telescope and derive a cosmic ray confinement time

$$\tau_{\text{esc}} \sim 26 \text{ Myr}. \tag{3.16}$$

This value refers to cosmic rays with a kinetic energy per nucleon $\sim 0.5 \text{ GeV}$ and a mean gas density inside the "leaky box" $n_{\text{box}} = 0.19 \text{ atoms/cm}^3$ which was inferred from simultaneously fitting the transport model to observed secondary-to-primary ratios and grammage $\Lambda \approx 7 \text{ g cm}^{-2}$.

The average density n_{box} is lower than the average density in the galactic disk with about one atom per cm^3. This discrepancy and $\tau_{\text{esc}} > \tau_{\text{res}}$ can be reconciled if the cosmic rays spend a significant time in more dilute environments like the hot ISM ($n_{\text{hot}} \sim 0.0065 \text{ cm}^{-3}$ (Ferrière, 2001), which fills most of the volume above and below the disk. This scenario is commonly described as cosmic ray *confinement in a magnetized halo*. Accurately describing CR transport becomes even more complex when accounting for the different phases of the ISM and cosmic ray streaming instabilities in order to determine the respective diffusion coefficient (e.g., Xu and Lazarian, 2022a).

$$H^2 \sim D\tau_{\text{esc}} \tag{3.17}$$

with scale height H (vertical extension from the disk) of the halo and diffusion coefficient D. Evoli et al. (2020) apply a cosmic ray propagation model to recent AMS measurements and conclude $H \gtrsim 5 \text{ kpc}$.

In general the confinement time $\tau_{\text{esc}}(R) \sim H^2/D(R)$, or equivalently speaking the diffusion coefficient $D(R)$, depends on the particle's rigidity. It is of particular interest because the energy dependence of the diffusion provides the link between injection spectrum $\mathcal{N}_{\text{inj}}$ and the observed spectrum here at Earth $\mathcal{N}_{\text{obs}}$ via[5]

$$\mathcal{N}_{\text{obs}} \propto \mathcal{N}_{\text{inj}}\tau_{\text{esc}} \propto \mathcal{N}_{\text{inj}}D^{-1}(R). \tag{3.18}$$

when neglecting possible further modifications due to other energy dependent CR transport processes like reacceleration for example. The energy dependence of the diffusion coefficient can be inferred from the flux ratio of secondary to primary CRs. Aguilar et al. (2016) present the AMS-02 data[6] shown in figure 3.3 and determine

---

[5]Here we use the following notation for the differential number density $\mathcal{N}(E) = \text{d}N/\text{d}E$.

[6]Here we explicitly distinguish AMS-02 data release from the older AMS-01 data. In the following we simply write AMS and usually consider AMS-02 data.

the rigidity dependence of the diffusion coefficient as $\Phi(\text{B/C}) \propto D^{-1}(R) \propto R^{-0.33}$ by a single power law fit in the rigidity range $65\,\text{GV} \leq R \leq 2.6\,\text{TV}$. Plugging this result into (3.18) and using $\mathcal{N}_{\text{obs}} \propto R^{-2.8}$ for the proton spectrum in the hundred GV range Aguilar et al. (2015) yields

$$\mathcal{N}_{\text{inj}} \propto R^{-2.47} \tag{3.19}$$

which is significantly steeper than the DSA prediction $\gamma = 2$ discussed in the previous section.

Remarkably the power law of the diffusion coefficient can be connected to the power spectrum of the external turbulence of the ISM which is also characterized by a power law (see section 4). In a leaky box model with CRs as test particles in a fluctuating magnetic field with $\delta B^2 / B^2 \ll 1$ quasi linear theory allows to connect the wave number dependence of the spectral energy density E_k of turbulence to the diffusion coefficient (see Schlickeiser (2002) for a more detailed treatment)

$$E_k \propto k^{-s} \rightarrow D(R) \propto R^{2-s}. \tag{3.20}$$

The spectral energy density E_k is a characteristic quantity for different types of turbulence. For Kraichnan turbulence $E_k \propto k^{-3/2}$ and hence $D(R) \propto R^{1/2}$ whereas for Kolmogorov turbulence $E_k \propto k^{-5/3}$ and hence $D(R) \propto R^{1/3}$ which agrees perfectly with the results obtained by Aguilar et al. (2016) and also the interstellar turbulence spectrum obtained by Armstrong et al. (1995) and subsequent studies discussed in section 4. Although this argument sounds quite conclusive it has tossed over an important subtlety, namely the relation between the hydrodynamic turbulence power spectrum, associated with the electron density fluctuations considered by Armstrong et al. (1995), and the magneto-hydrodynamic turbulence power spectrum which is relevant for the scattering of CRs.

In summary the presented standard paradigm of CRs provides potential mechanisms that may collectively account for the observed power law energy spectra. Recent observational data allows to rule out one or the other model but there is still an ongoing debate about the dominant physical mechanisms responsible for the observed spectra (Gabici et al., 2019).[7] In the following we employ a model that has yet deserved little attention from the field of CR research and may therefore provide some new insights by using an approach grounded in statistical physics.

3.3 Superstatistical interpretation of CR energy spectra

In our published paper Smolla et al. (2020) we use superstatistics to analyse the flux of primary (He, C, O) and secondary nuclei (Li, Be, B) detected with rigidity (momentum per charge) between $2\,\text{GV}$ and $3\,\text{TV}$ by the Alpha Magnetic Spectrometer (AMS) on the International Space Station that was published in Aguilar et al. (2017, 2018). We show that q-exponential distribution functions, as motivated by generalized versions of statistical mechanics with temperature fluctuations, provide

---

[7]Here we have not provided a complete review about all potential mechanisms. In particular energy losses due to radiation and particle collisions certainly modify the observed spectrum. Reacceleration, adiabatic deceleration and convection may also be important in particular for $p \lesssim 10$ GeV range where diffusion is weaker (Schlickeiser, 2002).

excellent fits for the measured flux of all nuclei considered. Primary and secondary fluxes reveal a universal dependence on kinetic energy per nucleon[8] for which the underlying energy distribution functions are solely distinguished by their effective degrees of freedom. All given spectra are characterized by a universal mean temperature parameter $T \sim 200\,\text{MeV}$ which agrees with the Hagedorn temperature. Our analysis suggests that quantum chromodynamics (QCD) scattering processes together with nonequilibrium temperature fluctuations provide a plausible explanation for the observed universality in cosmic ray energy spectra. Our analysis suggests that QCD scattering processes together with nonequilibrium temperature fluctuations imprint universally onto the measured cosmic ray spectra, and produce a similar shape of energy spectra as high energy collider experiments on the Earth.

3.3.1   Methodology

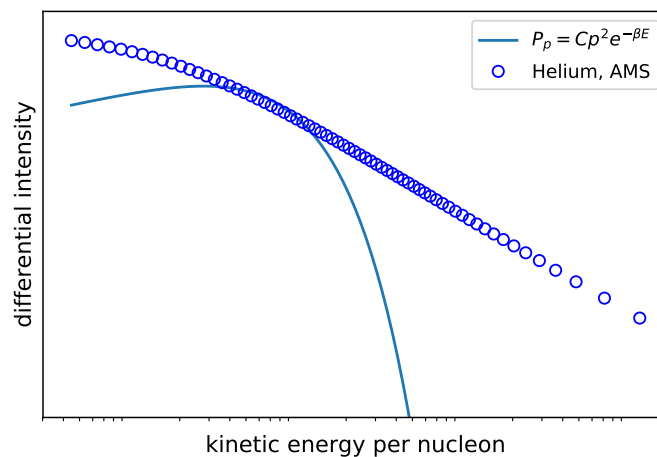**Reasons to go beyond equilibrium thermodynamics**

Figure 3.10: Evidently the flux of Helium nuclei, detected by AMS and presented by Aguilar et al. (2017) as differential intensity in the GeV to TeV range, does not decay exponentially for larger energies but the straight line in this log-log plot illustrates its asymptotic power law behavior. The blue solid curve shows the attempt to fit the data with a Maxwell-Boltzmann distribution $P_p = Cp^2 e^{-\beta E}$.

From equilibrium thermodynamics we know that the momentum distribution of an ideal gas at constant temperature $T = \beta^{-1}$ ($k_B = 1$ convention with temperature in energy units $[T] = \text{eV}$) is described by the Maxwell Boltzmann distribution in momentum space $P_p = C(\beta)p^2 e^{-\beta E(p)}$ with a temperature dependent normalization constant $C(\beta)$. Given the momentum or energy distribution of CRs we can naively try to find a best fit for the Maxwell Boltzmann distribution with β as free parameter. Fig. 3.10 illustrates that the flux of Helium detected by AMS in the GeV

---

[8]Commonly rigidity (momentum per charge) is chosen rather than kinetic energy or momentum because it is particles with equal rigidity which experience the same acceleration and diffusion. Also the AMS data is presented as differential intensity in rigidity. For highly relativistic particles the spectrum is the same in momentum, energy or rigidity units whereas the shape differs for nuclei in the GeV range or below.

to TeV range does not decay exponentially for larger energies, which is characteristic for a Maxwell Boltzmann distribution, but as a power law over multiple orders of magnitudes. This heuristic argument suggests that nonequilibrium statistical physics might be a more suitable description which is the scope of generalized statistical mechanics. Therefore, superstatistics provides a framework which naturally generates power laws rather than exponential distributions as the relevant effective canonical distributions. But before applying the superstatistical model to the AMS data we review some important subtleties about different ways for counting particles and investigating the CR spectra.

Differential intensity and energy variables

The AMS data in Aguilar et al. (2017, 2018) was presented in bins of rigidity $R = pc/Ze$ with atomic number Z, electric charge e, momentum $p = |\boldsymbol{p}|$, $[R] = [\mathrm{V}]$ and the corresponding flux measured in units $[J(R)] = [\mathrm{m}^{-2}\mathrm{sr}^{-1}\mathrm{s}^{-1}\mathrm{GV}^{-1}]$. Instead of rigidity we have chosen to investigate the spectrum with respect to kinetic energy per nucleon, defined as

$$E = \frac{E_{total} - m}{A} \tag{3.21}$$

with total energy $E_{\text{total}} = \sqrt{p^2 + m^2}$, momentum $p = |\boldsymbol{p}|$, rest mass $m = Au$, mass number A, atomic mass unit $u = 0.931\,\mathrm{GeV}$ and $[m] = [p] = [\mathrm{GeV}]$ in $c = 1$ convention. To convert the flux dependence from rigidity R to kinetic energy per nucleon E, we need to transform the flux $J_R(R) \to J_E(E)$ such that $J_R(R)\mathrm{d}R = J_E(E)\mathrm{d}E$ is conserved. This is a simple transformation of variables and yields

$$J_E(E) = \frac{A}{Ze} \frac{E + u}{\sqrt{E(E + 2u)}} J_R(R), \tag{3.22}$$

with $[J_E(E)] = [\mathrm{m}^{-2}\mathrm{sr}^{-1}\mathrm{s}^{-1}\mathrm{GeV}^{-1}]$. For better visibility of the accuracy of our fits, we multiplied the flux with $E^{2.7}$, such that the units for the flux in the presented plots are $[\mathrm{GeV}^{1.7}\mathrm{m}^{-2}\mathrm{sr}^{-1}\mathrm{s}^{-1}]$. For the atomic number A we refer to the AMS collaboration (Aguilar et al., 2017, 2018) who inferred the following average abundance of isotopes ^{4}He, ^{12}C, ^{16}O, $^{6.5}$Li, ^{8}Be and $^{10.7}$Be among the detected nuclei. The measured flux J represents a differential intensity. Thus it counts the number of particles with energy E (or rigidity R) coming from a unit solid angle that pass through a unit surface per unit of time. Therefore, in order to apply superstatistics we need to connect distribution functions with differential intensities.

Fitting distribution functions to differential intensities

The distribution function of our superstatistical model is given by (2.97), for which we still need to specify the energy momentum relation in order to calculate the phase space factor $\rho(E)$. Since we consider kinetic energy per nucleon, defined in equation (3.21), which depends only on the magnitude of the momentum we have $\mathrm{d}^3p = 4\pi p^2 \mathrm{d}p$ which implies $\rho(p) \sim p^2$. Hence, the density of states $\rho(E)$ can be calculated from the conservation condition $P_p \mathrm{d}p = P_E \mathrm{d}E$ which yields

$$P_E(E) = C\rho(E)e_q^{-bE} = C\rho(p)\frac{\mathrm{d}p}{\mathrm{d}E}e_q^{-bE}. \tag{3.23}$$

Calculating the derivative $\mathrm{d}p/\mathrm{d}E$ and using $\rho(p) = p^2 = A^2 E(E + 2u)$ we find

$$\rho(E) \sim (E + u)\sqrt{E(E + 2u)}, \qquad (3.24)$$

where we have again neglected constant global factors in our equations because we are focusing on the shape of the spectrum rather than its absolute magnitude. Thus for our superstatistical model the distribution function with respect to kinetic energy per nucleon is given by

$$P_E = C(E + u)\sqrt{E(E + 2u)}e_q^{-bE}. \qquad (3.25)$$

Evidently, $[P_E] = [\mathrm{eV}^{-1}\,\mathrm{m}^{-3}]$ does not have the same dimension as the detected flux, that is given as differential intensity J with $[J] = [\mathrm{eV}^{-1}\,\mathrm{m}^{-2}\,\mathrm{s}^{-1}\,\mathrm{sr}^{-1}]$. This reminds us that in order to associate a distribution function with a measured differential intensity we have to account for the rate at which particles go through the detector. Therefore, we multiply with the particle's velocity to obtain the flux, J_E, corresponding to the distribution function, P_E, which yields

$$J_E^{\mathrm{mod}}(E) = Cv(E)P_E(E) = Cv(E)\rho(E)e_q^{-bE}. \qquad (3.26)$$

Apparently $J_E^{\mathrm{mod}}(E)$ has the the desired physical dimensions because $[vP_E] = [\mathrm{eV}\,\mathrm{m}^{-2}\,\mathrm{s}^{-1}]$ and the units sr^{-1} for the solid angle are merely a dimensionless global factor. In order to express the velocity in terms of E we use $p = \gamma m v$ with $\gamma = \frac{1}{\sqrt{1-v^2}}$ (in $c = 1$ convention), $p = A\sqrt{E(E + 2u)}$ and $m = Au$ to find

$$v(E) = \frac{\sqrt{E(E + 2u)}}{(E + u)}. \qquad (3.27)$$

Plugging everything into equation (3.26) yields

$$J_E^{\mathrm{mod}}(E) = CE(E + 2u)e_q^{-bE}, \qquad (3.28)$$

which is the differential intensity of our our model, $J_E^{\mathrm{mod}}(E)$, that was derived from the superstatistical distribution function. Moraal (2013) provides a detailed overview about the different ways to count particles including the relation between differential intensity and momentum space distribution function (3.26) upon exploiting the fact that $E \sim p$ for large momenta such that we finally obtain $v(E)\rho(E) \sim E(E + 2u) \sim p^2$.

This careful analysis is essential for connecting the observed cosmic ray *differential intensities* with the theoretical *distribution functions* from the superstatistical model. In previous studies the fitting of distribution functions to the data was technically incorrect (e.g., Beck, 2004, 2009; Yalcin and Beck, 2018). Hence, the methodology presented here is an important contribution for interpreting any cosmic ray data with theoretical models which are based on superstatistics.

3.3.2   Results and interpretation

We use the AMS data (Aguilar et al., 2017, 2018) to investigate the universal properties of the primary CRs helium, carbon, oxygen, and the secondary CRs beryllium, lithium, boron. Our superstatistical model allows to infer physical parameters from the observed energy spectra by applying (3.28) to the observed differential intensities with $C > 0$, $q > 1$ and $T = b^{-1} > 0$ as fitting parameters.
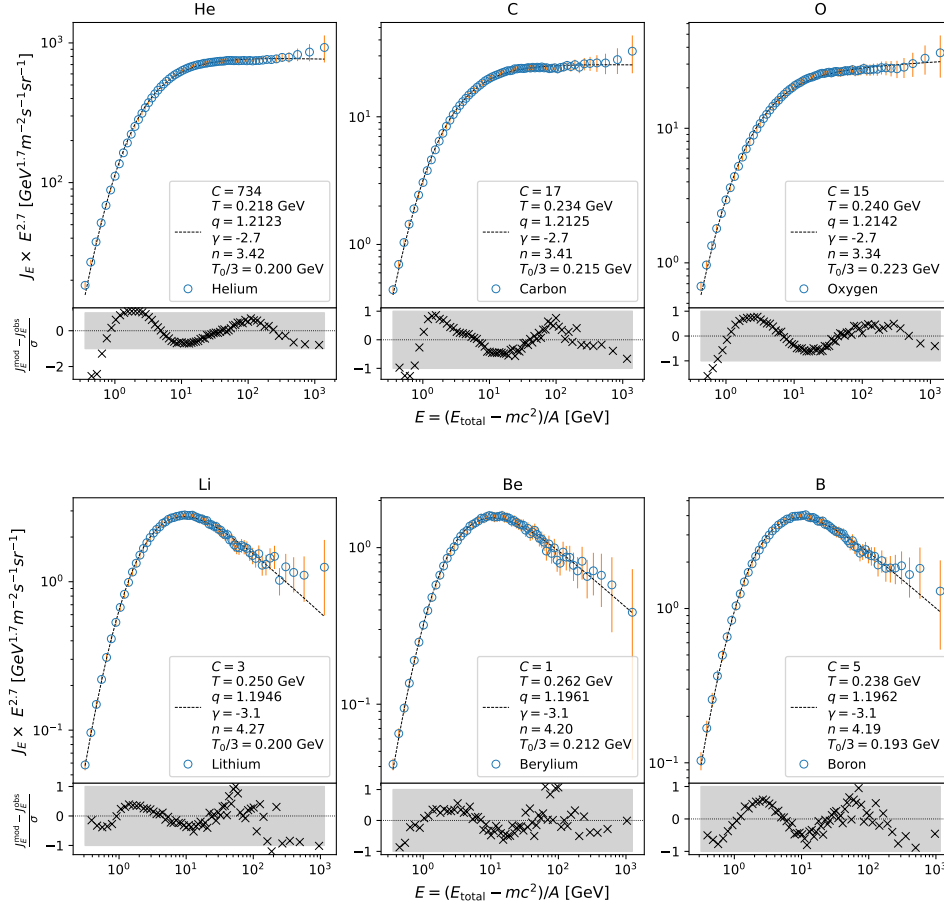
Figure 3.11: The particle flux of each CR species was fitted with equation (3.28) using the three parameters C, T, q. The vertical axis in this log-log plot was multiplied with $E^{2.7}$ for better visibility. The fit's accuracy can be quantified by the deviation from modelled J^{mod} to observed flux J^{obs} weighted by the respective measurement error σ. Evidently, almost all data points fall within the uncertainty range of $\pm\sigma$ illustrated as grey shaded area. The mean temperature T_0 is defined in equation (2.90). The amplitude C has dimensions $[C] = [\mathrm{m}^{-2}\,\mathrm{sr}^{-1}\,\mathrm{s}^{-1}\,\mathrm{GeV}^{-3}]$ which is omitted in the legend of the plot for reasons of better readability.

Fig. 3.11 illustrates that most data points are fitted by our model within a single standard deviation for all six nuclei. We determined the best fit by applying χ^2-minimization with $(J_E^{\mathrm{mod}} - J_E^{\mathrm{obs}})/\sigma$, meaning deviation of model from data weighted by the respective measurement uncertainty, where the standard deviation σ is the sum of measurement uncertainties for a specific energy bin. For most of the data the error is of the order of a few percent whereas the uncertainty tends to increase with energy up to the largest uncertainty of 89 percent associated with the Beryllium flux measured in the highest energy bin.

Since our analysis focuses on the spectral *shape* we collect all constant factors, which do not depend explicitly on the energy, in the amplitude C, which is merely a gauge for the absolute magnitude of the flux.

The entropic index q determines the high-energy (i.e., the tail) behavior of the distribution since the q-exponential asymptotically approaches a power law

$$\lim_{E \to \infty} e_q^{-bE} \propto E^{\gamma}, \tag{3.29}$$

with spectral index

$$\gamma = 2 - \frac{1}{q-1} \tag{3.30}$$

for $q > 1$. The effective degrees of freedom n, defined by equation (2.88), are related to the entropic index q via

$$n = \frac{2}{q-1} - 6. \tag{3.31}$$

The parameter $T = b^{-1}$ represents a temperature in energy units that mainly affects the low-energy turnover around the flux maximum. For the temperature parameter $T_0 = \beta_0^{-1}$, defined in (2.90), we get the value $T_0 \sim 600$ MeV for each of the six CR species, that is atomic nuclei which are built of multiple nucleons - protons and neutrons. Our superstatistical model considers kinetic energy per nucleon and each nucleon consists of three quarks. Dividing the mean temperature by the number of quarks per nucleon yields $T_0/3 \sim 200$ MeV. This temperature or energy scale coincides with the observed value of the Hagedorn temperature which is roughly known to be in the range 140 to 200 MeV (Hagedorn, 1965; Rafelski and Ericson, 2016; Broniowski et al., 2004). It represents a universal critical temperature for the quark gluon plasma and for high energy QCD scattering processes. The best fit value for $T_0/3$ turns out to be the same for all six nuclei, i.e., for both primary and secondary cosmic rays within a range of about one tenth of its absolute value. This interpretation was outlined more broadly in Smolla et al. (2020) and presented earlier for electrons and positrons by Yalcin and Beck (2018).

Figure 3.12 reveals the universal properties of the primary (He, C, O) and secondary (Li, Be, B) cosmic ray fluxes when rescaling each nuclei's flux with a suitable global factor such that all data points collapse to a single line in the low energy range. Fixing the global amplitude parameter to $C = 1$ and $T = 0.240$ GeV, which is the average value for the temperatures inferred from the individual best fits in figure 3.11, allows us to do a best fit with q as the only free parameter for the collapsed data of primaries and secondaries. This yields $q_{\mathrm{prim}} = 1.2109$ ($n = 3.5$) and $q_{\mathrm{sec}} = 1.1969$ ($n = 4.2$). From its definition in (2.88) we require n to be an integer and we can interpret n as effective degrees of freedom of temperature fluctuations. Evidently, the best fit parameters are not integers but this could be explained by secondary effects in the following reasoning. The observed spectra are the outcome of an initial spectra, associated with the energy distribution at the source of acceleration, that becomes modified during propagation due to energy dependent radiative losses, collision and diffusion processes. In the absence of these affects, meaning considering the energy spectra near the source, we would expect to observe $n_{\mathrm{prim}} = 3$ and for the secondaries $n_{\mathrm{sec}} = n_{\mathrm{prim}} + 1$ we could have an extra degree of freedom since they originate from the collision of primaries with secondaries. This speculative interpretation still requires further research in order to clarify the physical meaning of the effective degrees of freedom. Nevertheless, it is an interesting approach which builds on previous results (Tsallis et al., 2004; Beck, 2004, 2009; Yalcin and Beck, 2018).

3.3.3 Discussion

In the following we choose a critical point of view to discuss the results obtained with our superstatistical model. We outline some subtle details in the methodology and
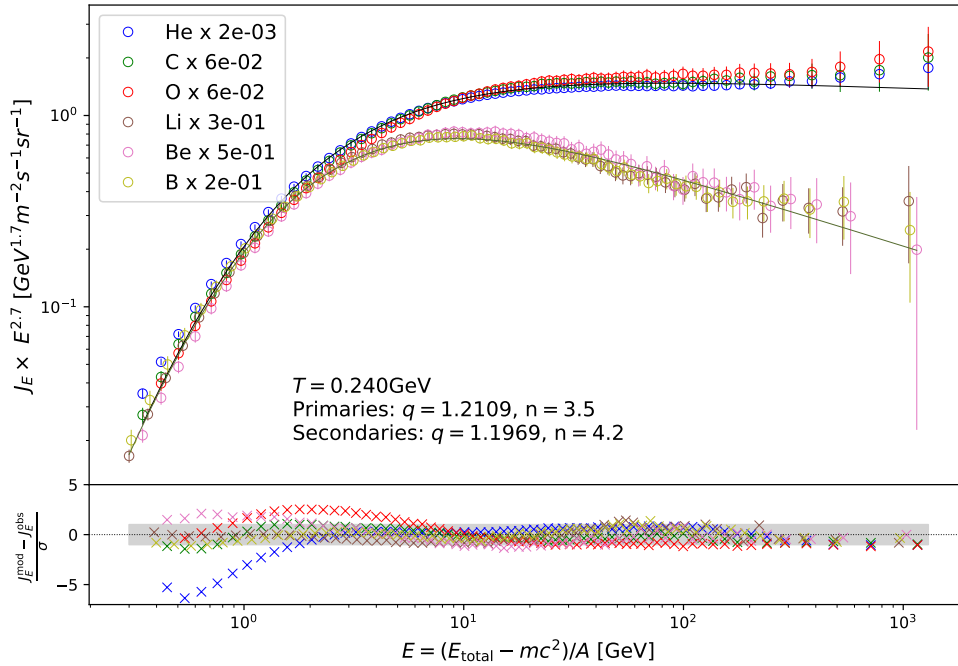
Figure 3.12: Each particle flux was rescaled with a suitable factor such that the data points roughly collapse to a single line at the low energy end and the universal properties of primary and secondary cosmic ray nuclei spectra become visible. For larger energies the spectrum splits into primaries and secondaries which is distinguished by a single parameter, the entropic index q and can be interpreted by the underlying effective degrees of freedom.

comment on the canonical interpretation of the data within the standard paradigm of CRs.

Relevance of solar wind modulation

The AMS measurements were taken on the ISS at about $400\,\mathrm{km}$ above Earth's surface and are thus subject to solar wind modulation which yields a suppressed flux compared to outside the heliosphere, in particular for charged particles with kinetic energies per nucleon $E \lesssim 10\,\mathrm{GeV}$ (Moraal, 2014). Thus for our given AMS data with kinetic energies per nucleon in the range of $0.4\,\mathrm{GeV} \lesssim E \lesssim 1.2\,\mathrm{TeV}$ the flux in the lower energy range should be affected and we aim to quantify this effect of solar wind modulation on our given spectra. Using cosmic ray propagation models allows to infer the unmodulated flux before cosmic rays are entering the heliosphere, that is the local interstellar flux, from the given data.

This was recently done by Boschini et al. (2017, 2018, 2020) who combined the two cosmic ray propagation models HelMod and Galprop and published the calculated flux for all our given atomic nuclei and for the entire energy range covered by AMS. We use their data and interpolate it to match the AMS energy bins definition. We find an upper bound for the deviation of local interstellar flux (LIS) to flux inside heliosphere (AMS) for the lowest energetic particles with $LIS/AMS \lesssim 4$ for $E = 0.4\,\mathrm{GeV}$. The two spectra converge for larger energies and we find $LIS/AMS \lesssim 1.2$ for $E = 10\,\mathrm{GeV}$ such that in fact only the lowest energy
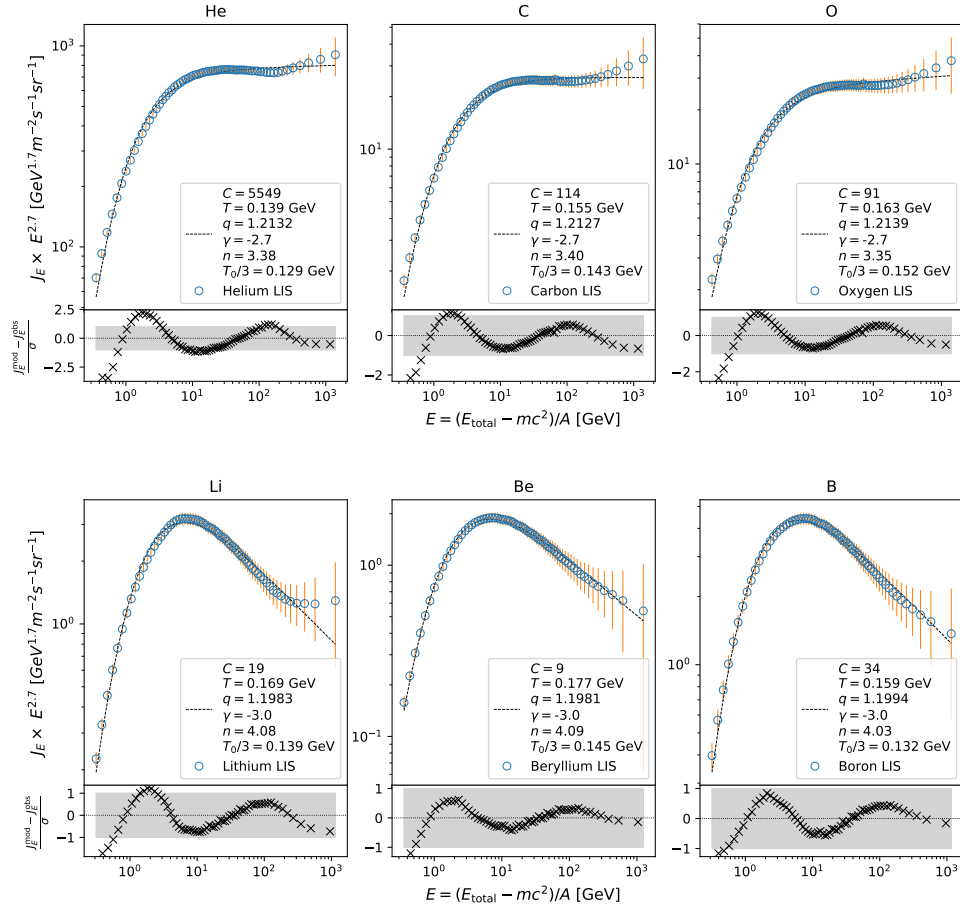
Figure 3.13: Superstatistical results are robust when correcting for heliospheric impact. Using cosmic ray propagation models HelMod and Galprop allows Boschini et al. (2017, 2018, 2020) to estimate the flux outside the heliosphere, that is unmodulated by solar wind representing the local interstellar spectra, in short LIS. Here, we use the data published in Boschini et al. (2017, 2018, 2020) which we investigate for the given AMS energy bins. We apply (3.28), that is $J_E^{\mathrm{mod}}(E) = CE(E + 2u)e_q(-bE)$ with $e_q^x \equiv (1 + (1-q)x)^{\frac{1}{1-q}}$, in order to derive the best fit global amplitude C, temperature T and entropic index q. From the best fit parameter T we derive the average temperature per quark as $T_0/3$. The entropic index q can be translated into effective degrees of freedom n and into the spectral index γ representing the asymptotic power law behaviour $\lim_{E\to\infty} e_q^{-bE} \propto E^\gamma$.

range of our spectra is significantly affected. Since the propagation model provides the flux without giving any uncertainty, we assign each estimated flux the same relative error as in the AMS data set. This makes the comparison between the flux inside and outside the heliosphere consistent and allows to put appropriate weight on measurements with smaller uncertainties for our least-square optimization.

Analogously to the steps performed above for the given AMS data, we apply our superstatistical model to the LIS data and present the resulting fits and parameters in figure 3.13. The average temperatures $T_0/3$ for the different nuclei are about 50 to 80 MeV lower than for the unmodulated AMS data, namely in the range 129 to 152 MeV. Still, these temperatures are all about the scale of the Hagedorn temperature and in fact coincide with the temperature range 130 to 160 MeV inferred by q-exponential distributions applied to some LHC experiments (e.g., Wong et al., 2015; Wilk and Wlodarczyk, 2017). The effective degrees of freedom remain

approximately the same. Since the reliability of our methodology ultimately depends on having a large energy range measured for all the different nuclei, the AMS data is the best currently available experimental data set. In contrast, measurements acquired by Voyager outside the heliosphere only cover energies from about 3 MeV to a few hundred MeV (e.g., Cummings et al., 2016; Stone et al., 2019). Hence, we apply our analysis to the broad range of AMS-measured data and estimate the modulation by the solar wind, rather than using theoretically derived data for unmodulated spectra.

Choice of kinetic energy per nucleon vs. total energy

As an alternative to the canonical statistics considering the total energy *per atom* a quantity frequently considered in cosmic ray literature is kinetic energy *per nucleon*. The choice of total vs. kinetic energy is meaningless for the energy spectrum associated with the Boltzmann factor whereas the weighting *per nucleon* actually yields a different spectrum as illustrated below.

The relativistic generalization for kinetic energy is $E_{\text{kin}} = E_{\text{tot}} - m = \sqrt{p^2 + m^2} - m$ which can be expanded for $p \ll m$ to recover the classical kinetic energy as first order term in $E_{\text{kin}} = \frac{p^2}{2m} + \mathcal{O}(p^4)$. Considering the Boltzmann factor $B(E_{\text{tot}}) = e^{-\beta E_{\text{tot}}}$ the choice of total energy E_{tot} or kinetic energy $(E_{\text{tot}} - m)$ are equivalent up to a temperature dependent global constant since

$$
\begin{aligned}
B(E_{\text{kin}}) &= e^{-\beta(E_{\text{tot}} - m)} \\
&= e^{\beta m} e^{-\beta E_{\text{tot}}} \\
&\propto B(E_{\text{tot}})
\end{aligned}
\tag{3.32}
$$

whereas the choice of kinetic energy per nucleon $E = (E_{\text{tot}} - m)/A$ does not factorize into the canonical Boltzmann factor and a constant because

$$
B(E) = e^{\frac{-\beta(E_{\text{tot}} - m)}{A}} = \left[e^{-\beta(E_{\text{tot}} - m)} \right]^{\frac{1}{A}}.
\tag{3.33}
$$

To summarize, the Boltzmann factors $B(E_{\text{tot}})$ and $B(E_{\text{kin}})$ are generalizations which recover the classical Boltzmann statistics with $B(p^2/2m)$ for $p \ll m$. Whereas $B(E)$, with kinetic energy per nucleon $E = (E_{\text{tot}} - m)/A$, is characterised by a different energy dependence, that is the distribution function actually has a different spectral shape. Superstatistics with kinetic energy *per nucleon* is thus not a generalization of canonical Boltzmann statistics for energy *per atom* and should therefore be investigated more critically in terms of the underlying assumptions and their implications for the statistical model at hand.

Deriving the superstatistical distribution function: normalization constant for relativistic particles

In agreement with Beck (2004) we calculate the normalization (2.91) in the following way

$$
\begin{aligned}
C_p(\beta)^{-1} &= \int_0^{+\infty} e^{-\beta E} E^2 \mathrm{d}E \\
&= 2\beta^{-3}.
\end{aligned}
\tag{3.34}
$$

However, this integral rests on an important assumption, that is $\rho(E) \sim \rho(p)$, meaning the density of states is essentially the same in energy and momentum space, which holds true only for to the ultra-relativistic regime where $E \sim p$. Evidently, this relation holds for both choices of energy, the total energy $E = \sqrt{p^2 + m^2}$ or the kinetic energy per nucleon $E = (\sqrt{p^2 + m^2} - m)/A$, only for $p \gg m$. One could argue that $\lim_{m \to 0} \rho(E) = E^2$ but $m \to 0$ for massive particles actually means $p \gg m$ which is only true for sufficiently large temperatures meaning $p \sim \beta^{-1} \gg m$ which will be violated when integrating over $\int_0^\infty \mathrm{d}\beta$ in (2.87). Additionally, the required temperatures exceed even the temperature of the hot ionized medium $T \sim 10^6 \, \mathrm{K} \sim 100 \, \mathrm{eV} \sim 10^{-7} m_p$ (with proton mass m_p) by multiple orders of magnitude.

A more rigorous derivation for a relativistic superstatistical distribution function could be obtained by using the relativistic normalization constant which is found in the Maxwell Jüttner distribution (2.80) and can be expressed more compactly via equation (2.82). Hence, in order to find the relativistic distribution function (2.87) for χ^2-superstatistics the following integral has to be solved

$$P_{E_{\text{tot}}}(E_{\text{tot}}) \sim \int_0^\infty \frac{\beta^{\frac{n}{2}} e^{-\beta(E_{\text{tot}} + \frac{n}{2\beta_0})}}{K_2(\beta m)} \mathrm{d}\beta. \tag{3.35}$$

Here K_2 represents the modified Bessel function of the second kind. To our best knowledge this integral has not yet been solved analytically but could be investigated (e.g. with numerical methods) in future work.

Interpretation of AMS data within standard paradigm of CRs

Whereas we decided to investigate the CR spectra in kinetic energy per nucleon the AMS collaboration focused on rigidity. There are at least two arguments why AMS uses rigidity. First, the given magnetic spectrometer actually measures the particle's rigidity. Second, in the standard paradigm of CRs (section 3.2) diffusive shock acceleration and diffusive transport accelerate particles according to their rigidity (Kachelriess and Semikoz, 2019).
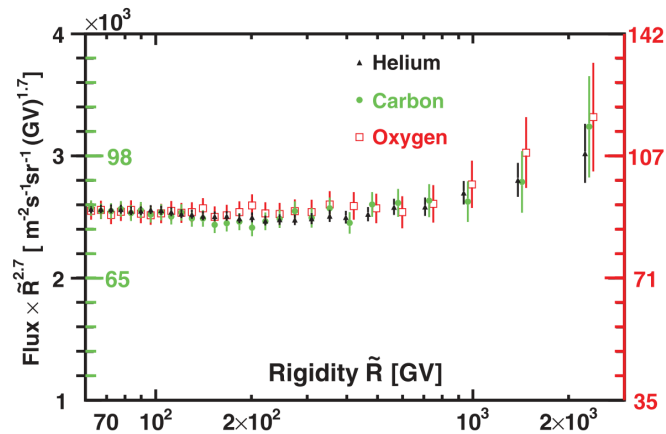

Figure 3.14: The flux of primary CRs helium, carbon and oxygen shares an identical rigidity dependence for $R > 60 \, \mathrm{GV}$. Plot by Aguilar et al. (2017).

Figure 3.14 illustrates the identical rigidity dependence of primary CRs helium, carbon and oxygen for $R > 60 \, \mathrm{GV}$. This property can be understood within the

standard paradigm of CRs if the different nuclei are all accelerated at the same kind of sources (in a statistical sense) according to their rigidity and thus share an identical injection spectrum. Assuming their propagation properties to depend only on rigidity and not on the type of particle (e.g., number of nucleons), and in the absence of further effects like energy dependent losses, we expect an identical rigidity dependence for all primaries. The particle dependent spectra for $R < 60\,\mathrm{GV}$ could result from collisions of primaries with other interstellar particles. The effective production cross sections during such collisions depend on the type of particle and generally tend to increase with the number of charges per nuclei (Aguilar et al., 2021b).[9]
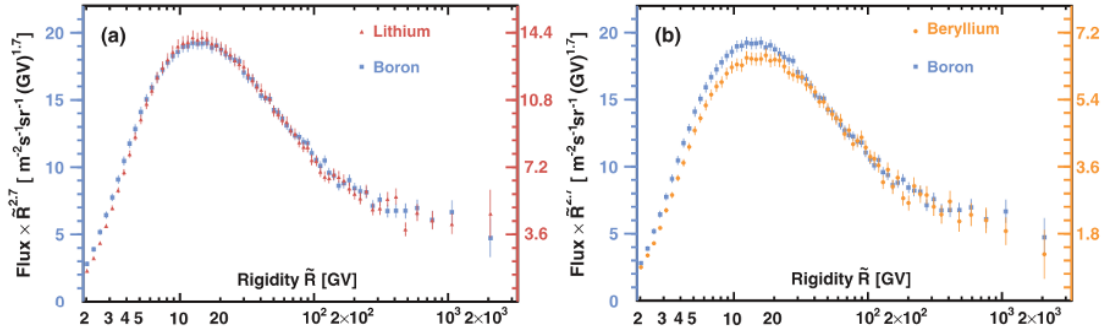

Figure 3.15: The spectra for the secondary CRs lithium, beryllium and boron all share an identical rigidity dependence for $R > 30\,\mathrm{GV}$ whereas lithium and boron already share this property for $R > 7\,\mathrm{GV}$. Plot by Aguilar et al. (2018).

Figure 3.15 presents the flux of the secondary CRs lithium, beryllium and boron with identical rigidity dependence for $R > 30\,\mathrm{GV}$ whereas lithium and boron already share this property for $R > 7\,\mathrm{GV}$. The reduced flux of beryllium could result from the decay of the radioactive ^{10}Be isotope. For higher momenta (and thus higher rigidities) this effect is diminished because of the reduced half life due to time dilation in the particle's frame of reference that is Lorentz-boosted compared to the observer's frame.

Figure 3.16 compares the rigidity dependent flux of primaries to secondaries. Clearly we recover the two universality classes which are also observed for the spectra in kinetic energy per nucleon in figure 3.12. The right plot presents the spectral index $\gamma = \mathrm{d}[\log(\mathrm{Flux})]/\mathrm{d}[\log(R)]$ determined over rigidity intervals bounded by 7.09, 12.0, 16.6., 22.8, 41.9, 60.3., 192, and 3300 GV. Apparently the spectra of primary and secondary nuclei all harden (become flatter) for $R \gtrsim 200\,\mathrm{GV}$ but this effect is even more pronounced for the secondaries. Analogously to the reasoning for determining the diffusion coefficient from the primary to secondary flux ratio (see figure 3.3) this spectral break may well be associated with CR transport and because it imprints even stronger on the secondary spectra. Blasi (2019b) proposes an explanation arguing that the spectral break could be due to a transition from CRs scattering on self-generated Alfvén waves to CRs scattering on pre-existing MHD waves. The energy range of this transition can be estimated by comparing the rate of nonlinear Landau damping to the growth rate of the resonant streaming instability which is responsible for the generation of self-generated Alfvén waves. Remarkably the transition is expected at about the observed scale of $\sim 200\,\mathrm{GV}$ but its applicability

---

[9]In general the effective production sections also depend on the kinetic energy per nucleon but turn out to be approximately constant above a few GeV/nucleon (Génolini et al., 2018).
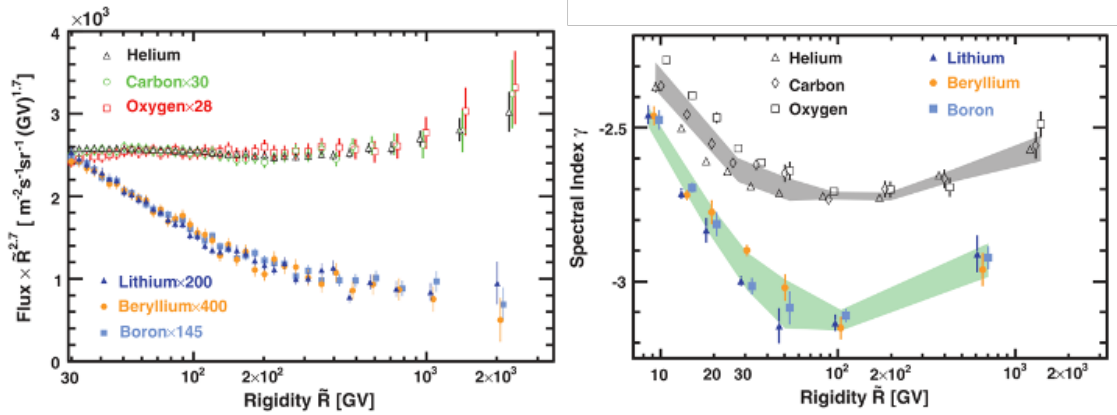
Figure 3.16: The left plot clearly shows that He, C, O and Li, Be, B respectively share the same rigidity dependence that clearly separates the primaries from the secondaries. The right plot illustrates the spectral break at ~ 200 GV for both primaries and secondaries whereas for the latter the hardening is even more pronounced. Plots by Aguilar et al. (2018).

is constrained to environments with fully ionized gas because even a small fraction of neutral gas could fully damp the CR-generated Alfvén waves (Amato and Blasi, 2018). Ultimately the spectral break needs to be explained self-consistently together with all the other recent anomalies (see review by Gabici et al., 2019) for which various models are currently under debate (see review by Kachelriess and Semikoz, 2019).

3.3.4 Comparison with new data for other heavy CR nuclei

After the publication of Smolla et al. (2020) the AMS collaboration released data for the primaries neon, magnesium, silicon (Aguilar et al., 2020), iron (Aguilar et al., 2021b), and the secondary fluorine (Aguilar et al., 2021a). Figure 3.17 shows the results obtained with our superstatistical model for the new data and additionally for protons (Aguilar et al., 2015). The accuracy of the fits is quite good and generally comparable to the previous results presented in figure 3.11. Comparing the best fit parameters obtained for all particle types (new and old data), namely the degrees of freedom n and the temperature $T_0/3$, provides the following insights. First, with $n \sim 3.16 - 3.45$, primary CRs are clearly characterized by lower degrees of freedom compared to the secondary CRs with $n \sim 3.96 - 4.27$. Second, the temperature ranges from $\sim 193 - 266$ MeV without a clear correlation with respect to primary vs. secondary. Third, protons clearly differ from primary and secondary CRs in terms of temperature and degrees of freedom. We conclude that the simple picture we propose above and in Smolla et al. (2020), namely a universal temperature scale $T_0/3 \sim 200$ MeV and the distinction of two universality classes by the effective degrees of freedom, has become less sharp with the new data but it is not excluded.

In analogy to the universality plot in figure 3.12 we aim to illustrate the (approximate) universality of primary and secondary CRs by rescaling each flux with a suitable constant such that the data collapse in figure 3.18. On the low energy end $E < 10$ GeV the two primaries helium and iron deviate strongly from the model but for larger energies the fits work very well. Apparently the new data still fits approximately into the previously proposed interpretation of a single universality class for primaries and secondaries respectively.
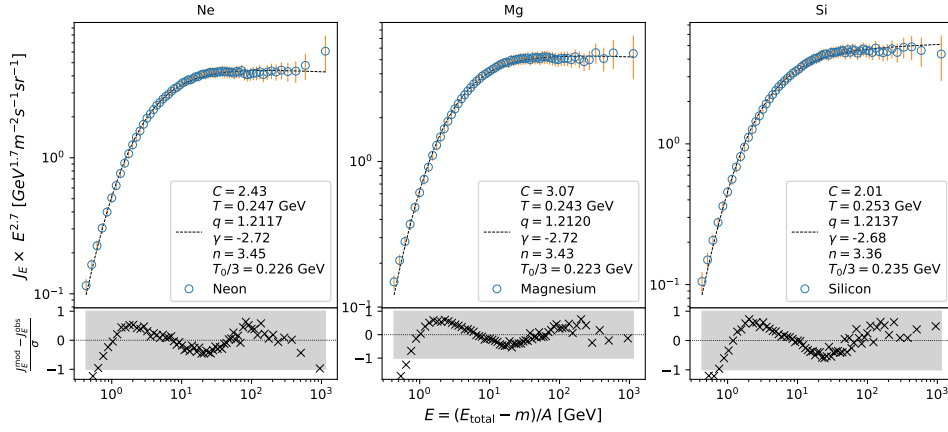
(a) Neon, magnesium, silicon (all primary CRs).
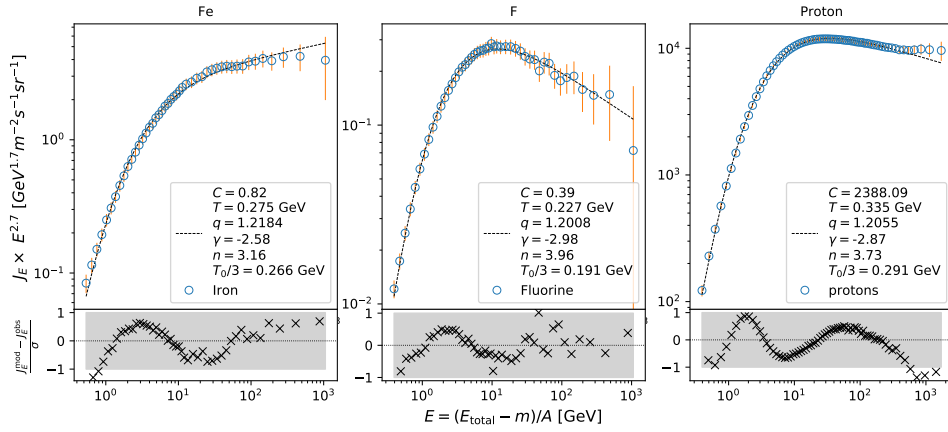
(b) Iron (primary), fluorine (secondary) and protons (for comparison).
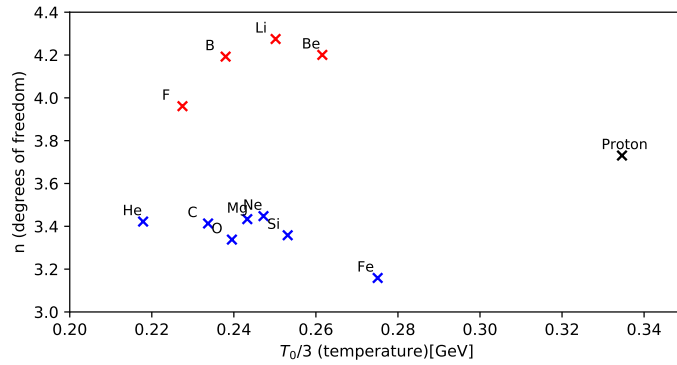
(c) Temperature vs. degrees of freedom.

Figure 3.17: Results of our superstatistical model applied to the newest AMS data fitted with equation (3.28) using three parameters, namely the amplitude C, temperature T, entropic index q. From T we calculate the mean temperature T_0 (see equation (2.90)) and from q we obtain the effective degrees of freedom n (see equation (3.31)). The fit's accuracy can be quantified by the deviation from modelled J^{mod} to observed flux J^{obs} weighted by the respective measurement error σ. The bottom figure illustrates the effective degrees of freedom are lower for the primary CRs (blue) than for the secondary CRs (red).

On the other hand, according to the AMS collaboration the new data reveals two (rigidity dependent) universality classes of primary and secondary CRs respectively

Figure 3.18: The (approximately) universal spectra of primary (He, C, O, Fe, Ne, Mg, Si) and secondary (Li, Be, B, F) cosmic rays can be illustrated by multiplying each flux with a constant factor such that the data collapse nearl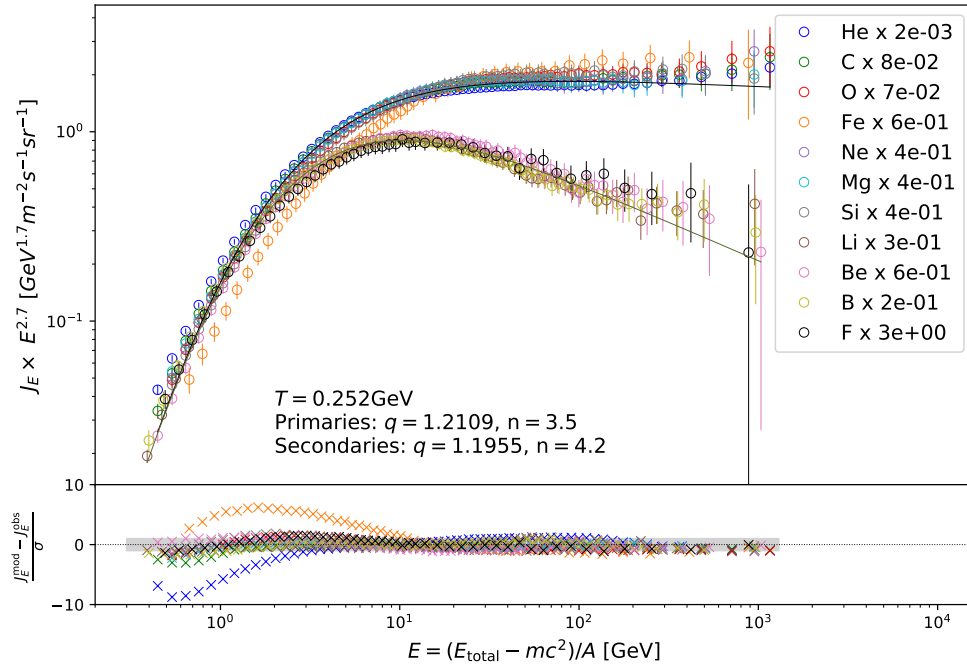y to single curve. We set $T = 252\,\mathrm{GeV}$, which is the arithmetic mean temperature of the individual best fit parameters in 3.17, and determined the best fit for the entropic index q from which the degrees of freedom follow directly via (3.31).

as illustrated in figure 3.19. They classify the rigidity spectra in Aguilar et al. (2020) for the heavier nuclei ^{20}Ne, ^{24}Mg, ^{28}Si as distinct universality class to the lighter nuclei ^{4}He, ^{12}C, ^{16}O but surprisingly ^{56}Fe belongs to the latter class although it is the heaviest nuclei. Apparently the atomic number A does not distinctly characterize the two universality classes and the interpretation is yet unclear. On the other hand the heavy secondary ^{19}F deviates from the rigidity dependence of the lighter secondaries $^{6.5}$Li, ^{8}B and $^{10.7}$Be.[10]

Further evidence for new features in heavier nuclei can be found by considering the secondary to primary flux ratios in figure 3.20. If CR propagation properties are fully determined by the particle's rigidity we would expect a constant ratio of heavy F/Si to the light B/C but the data discovers a mildly decreasing ratio for low rigidities and an increasing ratio for higher rigidites. Another peculiar feature is the increasing Fe/O ratio up to $R \sim 100\,\mathrm{GV}$ which is in tension with the standard models of CR propagation and also with other low energy measurements (e.g., Schroer et al., 2021).

In summary the new data can be interpreted with our superstatistical model self-consistently with the previously discovered universality classes for primaries and secondaries respectively. Nevertheless, our proposed model appears to be rather insensitive to the newly discovered peculiar features discussed above. Further work

---

[10]Aguilar et al. (2018) determined these mass numbers as an effective mean value from the relative abundance of different isotopes in the detected flux.
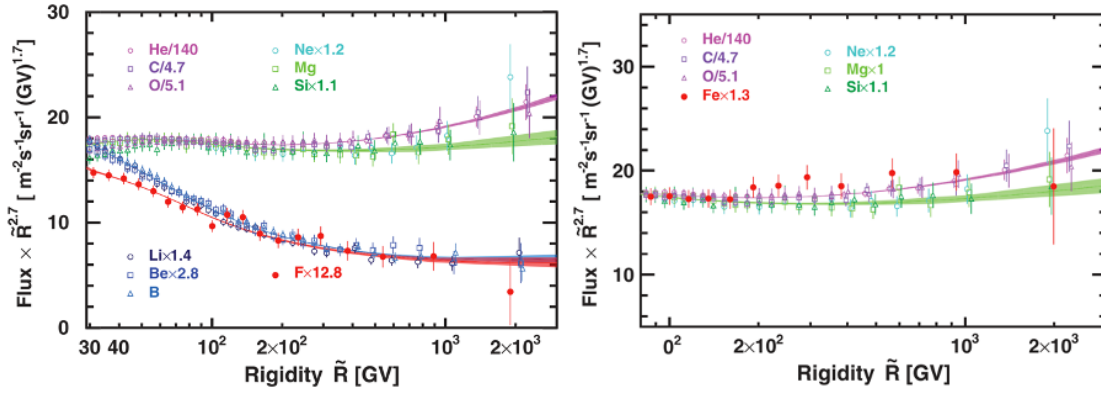
Figure 3.19: The AMS collaboration reported two universality classes for the rigidity spectra of primaries and secondaries respectively. The left plot reveals a different rigidity dependence of the heavy secondary F compared to the lighter secondaries Li, Be, B. Similarly, the heavier primaries Ne, Mg, Si deviate from the lighter primaries He, C, O. Interestingly the right plot shows that the heavy primary Fe looks more similar to the lighter than to the heavier primaries. Left plot by Aguilar et al. (2021a) and right plot by Aguilar et al. (2021b).
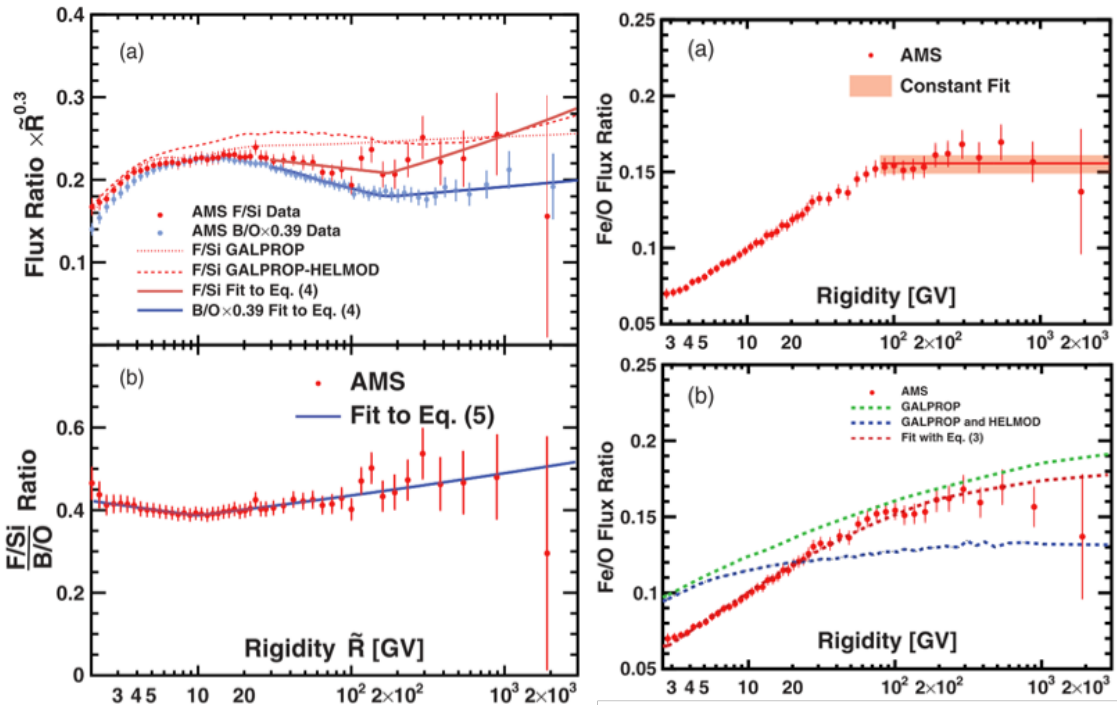
Figure 3.20: On the left the heavy secondary to primary ratio F/Si is compared to the usual primary to secondary ratio B/C and its rigidity dependent features suggest different propagation properties of heavy compared to lighter nuclei. On the right we see that the flux of the heaviest observed nuclei compared to oxygen increases for the low rigidity end until it becomes approximately constant. This peculiar behaviour deviates from the predictions of CR propagation models (lower right) before the new AMS data was published. Left plot by Aguilar et al. (2021a) and right plot by Aguilar et al. (2021b).

is needed to decide whether it is a weakness of our model to not detect the further two universality classes or if the spectra of primary and secondary CRs are in fact universal - at least within a certain energy range.

Chapter 4

Interstellar Turbulence

An understanding of turbulence will eventually necessitate a realization of the integration and vanishing of such dualities as parts and the whole, determinism and randomness, and, especially, order and chaos. (Scalo, 1987)

4.1 Observations

A closer look into interstellar space reveals a great diversity of structures. The interstellar medium (ISM) consists mainly of cold (~ 10 to $100\,\mathrm{K}$), warm ($\sim 10^4\,\mathrm{K}$) and hot ($\sim 10^6\,\mathrm{K}$) gas reservoirs, a small fraction of dust, cosmic rays, electromagnetic radiation and magnetic fields (e.g., Ferrière, 2001). Although the ISM contributes only a smaller fraction to the total mass of our galaxy it is of utmost importance for most processes leading to the formation of structures and therefore for the evolution of the entire galaxy. Examples range from spiral structure at tens of kiloparsec scales, molecular gas clouds at parsec scales to dust particle formation at micrometer scales. Describing the ISM necessarily involves a broad range of scales and a variety of interactions between its components making it a truly complex system. In the following we focus on turbulent motions of the gas components of the ISM and how these can be traced via their effect on electromagnetic radiation. A reasonably complete picture can be obtained because most of the ISM is ionized. Even for environments with a significant fraction of neutral atoms, there is usually still a sufficient degree of ionization such that the neutrals are tightly coupled to the ions with a collision time of $\sim 10^2 - 10^3$ years for the cold neutral medium and $\sim 10^2 - 10^4$ years for the warm neutral medium (Ferrière, 2019).

Figure 4.1 shows the polarization gradient $|\nabla P|$ derived from radio data which reveals a complex web of filamentary structures that look similar to the results obtained in simulations of magnetized turbulence with low Mach numbers (Gaensler et al., 2011). This is not the only hint on the presence of turbulent motions in the ISM but further evidence can be obtained from various observational techniques (see review by Elmegreen and Scalo, 2004).

Figure 4.2 shows the *Big Power Law in the Sky* obtained for the power spectrum of electron density fluctuations in the ISM. The spectrum is inferred by closely investigating radio data for fluctuations in intensity and phase which are caused by the scattering of photons with the free electrons. This so-called *interstellar scintillation* was exploited by Armstrong et al. (1981, 1995) in order to derive the electron density power spectrum for a range of wavenumbers from $k \sim 10^{-13}$ to $10^{-6}\mathrm{m}^{-1}$. The authors used data and methods which are less certain to constrain
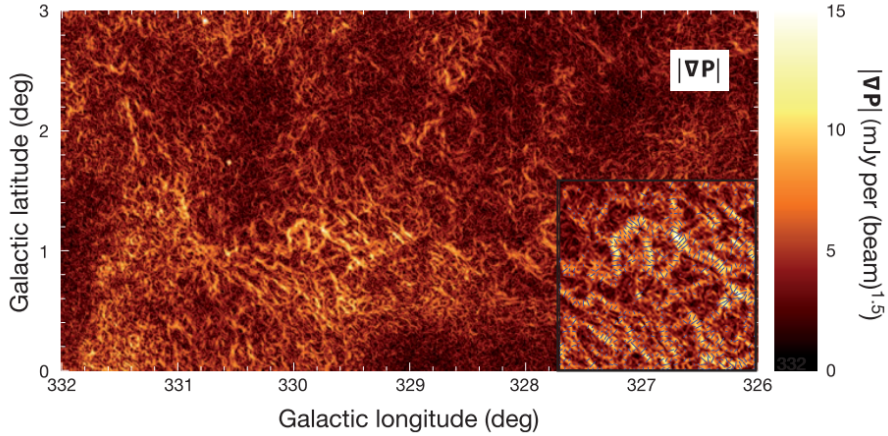
Figure 4.1: The radio polarization gradient $|\nabla P|$ carries information about the properties of the turbulent, diffuse and ionized gas in the ISM. It reveals a complex web of structures with maximal gradients perpendicular (lines in inset) to the filaments (elongated shapes). Image shows an 18-deg^2 region of the Southern Galactic Plane Survey at a frequency of 1.4 GHz published by Gaensler et al. (2011).
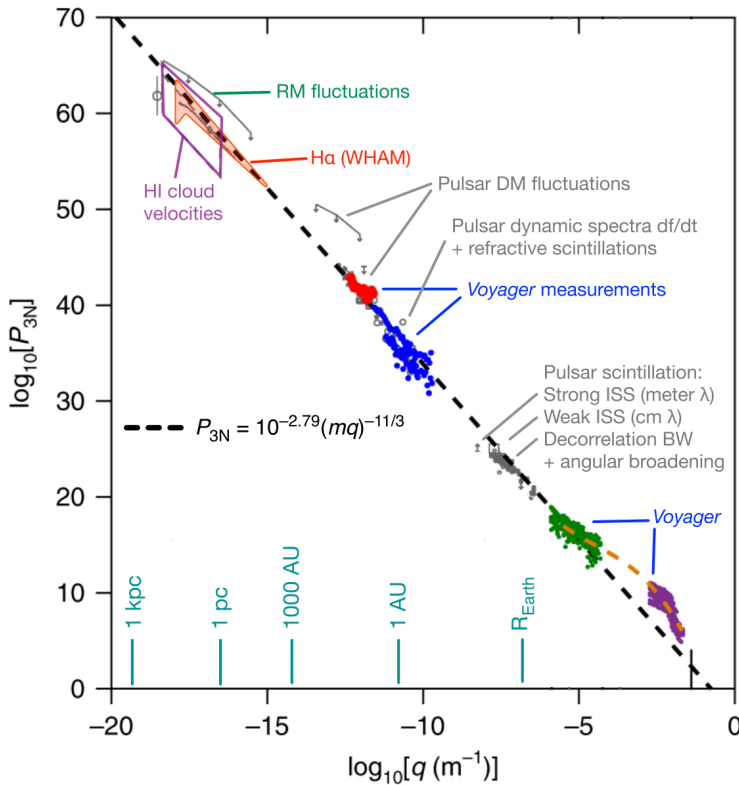
Figure 4.2: Electron density 3D power spectrum with in situ measurements by Voyager Lee and Lee (2019) and remotely measured H-alpha data by Chepurnov and Lazarian (2010) added to the original work by Armstrong et al. (1995). The spectrum can be approximated by a single power law $\sim q^{-11/3}$, in spatial wave number q (in our notation k), over eleven orders of magnitude. For the smallest scales ($q > 10^{-6}\,\mathrm{m}^{-1}$) there is an excess of energy compared to the extrapolated spectrum. Plot taken from Stinebring et al. (2019).

the spectrum for the lower wave numbers down to $k \sim 10^{-17}\,\mathrm{m}^{-1}$ and Chepurnov and Lazarian (2010) provided H-alpha emission data to make these constraints more

tight. The composite spectrum can be approximated with a single power law over eleven orders of magnitude. The spectral slope $\sim k^{-11/3}$ of this 3D power spectrum turns out to be consistent with the prediction by one of the earliest turbulence models proposed by Kolmogorov (1941), which we introduce in the next section and discuss its applicability to the observed electron density power spectrum of the ISM. However, it should be noted that other "non-Kolmogorov" power spectra have been reported by Xu and Zhang (2020a). The authors applied a new method for determining the dispersion measure from pulsar observations and found a shallower (than $\sim k^{-11/3}$) spectrum for the cold interstellar phases, which is characterized by supersonic turbulence, and a steeper spectrum for the diffuse warm medium on kiloparsec scales. On scales below hundreds of parsecs they confirmed a Kolmogorov-like density spectrum for the warm diffuse medium. Although we focus our discussion on the *interstellar* medium we would like to mention that similar spectra have also been observed for the gaseous medium between galaxies, i.e. the *intergalactic* medium. Xu and Zhang (2020b) use fast radio burst observations to infer power law spectra consistent with Kolmogorov's turbulence model with an outer scale of $\sim 100\,\mathrm{Mpc}$. However, their analysis carries a relatively large uncertainty in the derived spectral index.

4.2 Discussion with Kolmogorov's turbulence model

Turbulence has been intensively studied within the framework of fluid dynamics but a general and complete description is still an unsolved challenge. Multiple models have been proposed and reviewed (Landau and Lifschitz, 1986; Brandenburg and Lazarian, 2013). These models typically predict scaling relations associated with some statistical properties of the fluid's density or velocity field. In the following we provide a brief introduction of some essential quantities of fully developed, isotropic and stationary hydrodynamic turbulence. We follow a heuristic and instructive derivation of the model first proposed by Kolmogorov (1941), which applies to incompressible flows with a statistically isotropic and homogeneous velocity field.

For an incompressible fluid with density ρ, pressure p, kinematic viscosity ν (with $[\nu] = \mathrm{L}^2\mathrm{t}^{-1}$) the continuity equation is $\nabla \cdot \boldsymbol{v} = 0$ and in the absence of external forces the Navier-Stokes (NS) equation (see section 2.2.3) is

$$\rho\frac{\partial \boldsymbol{v}}{\partial t} = \underbrace{\rho\nu\nabla^2\boldsymbol{v}}_{\text{viscosity}} - \underbrace{\rho(\boldsymbol{v}\cdot\nabla)\boldsymbol{v}}_{\text{advection}} - \underbrace{\nabla p}_{\text{pressure}} \ . \tag{4.1}$$

On the right hand side of the equation we identify one term respectively for viscosity, advection and pressure. The viscous term is responsible for the dissipation of kinetic energy of the flow. The nonlinear advection term allows for a spectral transfer of kinetic energy and physically represents the inertia of fluid elements. The relative importance of these two terms can be estimated by replacing the spatial derivative ∇ simply with some inverse length scale l_0^{-1} and the velocity vector $\boldsymbol{v}$ with some velocity magnitude v_0 which is characteristic for flow on the spatial scale l_0. For example l_0 could be the diameter of the system and v_0 the velocity dispersion within this system. The ratio of advection to viscous term can then be written as

$$\frac{\rho(\boldsymbol{v}\cdot\nabla)\boldsymbol{v}}{\rho\nu\nabla^2\boldsymbol{v}} \sim \frac{\rho l_0^{-1}v_0^2}{\rho\nu l_0^{-2}v_0} = \frac{l_0 v_0}{\nu} \equiv \mathrm{Re}. \tag{4.2}$$

The introduced Reynolds number Re is dimensionless and allows to distinguish different regimes of streaming properties for a viscous fluid. For Re $\sim$ 1 both viscosity and inertia are important and, at least for appropriate initial and boundary conditions, the fluid flow will be laminar. For Re $\gg 10^3$ inertia clearly dominates over viscosity and the fluid flow will be turbulent.[1]

Energy cascade

Considering a flow with sufficiently large Reynolds number the advection term dominates which effectively redistributes kinetic energy from lower to higher wavenumbers. We take a concrete example to demonstrate how this spectral energy transfer works. If a one dimensional flow starts with a sinusoidal velocity field, $v(x) = sin(kx)$, then the advection term is given as $v\partial_x \sin(kx) = k\sin(kx)\cos(kx) = \frac{k}{2}sin(2kx)$. Hence, the advection term produces a sine wave with twice the wavenumber compared to the initial wave and again enters into the Navier Stokes equations. This sine wave is again affected by the advection term such that the cycle continues to higher and higher wavenumbers. Effectively this generates an energy cascade from low to high wavenumbers with negligible energy dissipation until the viscous term becomes important. The dissipation-free range is called the intertial range (inertia dominates), ranging from the outer scale $l_0 \sim k_0^{-1}$ to the dissipation scale $l_d \sim k_d^{-1}$. Here we simply ignore factors of 2π when converting from wavelengths l to wavenumbers k which are defined as $k = 2\pi/l$.

Figure 4.3 illustrates the idea of this turbulent energy cascade. On the largest scales (outer scale l_0) energy is injected which generates eddies (or whorls) which successively break down into smaller ones and thereby transporting kinetic energy from large to small scales at a constant rate. This process continues until the viscosity of the fluid dissipates the kinetic energy of the fluid into heat and radiation. The idea goes back to Richardson in 1922 who also contributed a little poem (printed in a more recent edition of his book (Richardson, 2007).

> *Big whorls have little whorls*
> *Which feed on their velocity,*
> *And little whorls have lesser whorls*
> *And so on to viscosity.*

From this phenomenological description of turbulence it is possible to derive the spectral shape of the kinetic energy of the fluid by just a few simple arguments motivated by dimensional analysis. Therefore we introduce the following quantities:

- length scale l for the size (or wavelength) of an eddy with wavenumber $k = 2\pi/l \sim l^{-1}$

- velocity $v(l)$ characteristic for an eddy of size l (e.g., the velocity dispersion over the distance l)

- time scale $\tau_l \sim l/v(l)$ (equivalently we write $\tau(k) \sim (kv(k))^{-1}$) known as *eddy turnover time*

---

[1]The critical Reynolds number Re $\sim 10^3$ provides only an order of magnitude and may vary for different systems. It is commonly inferred from laboratory experiments (Frisch, 1995).
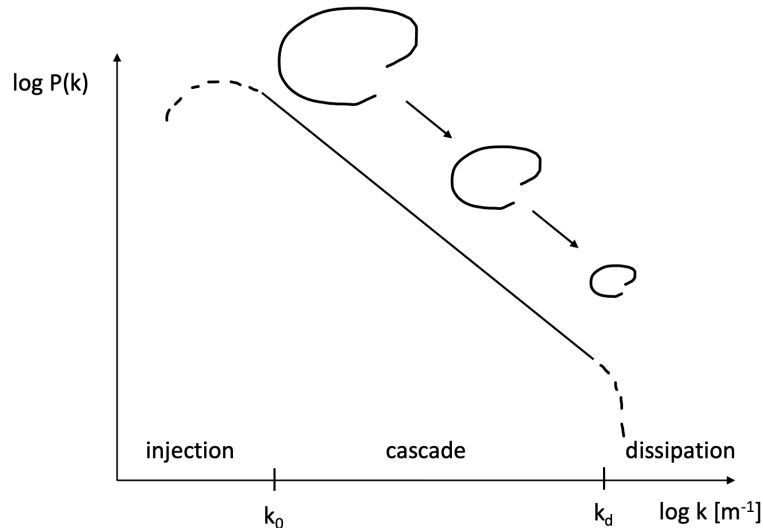
Figure 4.3: This sketch illustrates the energy cascade in turbulence. Energy is injected to the fluid flow at the lowest wavenumbers ($k \sim k_0$), meaning on the largest spatial scales, and transported at a constant rate over the entire inertial range ($k_0 < k < k_d$) until it becomes dissipated on the smallest spatial scales corresponding to the highest wavenumbers ($k \sim k_d$).

Before proceeding it is instructive to emphasize two underlying assumptions. First, we postulate the localness of interactions meaning that the flux of energy at a given length scale l predominantly involves comparable length scales.[2] Second, we postulate the energy cascade to proceed in a self-similar fashion with a constant flux of energy ϵ over the inertial range with $[\epsilon] = \mathrm{eVg^{-1}s^{-1}}$ (energy per mass per time). From these two assumptions it is straightforward to derive the formula for ϵ by dimensional analysis. In fact, dimensional analysis necessarily leads to power law functions (for an extensive treatment see Henriksen, 2015) such that the derived power law scaling is essentially given by the basic construction of the model. The resulting power law relationship of the turbulent power spectrum can also be understood as a direct consequence from demanding the energy cascade to occur with a constant transport rate in a self-similar fashion.

Although the viscosity is responsible for the dissipation of energy at the bottom of the energy cascade for the inertial range ϵ must be independent of ν because of the localness of the interactions and the dominance of inertia over viscosity in this wavenumber range. For a given wavenumber k in the inertial range the turbulent energy transport rate, ϵ, must depend on a combination of the fluid's characteristic scales which are the density ρ (constant for incompressible fluids), velocity $v(k)$ and wavenumber k. The only combination which yields the desired dimensions is

$$\epsilon \sim kv(k)^3 \tag{4.3}$$

where $\epsilon \approx \mathrm{const}$ for the inertial range. This transport rate (also dissipation rate) can also be written in a more intuitive way as $\epsilon \sim v^2(k)/\tau(k)$, representing the

---

[2]This argument is best understood in Fourier space by saying that coupling is dominated between modes of comparable wavenumbers. In physical space smaller eddies are naturally embedded in larger eddies and therefore entire eddies will be transported relative to the rest frame of the fluid but this larger scale motion is unimportant for the energy flux within the eddies.

kinetic energy per unit mass per eddy turnover time. From it we can derive the wavenumber or length scale dependent scaling of the velocity

$$v(k) \sim \epsilon^{1/3} k^{-1/3}, \tag{4.4}$$

$$v(l) \sim \epsilon^{1/3} l^{1/3}. \tag{4.5}$$

Taking a concrete example these results tell us that the velocity dispersion and the eddy turnover time within a given turbulent system increase with the size of the subsystem to the power of 1/3 and 2/3 respectively. The spectral energy density $E(k)\mathrm{d}k = \frac{1}{2}\frac{v^2(k)}{k}\mathrm{d}k$ therefore scales with wavenumber according to

$$E(k) \sim k^{-5/3}. \tag{4.6}$$

For isotropic turbulence the power spectrum depends only on the magnitude of the wave vector. Thus $E(k)\mathrm{d}k = 4\pi k^2 P(k)\mathrm{d}k$, ultimately leads to the 3D spectrum

$$P(k) \sim k^{-11/3} \tag{4.7}$$

and thereby recovering the observed scaling of the electron density power spectrum in figure 4.2.

In the following we aim to interpret the interstellar electron density spectrum within the given framework. It is important to emphasize that Kolmogorov's power spectrum was derived for the velocity field of some incompressible (i.e., constant density) fluid whereas the Big Power Law is associated with the density field of the interstellar free electrons.[3] We assume the applicability of Kolmogorov's model for turbulence and the associated energy cascade in order to discuss potential mechanisms for energy injection and energy dissipation.

Energy injection

The outer scale of turbulence refers to the length scale at which the largest turbulent eddies are driven. For larger scales (lower wavenumbers) the power spectrum decreases. Consequently, if this spectral break can be identified in the interstellar turbulence power spectrum this would be a clear indication for the scale at which the driving mechanism operates. In figure 4.2 there is no sign for such a break all the way up to about $\sim 10\,\mathrm{pc}$ but there is some considerable uncertainty at these length scales. Haverkorn et al. (2008) used rotation measure fluctuations and inferred an outer scale of a few parsec inside our Galaxy's spiral arms and about a hundred parsec for the interarm regions. The authors interpret these two distinct outer scales as a hint for the different energy injection mechanisms. Within the galactic spiral arms the dominant mechanism could be stellar winds and protostellar outflows whereas in the interarm regions SNe and superbubbles would dominate. In general, and as a galactic average, SNe are commonly assumed to be a major driver of interstellar turbulence (e.g., Ferrière, 2019).

The significance of SNe can also be motivated with an order of magnitude calculation by comparing the average power provided by SNe on galactic scales to the integrated turbulent dissipation rate, Γ_{turb}. For our Galaxy we use an average power

---

[3]In general the velocity fluctuations would be a much more direct tracer of turbulence than density fluctuations but are also more difficult to observe. See Brandenburg and Lazarian (2013) for an overview about velocity statistics in astrophysical turbulence.

for the kinetic energy contribution from SNe, which is $\Gamma_{\mathrm{SN}} \approx 10^{42} \, \mathrm{erg/s}$ derived in equation 1.3. The characteristic length scale for a SNR is $l \sim 100 \, \mathrm{pc}$ which we therefore use as outer scale for the energy injection from SNe (e.g., Bacchini et al., 2020, and references in section 5.4 of their paper). For $v = 10 \, \mathrm{km \, s^{-1}}$ we obtain $\tau \sim 10 \, \mathrm{Myr}$ for the largest eddy turnover time, which can be used as an order of magnitude estimate for the turbulent decay time scale (e.g. Mac Low, 1999; Chamandy et al., 2016). The given value of v is about the same order as the velocity of sound for an ideal gas with $T \sim 10^4 \, \mathrm{K}$, which is the temperature of the warm ISM that fills most of the volume in the galactic disk. The corresponding turbulent energy transport rate is $\epsilon \sim v^2/\tau \sim 1.6 \times 10^{-3} \, \mathrm{erg/gs}$. For our disk galaxy model (defined in the Introduction 1) with $n = 1 \, \mathrm{cm^{-3}}$ we obtain the following galactic average volumetric turbulent kinetic energy density

$$\begin{aligned}
\mathcal{E}_{\mathrm{turb}} &\sim \frac{1}{2} \rho v^2 \\
&\sim 0.5 \, \mathrm{eV/cm^3} \\
&\sim 10^{-12} \, \mathrm{erg/cm^3}.
\end{aligned} \qquad (4.8)$$

The corresponding integrated turbulent decay rate $\Gamma_{\mathrm{turb}} \sim \mathcal{E}_{\mathrm{turb}} V/\tau$ is

$$\Gamma_{\mathrm{turb}} \sim 10^{40} \, \mathrm{erg/s} \qquad (4.9)$$

which is about two orders of magnitude lower than the kinetic power from SNe. Evidently, even if the efficiency for the conversion of SNe energy into gas turbulence is very low, this would still be sufficient to maintain interstellar turbulence in the absence of any other drivers.

Of course this argument provides only a necessary but not a sufficient condition to identify SNe as dominant driver for the observed turbulence. Furthermore, this reasoning applies to the integrated power contribution (i.e., galactic average) whereas locally the relative importance of the various sources may differ. For example in outer parts of the galactic disc with a lower star formation rate the relative contribution from SN driving to turbulence may be less important than in the galactic center with a high star formatin rate. Consequently it is difficult to determine a single source which is responsible for driving interstellar turbulence but a plethora of potential candidates are found. This can be illustrated with the following (possibly incomplete) list of potential drivers behind interstellar turbulence.

- Stellar feedback: SNe, stellar wind, HII-regions, and superbubbles (e.g., Norman and Ferrara, 1996; Padoan et al., 2016; Bacchini et al., 2020)

- Instabilities driven by gravity: galaxy interactions (e.g., Renaud et al., 2014), gas accretion onto the galactic disk (e.g., Elmegreen and Burkert, 2010; Bacchini et al., 2020)

- Galactic shear: due to differential rotation (e.g., Richard and Zahn, 1999; Semelin and Combes, 2000)

- Cloud-cloud collisions (e.g., Dobbs et al., 2011)

The relative importance of the respective energy sources depends both on the particular region (e.g., inner or outer galactic disk, in- or outside of spiral arms) and on the given length scales (e.g., larger regions with hundreds of parsec or inside

a star forming region with sub-parsec extensions) under consideration. For the smaller scales another potential turbulence driver is magnetic field amplification via the cosmic ray streaming instability in the vicinity of supernova shock fronts (e.g., Bell, 2004; Xu and Lazarian, 2022a). There is an ongoing debate on how this power is distributed and to what extent and on which scales and environments the individual energy sources contribute (e.g., Mac Low and Klessen, 2004; Bacchini et al., 2020; Elmegreen et al., 2022). However, at least in star forming environments, SNe certainly play an important rule in driving interstellar turbulence

Energy dissipation

In a purely hydrodynamic, rather than *magneto*-hydronamic, description of turbulence, the energy is dissipated due to the viscosity of the fluid which can be generated from a sort of friction due to colliding particles that make up the fluid. For the Big Power Law (see figure 4.2) we are concerned with the density field of electrons. A first guess could be that the fluid's viscosity results from electrons scattering with each other and thereby loosing energy through bremmstrahlung. In this case the dissipation of energy should be at work roughly at about the electron collision mean free path. Most of the free electrons are part of the WIM for which the electrons have a mean free path $\lambda_e \sim 0.2\,\mathrm{au}$ (see figure 4.4). But the turbulent energy cascade appears to continue to much smaller length scales. Observations from pulsar scintillations (Armstrong et al., 1995) extend the inertial range to about the radius of the Earth ($10^{-5}\,\mathrm{au}$) and Voyager data (Lee and Lee, 2019) goes even further and displays a flatter rather than steeper spectrum at about hundred kilometers ($10^{-6}\,\mathrm{au}$) in length scale and measured locally in the vicinity of our solar system. This observation appears to be in tension with earlier studies who reported the inner scale to be at about a few hundred kilometers (Molnar et al., 1995; Spangler and Gwinn, 1990). Given these observations, it is difficult to determine a length scale for interstellar turbulence at which dissipative processes dominate.[4]

The characteristic scales listed in figure 4.4 suggest that the electron density fluctuations are collissionless for the shorter wave lengths. Consequently, at least for the smaller scales, there have to be other processes responsible for transporting and dissipating energy. This is not surprising however. After all, the fluid we are concerned with consists of electric charges and carries a magnetic field with it. Plasma physics and MHD are therefore necessary to accurately describe the processes at work for dissipating the turbulent energy. Here we do not go into the details of this framework but only mention the most prominent dissipation mechanisms relevant to our case of electron density fluctuations. For a review on MHD turbulence see Beresnyak (2019).

In MHD the fluctuations of the fluid are comprised of three different wave modes: Alfvén waves, and slow or fast magnetosonic waves. According to Ferrière (2019) the fast and slow modes are mostly dissipated by viscous damping in the collisional regime $l \gg \lambda_p$ with proton collision mean free path $\lambda_p \simeq \sqrt{2}\lambda_e$. Alfvén modes cascade almost undamped down to λ_p and are dissipated by Landau damping at length scales near the proton inertial length, $r_p = V_A/\Omega_p$, and proton gyro radius,

---

[4]Different turbulent environments may also be dominated by other dissipation mechanisms. For example in molecular clouds the fraction of neutral atoms is a lot higher and ambipolar diffusion is the dominant dissipation process according to Krumholz (2014).

	CNM	WNM	WIM	HIM
T (K)	80	5000	8000	10^6
n_H (cm^{-3})	30	0.4	0.2	0.005
n_e (cm^{-3})	0.02	0.01	0.2	0.006
C_s (km s^{-1})	0.7	6	10	120
V_A (km s^{-1})	1.7	15	20	130
ω_e (kHz)	8	5.5	25	4
$|\Omega_\text{e}|$ (Hz)	90	90	90	90
r_e (km)	0.6	5	6	60
τ_e	9 min	5 d	12 h	45 year
λ_e	5 $R_\oplus$	1.3 AU	0.17 AU	0.3 pc
L (pc)	10	30	30	100
V (km s^{-1})	3	10	10	30
Re	4×10^{10}	10^7	5×10^7	10^2
Re$_m$	7×10^{14}	3×10^{18}	5×10^{18}	5×10^{22}
P$_m$	2×10^4	3×10^{11}	10^{11}	5×10^{20}

Figure 4.4: These are typical values in the four different ISM phases (CNM = cold neutral, WNM = warm neutral, WIM = warm ionized, HIM = hot ionized medium). Here, T is the gas temperature, n_H the hydrogen number density, n_e the free electron number density, $C_\text{s} = \sqrt{P_\text{th}/\rho}$ the isothermal sound speed with mass density ρ and thermal pressure P_th, $V_A = \sqrt{2P_\text{B}/\rho}$ the Alfvén speed with magnetic pressure $P_B = B^2/(8\pi)$, $\omega_\text{e} = \sqrt{4\pi n_\text{e}e^2/m_\text{e}}$ the plasma frequency, $\Omega_\text{e} = -eB/(m_\text{e}c)$ the electron gyro frequency, $r_\text{e} = v_{\perp e}|\Omega_\text{e}|$ the electron gyro radius , $\tau_\text{e} \sim T^{1.5}/n_\text{e}$ the electron collision time, $\lambda_\text{e} \sim T^2/n_\text{e}$ the electron collision mean free path, L a typical length scale, V a characteristic velocity, Re $= VL/\nu$ the standard (fluid) Reynolds number with kinematic viscosity ν, Re$_m = VL/\eta$ its magnetic counterpart with magnetic diffusivity η, $P_m = $ Re$_m$/Re the magnetic Prandtl number. The enormous variations in Re and Re$_m$ between the CNM and the HIM is a consequence of Re $\propto \nu^{-1} \propto n_\text{e}T^{-2.5}$ and Re$_m \propto \eta^{-1} \propto T^{1.5}$. Generally, the large Reynolds numbers are in agreement with a turbulent interstellar medium in all phases. The values of V_A, Ω_e and r_e are obtained for $B = 5\,\mu$G corresponding to a magnetic pressure $P_B \sim 1\,\text{eV/cm}^3$. Table taken from Ferrière (2019).

$r_\text{p} = v_{\perp\text{p}}/\Omega_\text{p}$, which are both of order few hundred kilometers for the WIM where values and definitions are found in figure 4.4.

Evidently, Kolmogorov's 1941 turbulence model with a dissipation free energy cascade from large to small scales provides only a crude description of interstellar turbulence and does not represent the physical reality of the interstellar medium accurately. Furthermore, the power spectrum with $E \sim k^{-5/3}$, which is characteristic for Kolmogorov's model, can also be generated by other models of turbulence (e.g., Goldreich and Sridhar, 1995). The deviations in the assumptions by Kolmogorov's model and the reality of interstellar turbulence is manifold and can be illustrated by the following (possibly incomplete) list.

- not a single energy source: energy is injected at multiple scales with different mechanisms

- not a single energy sink: energy is dissipated at multiple scales with different mechanisms

- no clear separation of scales: injection, inertial and dissipation ranges are not fully distinct but overlap with each other

- not purely hydrodynamic: most of the volume of the ISM is magnetized and therefore governed by magnetohydrodynamic (MHD) turbulence

- not isotropic: magnetic fields, galactic rotation and other factors introduce anisotropy into the fluid flow and transport of energy

- not homogeneous: the ISM has at least three phases with different compositions, temperatures and densities

- not incompressible: pressure and density are not constant and shock waves propagate through the medium

- not subsonic (scale dependent): some regions of the ISM are transsonic (e.g., warm medium) or even supersonic (e.g., molecular clouds)

In summary, it is neither possible to determine a single dominant driver for turbulence nor is there a single mechanism responsible for dissipation which is valid for all of interstellar turbulence. Both sources and sinks of turbulent energy depend on the properties of the ISM. Collectively, all these different mechanisms and environments, lead to the well structured power spectrum known as Big Power Law in the Sky shown in figure 4.2.

4.3 Magnetic fields

Magnetic fields are omnipresent in the ISM and interstellar turbulence is an important driver not only for shaping the topology of the field but also for converting kinetic into magnetic energy. All observations for the magnetic fields are rather indirect and involve different tracers. Polarized infrared emission from interstellar dust is one possibility exploited by the Planck satellite image in figure 4.5. Additionally, synchrotron emission, its polarization and Faraday rotation are essential for inferring both magnetic field strength and the orientation of the field lines. In spiral galaxies large scale magnetic fields with $B \sim 10\,\mu$G are typical (e.g., Fletcher, 2010; Beck, 2012). This corresponds to a magnetic field energy density of

$$\frac{B^2}{8\pi} \sim 4 \times 10^{-12}\,\text{erg/cm}^3. \tag{4.10}$$

In the vicinity of SN shock fronts stronger (small scale) magnetic fields with $50 - 100\,\mu$G have been inferred (e.g., Berezhko et al., 2003; Ressler et al., 2014). In most spiral galaxies (large-scale) ordered magnetic fields are observed with an orientation
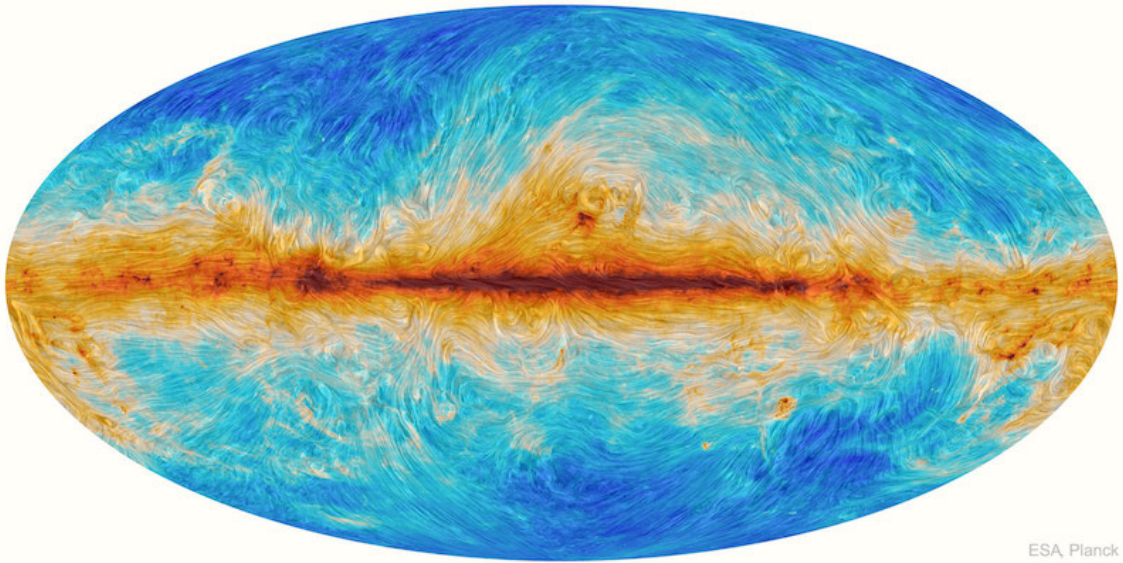
Figure 4.5: All sky image of our Galaxy taken by the Planck satellite. The galactic plane is distinguished by more intense dust emission which is indicated via the colour scale. The polarisation of the dust emission is represented via the texture and traces the orientation of the magnetic field which turns out to be largely parallel to the galactic plane. The emission from dust is computed from a combination of Planck observations at 353, 545 and 857 GHz, whereas the direction of the magnetic field is based on Planck polarisation data at 353 GHz. Image credit: ESA and the Planck Collaboration.

parallel to the galactic plane which can be interpreted as a result from a mean-field dynamo. However, the overall structure is more complicated (e.g., Beck, 2012; Beck et al., 2020) and on the top of ordered field there is an irregular or turbulent component of the magnetic field. In the following we aim to outline the connection between interstellar turbulence and magnetic field amplification.

We follow the same convention as Brandenburg and Subramanian (2005) and express the magnetic field in units of Gauss (i.e., $[B] = G$ with $1\,\mathrm{G} = 10^{-4}\,\mathrm{T} = 10^{-4}\,\mathrm{kg A^{-1} s^{-2}}$) and write down Maxwell's equations in SI units as follows

$$\nabla \cdot \boldsymbol{E} = \frac{\rho}{\epsilon_0} \tag{4.11}$$

$$\nabla \cdot \boldsymbol{B} = 0 \tag{4.12}$$

$$\nabla \times \boldsymbol{E} = -\frac{\partial \boldsymbol{B}}{\partial t} \tag{4.13}$$

$$\nabla \times \boldsymbol{B} = \mu_0 \left(\boldsymbol{j} + \epsilon_0 \frac{\partial \boldsymbol{E}}{\partial t} \right) \tag{4.14}$$

where $\boldsymbol{E}$ is the electric field, $\boldsymbol{B}$ is the magnetic field, ρ is the charge density, $\epsilon_0 = 1/(\mu_0 c^2)$ is the vacuum permittivity, μ_0 is the vacuum permeability, c is the speed of light, $\boldsymbol{j}$ is the current density. Furthermore, we introduce the electric conductivity σ and the magnetic diffusivity $\eta = 1/(\mu_0 \sigma)$. In the following we simply set $\mu_0 = \epsilon_0 = 1$, which implies $\eta = 1/\sigma$.

For the ISM in our galactic disk, and various other astrophysical environments (discussed in section 3.2 in Brandenburg and Subramanian, 2005), the high conduc-

tivity of the plasma allows us to neglect the displacement current term in equation (4.14) such that it reduces to

$$\nabla \times \boldsymbol{B} = \boldsymbol{j} \tag{4.15}$$

which is known as Ampere's law. The current density $\boldsymbol{j}$ is subject to Ohm's law,

$$\boldsymbol{j} = \sigma(\boldsymbol{E} + \boldsymbol{v} \times \boldsymbol{B}), \tag{4.16}$$

where $\boldsymbol{v}$ denotes the velocity field of the plasma. We can use this equation to express the electric field as

$$\begin{aligned} \boldsymbol{E} &= \eta\boldsymbol{j} - \boldsymbol{v} \times \boldsymbol{B} \\ &\stackrel{(4.15)}{=} \eta\nabla \times \boldsymbol{B} - \boldsymbol{v} \times \boldsymbol{B}. \end{aligned} \tag{4.17}$$

which we use to eliminate $\boldsymbol{E}$ from Faraday's law of induction (4.13) and obtain the following general form of the induction equation

$$\frac{\partial \boldsymbol{B}}{\partial t} = \nabla \times (\boldsymbol{v} \times \boldsymbol{B}) - \nabla \times (\eta\nabla \times \boldsymbol{B}). \tag{4.18}$$

Exploiting the following well-known formula $\nabla \times (\nabla \times \boldsymbol{a}) = \nabla(\nabla \cdot \boldsymbol{a}) - \Delta\boldsymbol{a}$, with Laplace operator $\Delta = \nabla \cdot \nabla$, which holds for arbitrary vectors $\boldsymbol{a} \in \mathbb{R}^3$ (p. 302 in Lang and Pucker (2010). Setting $\boldsymbol{a} = \boldsymbol{B}$, and using Gauss's law for magnetism (4.12), yields the following identity

$$\nabla \times (\nabla \times \boldsymbol{B}) = -\Delta\boldsymbol{B}. \tag{4.19}$$

Provided that the magnetic diffusivity η is constant over the entire space, we obtain the following form of the induction equation

$$\begin{aligned} \frac{\partial \boldsymbol{B}}{\partial t} &= \nabla \times (\boldsymbol{v} \times \boldsymbol{B}) - \eta\nabla \times (\nabla \times \boldsymbol{B}) \\ &\stackrel{(4.19)}{=} \nabla \times (\boldsymbol{v} \times \boldsymbol{B}) - \eta\Delta\boldsymbol{B}. \end{aligned} \tag{4.20}$$

The vector-product term $(v \times \boldsymbol{B})$ is commonly referred to as *induction term* and it is useful to expand it further by exploiting another formula, that is $\nabla \times (\boldsymbol{a} \times \boldsymbol{b}) = \boldsymbol{a}(\nabla \cdot \boldsymbol{b}) - \boldsymbol{b}(\nabla \cdot \boldsymbol{a}) + (\boldsymbol{b} \cdot \nabla)\boldsymbol{a} - (\boldsymbol{a} \cdot \nabla)\boldsymbol{b}$, which holds for arbitrary vectors $\boldsymbol{a}, \boldsymbol{b} \in \mathbb{R}^3$ (p.302, Lang and Pucker, 2010). Again, Gauss's law for magnetism, equation (4.12), eliminates the $\nabla \cdot \boldsymbol{B}$ -term such that we can rewrite the induction equation as

$$\frac{\partial \boldsymbol{B}}{\partial t} = \underbrace{(\boldsymbol{B} \cdot \nabla)\boldsymbol{v}}_{\text{stretching}} - \underbrace{\boldsymbol{B}(\nabla \cdot \boldsymbol{v})}_{\text{compression}} - \underbrace{(\boldsymbol{v} \cdot \nabla)\boldsymbol{B}}_{\text{advection}} - \underbrace{\eta\Delta\boldsymbol{B}}_{\text{diffusion}}. \tag{4.21}$$

Evidently, the dynamics of the magnetic field are determined by the net effect of stretching, compression, advection and diffusion. An essential property about plasmas with high conductivity is known as *flux freezing* (e.g., Brandenburg and Subramanian, 2005). In the limit of $\eta \to 0$ (equivalent to $\sigma \to \infty$) it guarantees a constant magnetic flux. Considering a flux tube of length l with surface A we require BA to be constant. Conservation of mass requires $\rho A l$ to be constant and hence $B \propto \rho l$. And for (nearly) incompressible fluids $B \propto l$. Thus, any fluid motion which stretches the tube length l automatically amplifies the magnetic field. An
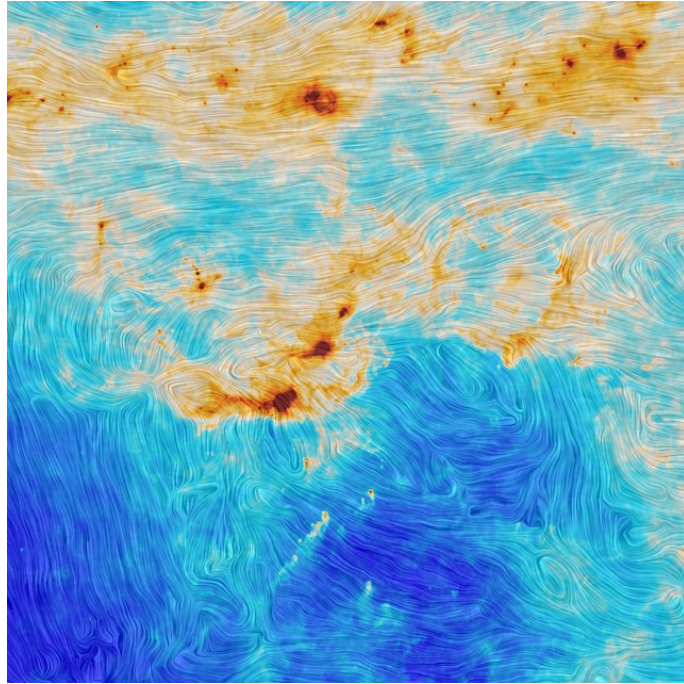
Figure 4.6: This Planck satelite image depicts the Orion Molecular Cloud. The magnetic field lines are largely ordered and parallel to the galactic plane (located above the top of this image) whereas the topology of the magnetic field varies more strongly in the vicinity of the denser and star forming regions (e.g., near the darkest clump on the lower left which is the Orion Nebula). The emission from dust is computed from a combination of Planck observations at 353, 545 and 857 GHz, whereas the direction of the magnetic field is based on Planck polarisation data at 353 GHz. Image credit: ESA and the Planck Collaboration.

important mechanism operating on larger galactic scales is the α-Ω-dynamo (e.g., Kulsrud and Zweibel, 2008) which is driven by the differential rotation in a galactic disk. The small-scale or turbulent dynamo operates on smaller scales and can be directly related to the turbulent power spectrum as we demonstrate in the following while referring to Batchelor (1950) and Kulsrud and Zweibel (2008) for a complete derivation.

Kulsrud and Zweibel (2008) show that for the kinematic regime, where the back-reaction of the magnetic field on the kinematics of the flow can be neglected, the magnetic energy at a given wave number grows exponentially at a rate that depends on the eddy turnover time in Kolmogorov's turbulence model. At a given wavenumber the magnetic field becomes amplified until the back-reaction of the magnetic field on the plasma flow becomes signifcant and a nonlinear theory is required as for example proposed by Xu and Lazarian (2016). In this regime the magnetic field grows only linearly in time until the magnetic field energy saturates with the turbulent kinetic energy. This equipartition is first reached for the largest wave numbers (small scales) and than spreads in an inverse cascade to the lower wavenumbers (large scales). An upper limit for the growth of magnetic energy is set by the turbulent energy at the outer scale of turbulence. After sufficient time it is thus reasonable to expect the turbulent dynamo creating an equipartition of energy, at least as an order of magnitude estimate, such that

$$\frac{B^2}{8\pi} \sim \frac{1}{2}\rho v^2 \tag{4.22}$$

with v being the characteristic turbulent velocity on the largest scale. Given the turbulence model considered above with the turbulent kinetic energy density of $\sim 10^{-12}\,\mathrm{erg/cm^3}$ energy equipartition corresponds to a magnetic field strength $B \sim 6\,\mu\mathrm{G}$ which agrees with observations in the range of given uncertainties. The equipartition of turbulent and magnetic energy at the outer scale of turbulence has also been found in dynamo simulations with SN-driven turbulence by Schober et al. (2013). The large scale coherence of magnetic fields is thought to be a result of the α-Ω-dynamo and the differential rotation of the galaxy (e.g., Beck et al., 2020).

Chapter 5

Star Formation

Star formation involves many physical mechanisms acting in concert, including gravity, hydrodynamics, magnetic fields, radiation, and chemistry. While all of these processes have a role to play, understanding the whole picture is difficult without first understanding how various subsets of these mechanisms work together. Above all, it is important to explore how star formation arises from the interplay of gravity and turbulence, which provide the canvas upon which other physics can be painted.
(Guszejnov et al., 2020)

5.1 Initial Mass Function

5.1.1 Observations

The stellar Initial Mass Function (IMF) is a crucial element of star formation theory and it has profound implications for a variety of other fields in astrophysics. The IMF represents the number of newly formed stars per interval in mass. From an observational perspective we can think of it as a sort of histogram one would obtain if it was possible to count the number of stars within a given interval of mass at the moment when they enter the main sequence of the Hertzsprung-Russel diagram. Unfortunately, such a direct assessment is not feasible for multiple reasons. Determining the IMF from observational data is a long and indirect procedure where errors and systematic biases can enter in various ways. Here we shall only provide a short overview in order to have a better understanding about the uncertainties associated with determining the IMF. In essence there are three major difficulties:

1. *Mass-luminosity relation:*
   The luminosity and mass of a star are connected via an empirical relation which depends on the star's age, its chemical composition and its spin. For low mass and pre-main-sequence stars the inherent uncertainties are particularly high.

2. *Converting present day to initial mass function:*
   Even young star clusters are typically observed at an age of a few 10^7 years which means that the most massive stars have already left the main sequence while some very low mass stars have not even yet reached it. Thus stellar evolutionary models inevitably need to be invoked, whereas on galactic scales the star formation history becomes important additionally, in order to reconstruct the *initial* mass function from present day observations.

3. *Assessing all stars:*
   For any system of stars, be it a cluster or a galaxy, it is important to obtain a fairly complete sample of stars. In practice this can be challenging for many reasons. The image resolution constrains the ability to detect low mass stars due to their lower luminosity. The multiplicity of stellar systems is another obstacle because individual stars cannot always be resolved. Dust extinction complicates observations even more. Dynamical evolution of star clusters typically leads to mass segregation such that more massive objects arrange near the center while the lower masses tend to settle further outside. Ultimately, these lower mass stars can be ejected from the cluster due to gas expulsions from the inner high mass stars. In this case, the observed sample is incomplete and needs to be corrected by applying dynamical models for star clusters.

Evidently, determining the IMF is a lengthy procedure which inevitably involves empirical relations or theoretical models. These difficulties are well acknowledged in the literature. Kroupa et al. (2013) refers to the second problem in the above list with his *IMF unmeasurability theorem* which states "the IMF cannot be extracted directly for any individual stellar population". The theorem is justified by considering the time scales of star formation. Since for any cluster of stars the most massive stars have already left the main sequence even before star formation has ceased there is no time when all stars have fully assembled and are observable. The *initial* mass function is therefore rather a theoretical construction than a directly accessible physical quantity.
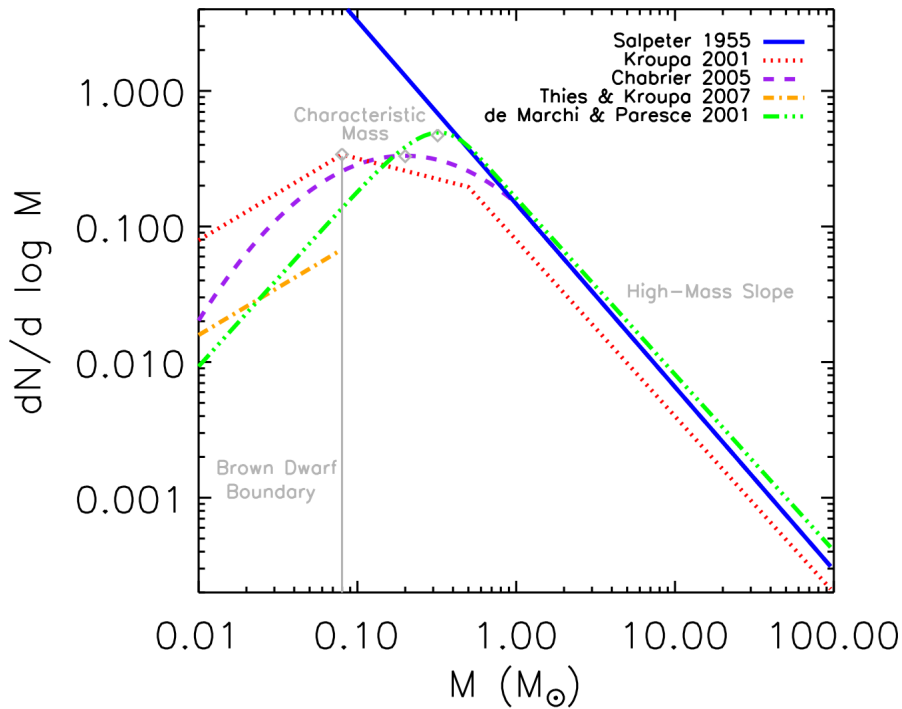

Figure 5.1: The most prominent IMF models are shown which all converge to Salpeter's power law for higher masses but vary slightly from each other for sub-stellar masses ($M_\odot$). The brown dwarf regime is particularly uncertain due to the observational difficulties mentioned above. The plot is taken from Offner et al. (2014).

Characterizing the shape of the IMF goes back to Salpeter (1955) who found the differential number of stars $\mathrm{d}N$ with masses in the range of $0.4 - 10\mathrm{M}_\odot$ to be best fit by a power law,

$$\mathcal{N}_\star(M) = \frac{\mathrm{d}N}{\mathrm{d}M} \propto M^{-\alpha}, \qquad (5.1)$$

with $\alpha \approx 2.35$. More precisely, the original paper used another convention for which the IMF is defined as the number of stars per logarithmic interval of mass such that

$$\frac{\mathrm{d}N}{\mathrm{d}\log M} \propto M^{-\Gamma}, \qquad (5.2)$$

for which the exponents of the two conventions are related by $\Gamma = \alpha - 1$. Since its first detection there have been numerous studies fitting observational data with different functional forms. An overview of the most established IMF functions is given by figure 5.1. In fact, the power law shape for the larger mass has become quite established but even in 1955 Salpeter must have known that his power law prescription must break down for lower mass at some point since a diverging number of low mass stars is not reasonable.

This turnover has its peak at about $M_\mathrm{c} \approx 0.2 - 0.3\mathrm{M}_\odot$ (Offner et al., 2014) which sets a characteristic scale for the IMF. In this way the IMF can be split into two parts: a low mass and a high mass regime for $M \gtrsim 1\,\mathrm{M}_\odot$. The low mass range can be fit with a lognormal distribution as defined by Chabrier (2003) (or with other similarly shaped functions) whereas the high mass range is characterized by Salpeter's power law dependence with $\alpha \approx 2.3 - 2.4$ according to Krumholz (2014). This scale-free part of the IMF is assumed to span a range of nearly two orders of magnitude (Offner et al., 2014). However, the high mass range is difficult to constrain strictly from observations.

Is the IMF universal?

Intuitively one would expect the IMF to be sensitive on the local conditions of the star forming region. There are numerous potential factors which could affect the complex process of a collapsing gas cloud until it turns into a star in hydrostatic equilibrium for which its future evolution is determined by its initial mass. Nevertheless, not all of these parameters need to affect the initial mass function. On the other hand, there are some particular properties of star forming regions for which we have conclusive arguments that they should affect stellar masses produced within that region. Here we consider only one illustrative example, namely the abundance of heavier elements which is commonly referred to as *metallicity*. The higher the metallicity in a gas cloud the higher its cooling rate. Consequently we would expect the metallicity in a star forming environment to affect the slope of the IMF for at least two reasons:

- Jeans Mass argument (clouds collapse only if $M > M_\mathrm{J} \propto \sqrt{T^3/\rho}$ as we discuss below in section 5.1.2):
  low metallicity $\rightarrow$ less effective cooling $\rightarrow$ higher temperature $\rightarrow$ higher Jeans mass ($M_\mathrm{J} \propto T^{3/2}$) $\rightarrow$ low mass objects do not collapse
  $\rightarrow$ top heavy IMF

- Self regulatory ansatz (accretion vs. feedback):
  low metallicity $\rightarrow$ photons couple more weakly to accreted gas + lower cooling

rate means higher sound speed ($c_s \propto \sqrt{T/\rho}$) $\rightarrow$ higher mass accretion rate with nonlinear dependence on mass $\rightarrow$ higher mass objects accrete more mass $\rightarrow$ top heavy IMF

Following this reasoning, and in the absence of additional metallicity-related effects, one would expect a top-heavy IMF (excess of high mass stars) for low metallicity environments and a bottom-heavy (excess of low mass stars) IMF for metal rich environments. This "variable IMF prediction" (Kroupa et al., 2013) can be tested observationally by comparing IMFs obtained for different regions or earlier times in cosmic evolution for which the metallicity was lower.[1]

Over the last decades a lot of literature has been published reporting about deviations from IMF universality (e.g., Hopkins, 2018, and references therein). Such claims should be considered carefully because, as explained above, the IMF is not a directly accessible quantity but necessarily involves model assumptions and therefore may be systematically biased. Observations of resolved stellar populations in the Milky Way and nearby galaxies enable counting stars whereas studies of more distant galaxies cannot resolve individual objects and involve different methods to infer the IMF (e.g., stellar population synthesis) (Guszejnov et al., 2019). Additionally, most observations are constrained to a fairly small range of masses since low mass stars are only detectable on short distance while high mass stars are limited to actively star forming regions due to their short lifetimes. Therefore, the robustness of different results has to be checked carefully to avoid misleading conclusions about the apparent (non-)universality of the IMF. The following claims on IMF deviations in rather extraordinary environments are worth emphasizing.

- Bottom-heavy IMF for some giant elliptical galaxies (e.g., Dokkum and Conroy, 2010; Cappellari et al., 2012; Oldham and Auger, 2018; Smith, 2020)

- Top-heavy IMF for some star clusters near Milky Way center (e.g., Bartko et al., 2010; Lu et al., 2013; Hosek et al., 2019)

- Top-heavy IMF in globular clusters with higher density and lower metallicity (e.g., Marks et al., 2012)

- Top-heavy IMF for some ultra faint dwarf galaxies (e.g., Geha et al., 2013; Guszejnov et al., 2019)

Offner et al. (2014) concludes there is "no compelling evidence for substantial IMF variations for resolved stellar populations in the local universe". Other reviews draw similar conclusions (e.g., Bastian et al., 2010; Kroupa et al., 2013). However, in a more recent review Hopkins (2018) claims "a growing wealth of evidence points against a universal IMF". But even if the IMF may not be perfectly universal, it appears to be remarkably independent of the particular environmental conditions.

It is worth clarifying some subtleties in the notion of universality which are frequently not clearly addressed. First, we must define the size of the system for which we consider the IMF. This could be a star-forming region, an entire galaxy or even an ensemble of galaxies at a given epoch of cosmic evolution. Therefore, Hopkins (2018) suggests to distinguish stellar, galactic and cosmic IMFs. Possibly

---

[1]However the mass-luminosity relation needed for determining the stellar mass also depends on the metallicity of the star and these two factors could potentially "conspire" in such way that the resulting IMF turns out to be relatively insensitive to variations in metallicity.

there is a universal IMF for (at least some types of) galaxies at our given epoch in cosmic time. This could be the result of a superposition of different IMFs on a level of star-forming regions. The universality on a galactic scale could be result of an averaging process over all star-forming regions. Alternatively, if the IMF turns out to be universal even on the level of individual (large enough) star-forming regions the universality on a galactic level would be a direct consequence. This latter scenario, a universal stellar IMF, is particularly interesting because it hints on the dominance of some universal mechanism which appears to operate independently of environmental parameters which characterize different star-forming regions.

5.1.2 Discussion

Ideally the origin of the IMF would be discussed within a more complete theory of star formation which takes into account all the relevant physical processes. This turns out being an extremely challenging task for multiple reasons. First, the spatial scales cover a range of about seven orders of magnitude for giant molecular clouds with $d \lesssim 100 \, \text{pc}$ collapsing to protostars with $d \sim 10^{-5} \, \text{pc}$ which cannot be resolved over the entire dynamical range in hydrodynamic simulations (e.g., Guszejnov and Hopkins, 2016). Second, the dynamical equations describing the turbulent and magnetized fluid are in general very hard to solve without simplifying assumptions like an equation of state for the gas which can only accurately describe a certain evolutionary period of the collapsing cloud (e.g., Krumholz et al., 2007). Third, the collapse is governed by a competition of multiple physical mechanisms like shock fronts and self-gravity responsible for compressing the gas cloud vs. thermal pressure, turbulent motion of the gas, radiation and magnetic fields which are all supporting the cloud against compression. Therefore a broad range of physics needs to be connected in order to describe the collective actions and reactions adequately. Fourth, there are poor observational constraints for some important parameters inside molecular clouds like the magnetic field, velocity and density distributions in 3D (e.g., Scalo, 1990; Mac Low and Klessen, 2004; Beattie et al., 2019). Last but not least, star formation is not an isolated process but stars typically form in clusters within larger star forming regions such that the formation process of a single star is affected by its environment (e.g., radiation and turbulence as investigated by Mathew and Federrath, 2021) or, when put into more general terms, depends on the boundary conditions. Krumholz (2014) provides a great overview about the "big problems in star formation" and highlights the IMF as one of its central challenges. Lee et al. (2020) provide a more recent review on the origin of the IMF.

In the following we do not attempt to present an overview about the whole range of IMF models but we choose a particular approach in order to better outline the most important aspects. Explaining the origin and universality of the IMF essentially needs to recover the following two properties. First, the scale-free power law tail for $M \gtrsim 1 \, \text{M}_\odot$. Second, the turnover around the peak mass at about $M_\text{c} \sim 0.2 \, \text{M}_\odot$. The former calls for scale-free physical processes whereas the latter explanation must somehow incorporate a characteristic mass scale.

Two prime candidates for scale-free processes, potentially responsible for the high mass power law tail of the IMF, are gravity and turbulence, which are both certainly at work in collapsing gas clouds. In a Newtonian framework gravity is scale-free because the force is proportional to the inverse square of the distance and

this holds for arbitrary distances. Turbulence is scale-free over some large inertial range, as discussed in chapter 4.

Gravitationally unstable molecular clouds

Interstellar turbulence is associated with density fluctuations on all scales which can create over-dense regions which collapse when their self-gravity exceeds a critical limit. Such a critical parameter can be obtained by investigating the equations for inviscid fluids under their own gravitational potential (see section 2.2.2) in order to obtain the dispersion relation. This approach goes back to Jeans (1902) and can be summarized as follows. For a uniform cloud with density, ρ, radius, R, sound speed, c_s, and some perturbation which affects the density field as $\rho(x,t) = \rho_0 + \rho_p \exp\left(i(kx - \omega t)\right)$, a linear stability analysis of the fluid equations with self-gravity leads to the following dispersion relation[2]

$$\omega^2 = c_s^2 k^2 - 4\pi G\rho. \tag{5.3}$$

Perturbations with wavenumber $k < \sqrt{4\pi G\rho}/c_s$ will be exponentially amplified, that is the cloud contracts due to its own gravity. The critical wavenumber can be equally expressed as a critical length scale,

$$\lambda_{\rm J} = \sqrt{\frac{\pi c_s^2}{G\rho}}, \tag{5.4}$$

which is the so-called Jeans length. The associated Jeans mass can be defined as

$$\begin{aligned} M_{\rm J} &= \frac{4\pi}{3}\rho \left(\frac{\lambda_{\rm J}}{2}\right)^3 \\ &= \frac{\pi^{\frac{5}{2}}}{6} \frac{c_s^3}{\sqrt{G^3 \rho}}, \end{aligned} \tag{5.5}$$

where it is common practice to use $\lambda_{\rm J}/2$ as radius for the spherical mass distribution but according to Girichidis et al. (2020) there is no fundamental justification which constrains the numerical factors in the Jeans mass to better than a factor of a few.[3] Assuming an ideal gas equation of state implies the sound speed is given by $c_s = \sqrt{k_B T/(\mu m_H)}$ and the Jeans mass then scales as

$$M_{\rm J} \propto T^{3/2} \rho^{-1/2}. \tag{5.6}$$

---

[2]The Jeans criterion is derived under some simplifying assumptions which we will not discuss here but simply refer to chapter five in Binney and Tremaine (2011).

[3]There is also an alternative derivation for a critical mass scale, the Bonnor-Ebert mass, which differs from the Jeans mass in its numerical factor. And in contrast to the Jeans mass the Bonnor-Ebert mass considers the external pressure. McKee and Ostriker (2007) provide a useful derivation. Apart from the choice of which critical mass scale to consider, there is another aspect which has the potential to be non-negligible even for order of magnitude calculations, namely the support from turbulent motions. The derivation for the Jeans mass here considers only the support from thermal pressure. Taking into account turbulence with supersonic motions adds another pressure which can be incorporated into equation (5.5) by redefining $c_s \rightarrow c_{\rm eff} = \sqrt{c_s^2 + \sigma^2/3}$ with velocity dispersion for the turbulent motion of the gas, σ, as discussed by Mac Low and Klessen (2004). Replacing c_s with $c_{\rm eff}$ in equation (5.5) yields $M_{\rm J,eff} \sim 200\,M_{\rm J}$ for supersonic turbulence in molecular clouds with $\sigma \sim 10 c_s$. Consequently, the effect of turbulent support against gravitational support is important to consider even for order of magnitude calculations about gravitational stability in supersonic molecular clouds.

It is useful to normalize the Jeans mass to typical values for molecular clouds[4] with $T \sim 10\,\mathrm{K}$ and $n \sim 1 \times 10^2\,\mathrm{cm}^{-3}$ with mean molecular weight, $\mu = 2.33$, for which we can express the Jeans mass as

$$M_\mathrm{J} \approx 29\,\mathrm{M}_\odot \left(\frac{T}{10\,\mathrm{K}}\right)^{3/2} \left(\frac{n}{100\,\mathrm{cm}^{-3}}\right)^{-1/2}. \tag{5.7}$$

If the total mass exceeds this limit the cloud is gravitationally unstable and will begin to collapse and become denser in the inner regions. The denser the cloud the lower the Jeans mass and thus the contracting cloud will soon contain more than one Jeans-unstable regions and the cloud will fragment.[5] This is a direct consequence of the Jeans Mass scaling according to equation (5.6) provided that the temperature remains constant because the cooling and heating rates balance each other. This scenario is referred to as isothermal collapse.

Relevance of turbulence for star formation

In chapter 4 we discuss the properties of interstellar turbulence in more detail. Here we summarize the main properties which are relevant for deriving the IMF within a model of *turbulent fragmentation*. Turbulence is essential for understanding star formation because stars form out of dense molecular gas clouds and the gas in their interior is not steady but in turbulent motion. Such molecular clouds are typically characterized by supersonic turbulence which effectively provides a pressure against suppression due to gravitational collapse of the cloud (Chevance et al., 2020). But turbulence can also act in favor of contraction. One mechanism is that turbulence increases collision rates and thereby enhances cooling via collisional excitation and subsequent photon emission which consequently reduces the thermal pressure. Another effect of compressible turbulence is that it creates density fluctuations above a critical threshold, which is the mechanism at the heart of the star formation model proposed by Hopkins (2013) which we discuss in the following. And because density fluctuations grow exponentially whereas velocities only grow linearly turbulence will always produce some regions which are unstable. In order to make quantitative statements about the relevance of turbulence for star formation it is useful to treat the density field statistically with a PDF.

Numerical simulations and observations (e.g., Sharda et al., 2022, and references therein) have established the prescription of a lognormal density PDF in turbulent star forming regions

$$P(s)\mathrm{d}s = \frac{1}{\sqrt{2\pi\sigma_s^2}} \exp\left(-\frac{(s-s_0)^2}{2\sigma_s^2}\right)\mathrm{d}s \tag{5.8}$$

where $s = \ln(\rho/\rho_0)$ with volume-averaged mean density ρ_0 and $s_0 = -\sigma_s^2/2$ due to conservation of mass (Krumholz, 2014). The width of this function, σ_s, generally increases with the Mach number, $\mathcal{M}$. The lognormal shape is well interpreted as a result of the central limit theorem because the density field results from a multitude

---

[4]According to Ferrière (2001) the typical densities in molecular clouds are $n \sim 10^2 - 10^6\,\mathrm{cm}^{-3}$ and $T \sim 10 - 20\,\mathrm{K}$ such that the Jeans mass derived in equation (5.7) represents an order of magnitude estimate for an upper limit for the (thermal) Jeans mass of molecular clouds.

[5]For an order of magnitude estimate the free-fall time $t_\mathrm{ff} \sim 1/\sqrt{G\rho}$ is suitable to approximate the time it takes for the gas cloud to collapse. Hence the denser regions collapse faster which is in support of the fragmentation process.

of random interactions (compression, shocks, rarefactions) which correspond to the multiplication of a large number of random factors.[6]

The velocity dispersion scaling discussed above for Kolmogorov turbulence is straight forward to generalize for other turbulent power spectra, which are given by $E(k) \sim k^{-n}$ (with $n = 5/3$ for Kolmogorov turbulence) via

$$\sigma_v^2(l) \sim \int_{2\pi/l}^{\infty} E(k)\mathrm{d}k \sim k^{-n+1} \sim l^{n-1}. \qquad (5.9)$$

Taking the square root yields

$$\sigma_v(l) \sim l^{(n-1)/2} \qquad (5.10)$$

which is known under the name of *linewidth-size relationship* because it corresponds to the observation that the linewidth of absorption or emission lines scale with the size of gas clouds in the interstellar medium (ISM).[7]

Furthermore interstellar turbulence is also important with respect to magnetic fields which are potentially relevant for star formation in many different ways. One effect is the additional magnetic pressure which together with thermal pressure opposes an inward acceleration of a magnetized gas cloud. Magnetic tension, meaning the resistance of magnetic field lines against deformation, is also important which depends on the geometry of the field lines and therefore also on the properties of the turbulent plasma. Magnetic fields around young stars are important drivers for jets and outflows. And turbulent compression can enhance ambipolar diffusion and consequently lower the magnetic pressure locally (Nakamura and Li, 2008). Furthermore, there are many possibilities for magnetic fields to influence star formation in more indirect ways and it is not yet clear to what extent magnetic fields actually influence which observable quantities of the star formation processes (Krumholz and Federrath, 2019).

In the following we discuss a star formation model introduced by Hopkins (2012) which builds on previous models (e.g., Padoan and Nordlund, 2002; Hennebelle and Chabrier, 2008) which aim at explaining the IMF via fragmentation in a turbulent medium. These models have a statistical approach to star formation theory in common because they all invoke a PDF for the density field which is connected to the properties of interstellar turbulence. Thus the scale-free nature of the IMF power law tail is inherited from the scale-free nature of turbulence and gravity. The characteristic mass scale, together with the lognormal-shaped turnover, is simply a result from the underlying density probability distribution function.

---

[6]Multiplying logarithmic quantities is equivalent to taking the logarithm of the sum of the quantities, that is $\ln(a)\ln(b) = \ln(a + b)$.

[7]Larson (1981) analyzed observational data of molecular clouds and found a power law relationship between the internal velocity dispersion and the cloud's size $\sigma \propto L^{\alpha}$ and mass $\sigma \propto M^{\beta}$. In Larson's original paper the best fit straight line through a cloud of data points was determined as $\alpha = 0.38$ and $\beta = 0.20$. The number of decimals in these results does not represent the actual uncertainty of this prescription as later studies have drawn different conclusions. Heyer et al. (2009) found the internal velocity dispersion to depend also on the density of the cloud as described by $\sigma \propto (\Sigma L)^{\alpha}$ with $\alpha = 0.5$ and surface density Σ. Ballesteros-Paredes et al. (2011) provide an overview of observational results at the time. Lately, Ballesteros-Paredes et al. (2018) found this relation to only hold for a limited dynamic range spanned by the column densities.

Turbulent fragmentation

Hopkins (2012, 2013) (hereafter H12 and H13) apply a methodology which goes back to Press and Schechter (1974) together with the so-called excursion set formalism. Here we outline only some essential aspects of the model in order to discuss their results.

The density field is described by a lognormal PDF, which is the imprint of turbulent compressions and rarefactions. In H13 a length scale dependent stability criterion is derived for a galactic disk and the density can be related to the largest Mach number in the galactic disk. In order to construct a statistical realization of the PDF one picks a random point in the galactic disk around which the gas density is smoothed within some arbitrary radius $R < h$. The mean density in this region, $\rho_0(R)$, can be compared to some critical density threshold, $B(R)$, which is defined below in equation (5.13), and takes into account contributions from galactic angular momentum, turbulence, thermal and magnetic support which dominate on different length scales. For a turbulent galactic disc, with scale height h, the critical density above which a region is self-gravitating is

$$\frac{\rho_{crit}}{\rho_0} = \frac{Q}{2\tilde{\kappa}} \left(1 + \frac{h}{R}\right) \left[\frac{\sigma_g^2(R)}{\sigma_g^2(h)} \frac{h}{R} + \tilde{\kappa}^2 \frac{R}{h}\right], \tag{5.11}$$

where the Toomre parameter, Q, and $\tilde{\kappa}$ are both numerical factors of order unity for marginally unstable galactic disks.[8] The dispersion is given by

$$\sigma_g^2(R) = c_s^2 + \langle v_t^2(R)\rangle + v_A^2 \tag{5.12}$$

where v_t is the turbulent velocity dispersion and v_A the Alfvén velocity. The *barrier* in this model is given by

$$B(R) = \ln\left(\frac{\rho_{crit}}{\rho_0}\right) + \frac{S(R)}{2} \tag{5.13}$$

where $S(R)$ is the variance in $\ln(\rho)$ averaged over a volume with radius R.[9] The model is best illustrated by considering figure 5.2.

H12 show that the resulting mass function can be approximated as

$$\frac{dN}{dM} \sim \frac{\rho_{crit}(M)}{\sqrt{2\pi S_0}} \left|\frac{d\ln\rho_{crit}}{d\ln M}\right| \exp\left[-\frac{(\ln[\rho_{crit}/\rho_0] + S_0/2)^2}{2S_0}\right] M^{-2}. \tag{5.14}$$

This lengthy expression can be further approximated for the low and high-mass range. For the high-mass range this allows to connect the exponent of the IMF power law index α (defined by equation (5.1)) to the spectral index of turbulence, n, as follows

$$\alpha \approx \frac{3(1 + n^{-1})}{2} + \frac{(3 - n)^2 \ln(M/M_0) - n\ln 2}{2S(M)n^2}. \tag{5.15}$$

---

[8]The Toomre parameter $Q \sim 1$ marks the critical point below which an axisymmetric gaseous disk becomes unstable to perturbations. H13 uses the following definitions: Toomre parameter $Q = (\sigma_g(h)\kappa)/(\pi G\Sigma_{\text{gas}})$, gas surface density Σ_{gas}, epicyclic frequency $\kappa = 2\Omega r_g^{-1}\mathrm{d}(r_g^2\Omega)/\mathrm{d}r_g$, orbital frequency $\Omega = v_c/r_g$, and $\tilde{\kappa} = \kappa/\Omega$. For constant circular velocity $v_c(r_g)$ it follows $\tilde{\kappa} = 2$.

[9]In H13 the variance in the logarithmic density is calculated from the following integral $S(R) = \int_0^\infty |\tilde{W}(k, R)|^2 \ln\left[1 + b^2 v_t^2(k)/(c_s^2 + \kappa^2 k^{-2})\right] \mathrm{d}\ln k$ with some suitable window function $\tilde{W}(k, R)$ and where $b \sim 1$ gives the fraction of the turbulent velocity in the compressive (longitudinal) motions.
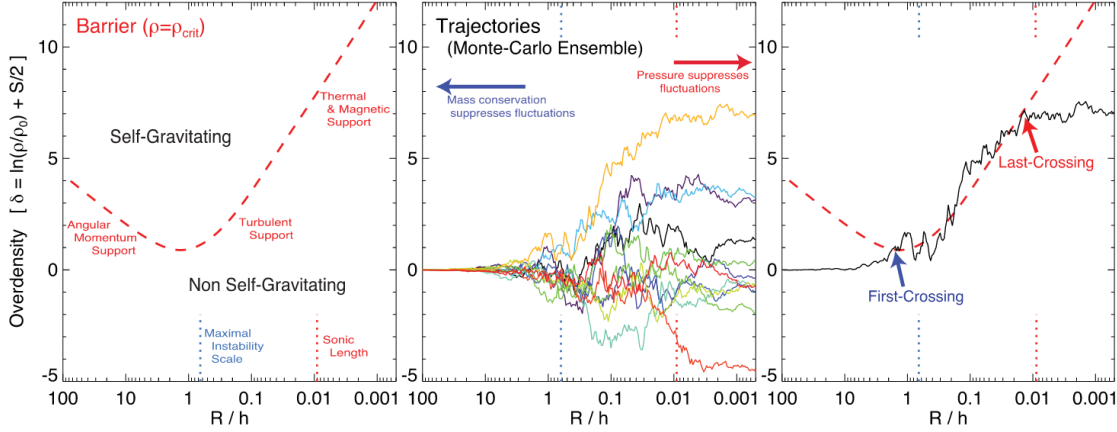
Figure 5.2: This figure from Hopkins (2013) nicely captures the essential features of the model. Left plot: the red dashed line marks the critical density, the barrier, $B(R)$, defined by equation (5.13), above which a region with radius R and density $\rho(R)$ becomes gravitationally unstable or self-gravitating. The sonic length corresponds to the length scale below which turbulent motions are subsonic. The sonic length is related to the turbulent power spectrum via the lindewidth-size relation in equation (5.10). Middle plot: each curve corresponds to a random realization of the density power spectrum at some random point in space and averaged with some window function within a radius R. Comparing these "trajectories" to the barrier (left plot) illustrates that most points are not self-gravitating. Right plot: this particular "trajectory", that is the mean density $\rho(R)$ in a volume with radius R around some point in space, is self-gravitating on multiple scales. The "first crossing" corresponds to the largest scale which is unstable and the "last crossing" to the smallest scale. The smaller the scales the larger the critical density and hence these scales will collapse faster because their free-fall time is shorter.

H12 find $\alpha \approx 2.2 - 2.4$ for typical initial conditions $M_0 \sim \rho_0 h^3 \sim 10^5 - 10^6 \, \mathrm{M}_\odot$ and turbulent power spectra in the range $n \in [5/3, 2]$ in good agreement with observations. The spectral index $n = 5/3$ corresponds to Kolmogorov turbulence and $n = 2$ to supersonic turbulence. The turnover at the lower masses occurs below the sonic length scale which corresponds to the following mass scale

$$M_{sonic} \approx \frac{2}{3} \frac{c_s^2 R_{sonic}}{G} \approx \mathrm{M}_\odot \left(\frac{c_s}{0.3 \, \mathrm{km \, s^{-1}}} \right)^2 \left(\frac{R_{sonic}}{0.1 \, \mathrm{pc}} \right) \tag{5.16}$$

and the overall shape appears to be in good agreement with observations as illustrated by figure 5.3.

In our discussion so far we have been somewhat imprecise when speaking about the mass function, $N(M)$, which in general may refer to different stages of the star formation process. Thus it is necessary to distinguish between the (prestellar) core mass function (CMF)[10] and the stellar initial mass function (IMF). Offner et al. (2014) offer a great overview about the various possibilities for the connection between CMF and IMF. Guszejnov and Hopkins (2015) derive both CMF and IMF from an analytic model in reasonable agreement with observations. If the CMF and

---

[10]The term "core" applies to many different kinds of dense gas clouds: starless cores (gravitationally bound or unbound), prestellar cores (starless and self-gravitating), protostellar cores (containing a protostar). Consequently cores are evolving and any CMF is always a composition of snapshots at a given evolutionary moment which is challenging to distinguish unambiguously. "Clump" is another frequently used terminology in the context of star formation which refers to large collections of gas which are likely to form a cluster of stars.
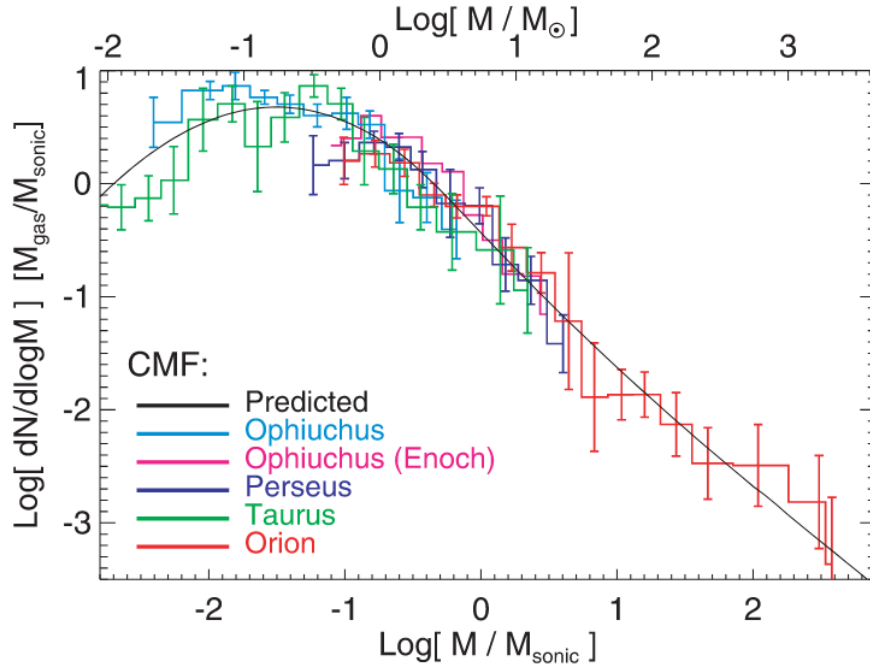
Figure 5.3: The core mass function (CMF) derived by the H12 model from the last crossing mass function (see figure 5.2) compared to observations of prestellar/starless CMFs in different regions. The modeled CMF corresponds to $\mathcal{M}_h = 30$, that is the Mach number for a region with size equal to the disc scale height, and $n = 2$, that is a steeper power spectrum as for Kolmogorov turbulence with $n = 5/3$ as discussed in chapter 4. Plot taken from Hopkins (2012).

IMF are self-similar to another then we would expect the evolutionary process from cores to stars to fulfill the following conditions:

- Cores must be gravitationally bound in order to produce stars;

- If cores accrete further mass, merge or fragment further, then this process has to occur in a self-similar way;

- Star formation efficiency (fraction of gas converted to stars) must be comparable for cores with different masses;

- Timescale on which stars are formed must be comparable for cores with different masses.

There are some hints for a direct correspondence (e.g., self-similar mapping) between the two quantities but there is also still considerable uncertainty with respect to observations (Lee et al., 2020).

In summary, the star formation model presented by H12 and H13 derives a core mass function (CMF) which recovers both the high-mass power law tail and the lognormal shaped turnover for the low mass range of the stellar initial mass function (IMF). The universal power law with $\alpha \sim 2.3$ can be understood as resulting from the omnipresence of turbulence in the star forming environments and the relatively weak dependence on the exact value for the spectral index of the turbulent power spectrum. The characteristic mass scale M_c together with a lognormal-shaped turnover for the lower mass range results from the characteristic scales that enter the model as initial and boundary conditions. These conditions are, the Mach number

at disc scale height, the speed of sound and the mean density, which are all connected to each other and therefore closely tied to certain values. However, the model is fairly complicated and involves many assumptions and approximations which can be questioned. At the same time there are certainly many important details which are not covered and the model cannot provide a physically accurate description of the star formation process which is simply too complex to model adequately in all details. Hence, in the following, we aim at taking an even more granular view on the origin of the observed mass functions. In doing so, we deliberately neglect basically all the physics and consider a very general and simple procedure which leads to mass functions with a power law exponent $\alpha \sim 2$.

Is there a universal mass function?

Having discussed the origin of the mass functions for stars and prestellar cores it is interesting to take a broader look and compare it to mass functions for other objects in our universe. Such an investigation naturally includes a large amount of uncertainty due to observational biases, like for example given an incomplete sample where larger masses are detected more frequently than lower masses. Comparing different mass functions also requires to choose a certain normalization which needs to be estimated when the data is incomplete and the total mass of all objects is unsure. Keeping this in mind, it is however surprising that the overall shape, that is the power law index of the mass function, appears to be $\alpha \sim 2$ for all sorts of different objects. Figure 5.4 shows the mass functions of objects as small as asteroids and planets all the way to galaxies and galaxy clusters and thereby spanning a range of more than thirty orders of magnitude in mass.

Evidently these objects are quite different to each other and are nevertheless all characterized by a similar mass spectrum. Therefore we are interested in finding universal mechanisms which do not depend on the specific details of the system and reproduce the observed scaling. In section 2.3 we demonstrate how the $\alpha = 2$ scaling emerges from two very simple toy models for fragmentation.[11] Because these toy models are invariant under time reversal they can equally well represent a model for a self-similar merging process in the context of galaxy and galaxy cluster formation. Consequently, $\alpha = 2$ can be understood as a result from self-similar fragmentation or merging processes.

This particular mass function scaling is also special in the sense that it guarantees an equal amount of mass per logarithmic mass interval, $\mathrm{d}\ln(M)$, as can be demonstrated simply by

$$\Delta M = \int_{M_0}^{M_1} N(M)\mathrm{d}M = C\ln(M_1/M_0), \qquad (5.17)$$

with constant C. Evidently ΔM depends only on the ratio M_1/M_0, which implies that it is constant for any logarithmic mass bin because $M_1/M_0 = 10$. This "equal mass per logarithmic mass bin" property holds only for $N(M) \sim M^{-1}$ (or equivalently $\mathrm{d}N(M)/\mathrm{d}M \sim M^{-2}$, that is $\alpha = 2$), whereas exponents larger or smaller

---

[11]Another interesting toy model was presented by Elmegreen (1997) who derives the IMF via random sampling from a turbulent fractal cloud.
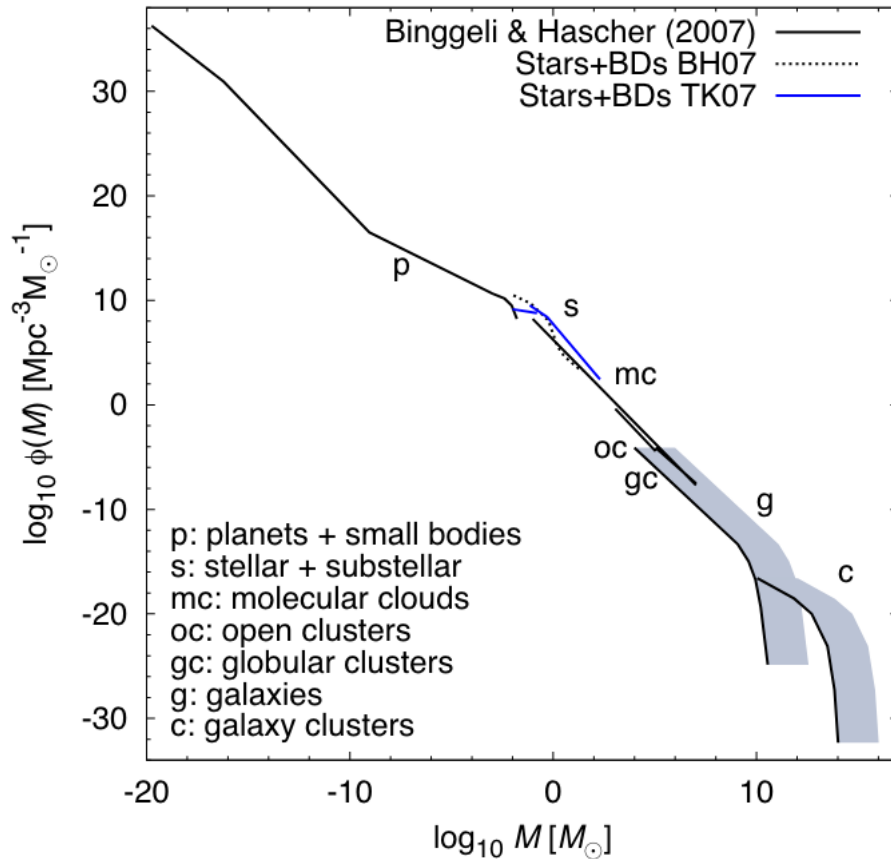
Figure 5.4: Here we show a plot which hints on the existence of a *universal mass function* which spans more than thirty orders of magnitude in mass and contains objects from asteroids up to galaxy clusters. The overall normalization for the respective mass functions was estimated by Binggeli and Hascher (2007) from the observed abundance of the objects. For galaxies (g) and galaxy clusters (c) the lower black line corresponds to the baryonic mass only and the upper end of the shaded region to baryonic mass + dark matter. Plot taken from Kroupa et al. (2013).

would lead to a ΔM which depends on the given mass scale.[12] The scale-free nature of this particular scaling thus goes beyond the generic scale invariance intrinsic to all power laws as discussed in section 2.1.

However, speculations about the existence of a *universal mass function* (Tutukov and Shustov, 2020; Shustov and Tutukov, 2018; Binggeli and Hascher, 2007) should be taken with a grain of salt because the similar scaling holds only very roughly. For

---

[12]The observed $N(M) \sim M^{-1}$ scaling is a solution for the differential equation $\frac{\mathrm{d}N}{N} = -\frac{\mathrm{d}M}{M}$ which illustrates the structural similarity of the number of objects N to their masses M. It is straightforward to verify as follows

$$\int \frac{\mathrm{d}N}{N} = \int -\frac{\mathrm{d}M}{M}$$
$$\ln(N) + C_1 = -\ln(M) + C_2$$
$$\ln(NM) = C_2 - C_1$$
$$NM = \exp(C_2 - C_1) \equiv C$$
$$N = CM^{-1}.$$

example Davidzon et al. (2017) find $\alpha \approx 1.5$ for low redshift galaxies whereas some type of higher redshift galaxies are better fit by a double Schechter function which contains two power law indices. These deviations from $\alpha = 2$ could be interpreted as the presence of physical processes which are characteristic to the respective system (planets, stars, galaxies, etc.) whereas all these systems are characterized by a sort of baseline mass function which is due to some very general mechanisms like fragmentation or merging as illustrated by the toy models. Shustov and Tutukov (2018) follow a similar line of thought and take the $\alpha = 2$ as the "basic spectrum" which results from the random character of the underlying processes whereas the deviations are interpreted as imprints of "specific physical processes" like galactic or stellar winds for example.

5.2 Star Formation Law

5.2.1 Observations

Apart from the initial mass function (IMF) there is another important quantity in the context of star formation, that is the star formation rate (SFR), which represents the amount of gas converted into stars per unit of time. The SFR is essential because it is closely tied to the evolution of the galaxy itself and the coupling is in both ways and over a large range of spatial scales because the large-scale evolution of a galaxy affects the SFR and the SFR affects the large-scale evolution of the galaxy. Stars are energy "sources" for the ISM because they convert nuclear binding energy into radiation and into particle motion as stellar wind or in supernova explosions for example. In consequence stars are responsible for accelerating cosmic rays (see chapter 3) and driving the turbulent motion of interstellar gas (see chapter 4 on interstellar turbulence). Hence the SFR is an essential quantity not only to study star formation but also to better understand the galaxy at large.

The SFR is commonly given as a surface density Σ_{SFR}. In disk galaxies the *surface* density for gas, Σ_{gas}, typically refers to averaging the volume density, ρ, as $\Sigma_{\text{gas}} = \int_{-\infty}^{\infty} \rho \mathrm{d}z$, where z is the coordinate perpendicular to the galactic disk. An analogous averaging procedure can be done for the three dimensional SFR density to obtain Σ_{SFR} in units of $[\Sigma_{\text{SFR}}] = \mathrm{M}_{\odot}\mathrm{yr}^{-1}\mathrm{pc}^{-2}$. Hence Σ_{SFR} describes the rate at which some galactic environment converts gas into stars.

Although star formation certainly presents a complex multi-scale problem with many parameters that could potentially matter, observations reveal a simple power law which connects the SFR surface density to the gas surface density as follows

$$\Sigma_{\text{SFR}} \sim \Sigma_{\text{gas}}^{n}. \tag{5.18}$$

It is known as *star formation law* or *Kennicutt-Schmidt law* because it goes back to Schmidt (1959) and Kennicutt (1998). The value of the power law index n does not appear to be universal but rather varying between $n \sim 1-2$ for different kind of galaxies and environments (e.g., Whitworth et al., 2022; Girichidis et al., 2020) but at least for "normal" and nearby spiral galaxies it appears to be fairly well constrained to $n \approx 1.4$ according to a recent study by de los Reyes and Kennicutt (2019) which is shown in figure 5.5.
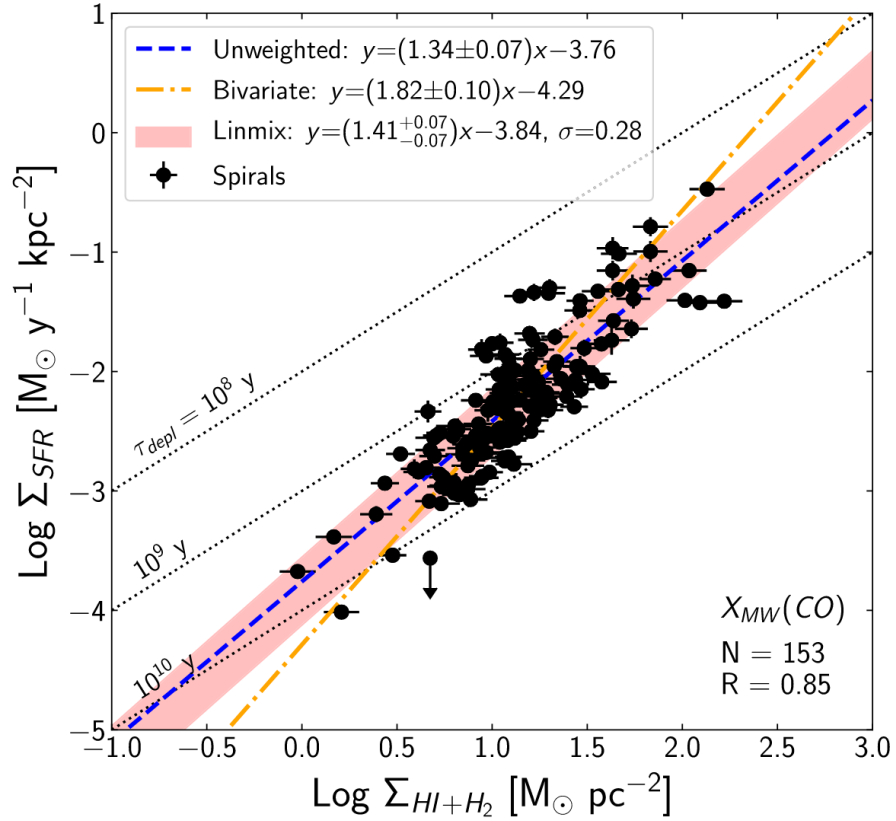
Figure 5.5: This plot is taken from de los Reyes and Kennicutt (2019) and shows the star formation law observed for 153 nearby spiral galaxies. The dashed lines represent constant depletion times $\tau_{\mathrm{dep}} = \Sigma_{\mathrm{gas}}/\Sigma_{\mathrm{SFR}}$. They used three different fitting techniques and determined $n = 1.41$ with a dispersion of 0.28 as best fit to their data. More details on the methodology and uncertainties are found in their paper.

5.2.2 Discussion

There is an ongoing debate about the star formation law with respect to questions like the following: Considering figure 5.6, does the SFR correlate with the density of atomic hydrogen (HI), molecular hydrogen (H_2) or with the sum of both (de los Reyes and Kennicutt, 2019)? How does the correlation change for low metallicity and high redshift galaxies (Whitworth et al., 2022)? What is *local* version of the star formation law, that is not averaged over the entire galaxy but holds sub-kpc scales (Bigiel et al., 2008)?

In the following we do not aim to answer these questions but focus on the star formation law on global scales for galaxies like our own Milky Way and with respect to the total gas density. Given the power law index $n \sim 1.4$ for the star formation law in equation (5.18) we would naturally like to understand its origin. We would expect $n = 1.5$ if stars form out of collapsing gas clouds on a free-fall time because $\tau_{\mathrm{ff}} \sim \rho^{-1/2}$. Under the premise that star formation itself is directly proportional to the density of available gas and given that we can take $\Sigma_{\mathrm{gas}} \sim \rho_{\mathrm{gas}}$ the star formation *rate* should then scale as $\Sigma_{\mathrm{SFR}} \sim \Sigma_{\mathrm{gas}}/\tau_{\mathrm{ff}} \sim \Sigma_{\mathrm{gas}}^{1.5}$. However, the observed SFR is about two orders of magnitude lower than expected if stars were produced simply by gas clouds in free-fall collapse. If all molecular clouds in the Milky Way were in free-fall collapse we would expect an integrated SFR of $\sim 300\,\mathrm{M_\odot yr^{-1}}$ (Evans II et al., 2021) which is more than a factor of hundred times larger than the observed
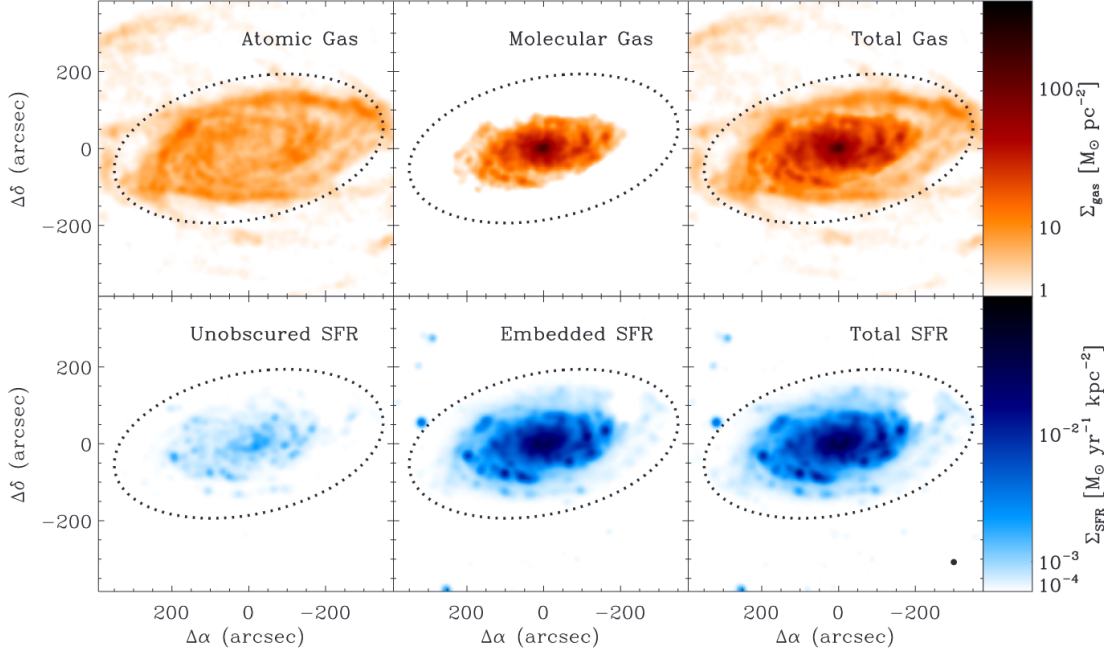
Figure 5.6: This plot compares the distribution of gas (upper panel) to the star formation rate SFR for the nearby galaxy NGC 5055. Apparently the correlation between molecular gas density and SFR surface density than between atomic gas density and Σ_{gas}. However, there is some considerable uncertainty in the data because of the observational methods. The density of H_2 is derived from the CO line emission intensity and the conversion factor carries a significant uncertainty (de los Reyes and Kennicutt, 2019). The SFR surface density is determined directly from the UV-emission of young massive stars and indirectly via the infrared emission caused by heated dust presumably by the UV radiation of massive young stars. The figure was published by Leroy et al. (2008).

value of $\sim 2\,\text{M}_\odot\text{yr}^{-1}$ (Chomiuk and Povich, 2011). The discrepancy between these two values can be captured by introducing a dimensionless parameter $\epsilon \sim 0.01$.[13] There are two opposing scenarios on how to interpret the low value of ϵ.

Either star formation is "slow but efficient" or it is "fast but inefficient" (Kruijssen et al., 2019). A third option is a mix of the two scenarios, that is "slow and inefficient", as presented by Evans et al. (2022) who connect the efficiency to the virial parameter of the star forming region in order to explain the varying but generally low efficiency of star formation. The difficulty in determining the physical mechanisms setting ϵ is one of the three "big problems in star formation" (Krumholz, 2014).[14]

Krumholz et al. (2012) present a version of a *local* star formation law which reduces the observed scatter in the star formation law by introducing the free-fall time into the star formation law as follows

$$\Sigma_{\text{SFR}} \sim \frac{\Sigma_{\text{gas}}^n}{\tau_{\text{ff}}}. \tag{5.19}$$

---

[13]The parameter ϵ can be interpreted in different ways. A frequently seen choice is to define it via the ratio of free-fall time to depletion time $\epsilon = \tau_{\text{ff}}/\tau_{\text{dep}}$ (e.g., Krumholz, 2014).

[14]The other two big problems in star formation are understanding stellar clustering and the origin of the stellar initial mass function.

They interpret this surface density star formation law as a result of an underlying *volumetric* star formation law which can be written in our notation as

$$\rho_{\rm SFR} \sim \frac{\rho}{\tau_{\rm ff}} \sim \rho^{3/2}. \tag{5.20}$$

They find that this local volumetric star formation law holds both for data from the Milky Way and nearby galaxies. Apparently, large-scale galactic properties (e.g., orbital period) affect the SFR only indirectly via their influence on the gas density.[15] Bacchini et al. (2019) find evidence for the volumetric star formation law $\rho_{\rm SFR} \sim \rho^2$ to hold in the Milky Way and in nearby star-forming galaxies.

Since observations are typically constrained to quantities that are averaged over the line of sight, there are large uncertainties involved and it is challenging to decide whether the volumetric or surface density star formation law provides the tighter relationship. According to de los Reyes and Kennicutt (2019): "the physics behind the star formation law remain unclear". However, in combination with other observed power laws, the star formation law certainly provides a useful tool to investigate the interconnections within a galaxy.

5.3 Far-infrared–radio correlation

5.3.1 Observations

The far-infrared – radio correlation (FRC) is a fairly tight power law relationship which connects the luminosity of two very distinct ranges of the electromagnetic spectrum. The correlation has been observed both globally (scales of tens of kiloparsec) for entire galaxies (e.g., de Jong et al., 1985; Helou et al., 1985; Niklas, 1997; Yun et al., 2001; Tabatabaei et al., 2017; Heesen et al., 2022) and locally (sub-kiloparsec scales) within galaxies (e.g., Boulanger and Perault, 1988; Murphy et al., 2006; Paladino et al., 2006; Dumas et al., 2011; Heesen et al., 2014).

Figure 5.7 compares the far-infrared luminosity at $60\,\mu m$ to the radio luminosity at $1.4\,{\rm GHz}$ in two plots which were published by Yun et al. (2001). Their study contains 1809 galaxies with redshift $z < 0.15$ and they claim to provide a representative sample for the population of "late type field galaxies in the local volume". The correlation has a relatively low scatter over about five orders of magnitude for the given data and the authors infer a linear correlation between the radio and far-infrared luminosities.

We can write down the FRC via the radio luminosity $L_{\rm rad}$ and the far-infrared luminosity $L_{\rm FIR}$ as

$$L_{\rm rad} \sim L_{\rm FIR}^b \tag{5.21}$$

where $b < 1$, $b = 1$, and $b > 1$, correspond to a sub-linear, linear or super-linear correlation respectively. The linearity or non-linearity of the FRC is still a matter of debate (e.g., Heesen et al., 2022, and references therein) due to methodological and observational uncertainties and the choice of wavelengths considered for both radio and far-infrared emission. Furthermore, in general the relationship may change for different types of galaxies (e.g., Schober et al., 2016; Petter et al., 2020; Delvecchio

---

[15]For galaxies with surface densities a lot higher than in the Milky Way Krumholz et al. (2012) expect deviations from the local volumetric star formation law.
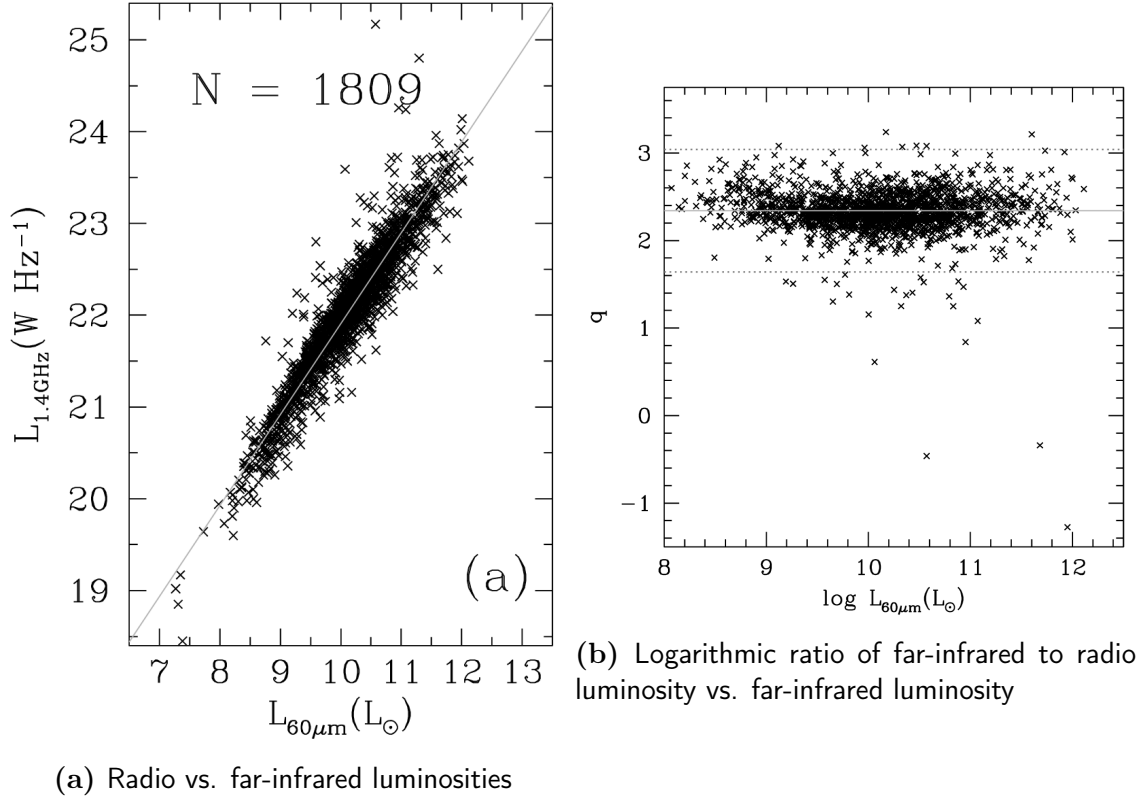
(a) Radio vs. far-infrared luminosities

(b) Logarithmic ratio of far-infrared to radio luminosity vs. far-infrared luminosity

Figure 5.7: The far-infrared –radio correlation (FRC) spans about five orders of magnitude in luminosity when plotting the radio luminosity at $1.4\,\mathrm{GHz}$ against the far-infrared luminosity at $60\,\mu\mathrm{m}$ (left). Introducing the q-parameter as a measure of the logarithmic ratio of the two luminosities allows to visualize the relatively low scatter of the correlation (right). The infrared data stems from 1809 galaxies observed in infrared with the Infrared Astronomical Satelite (IRAS) and the radio data from the NVSS catalog. Both plots taken from Yun et al. (2001).

et al., 2021). However, the correlation appears to hold for a broad variety of galaxies. Tabatabaei et al. (2017) investigate radio emission in the range of $1 - 10$ GHz and infrared emission in the range $8 - 1000$ μm for 61 nearby galaxies with various morphologies. They find indications for a nonlinear FRC from a declining value of q which is the logarithmic ratio of the two luminosities. They consider to different definitions for q, where they use either total infrared emission (TIR) or the far-infrared emission (FIR) in the range $42 - 122$ μ only. Their conclusion implies $b > 1$, however they do not infer an explicit value for b. For a sample of 74 nearby galaxies Niklas (1997) find $b = 1.25 \pm 0.08$ for non-thermal radio emissions at $10.8\,\mathrm{GHz}$ and $1.4\,\mathrm{GHz}$ frequencies. For a sample of 76 nearby galaxies Heesen et al. (2022) infer $b = 1.34 \pm 0.06$ at $144\,\mathrm{MHz}$, $b = 1.16 \pm 0.06$ at $1.4\,\mathrm{GHz}$, and $b = 1.08 \pm 0.06$ at $5\,\mathrm{GHz}$.

5.3.2   Discussion

There is little doubt that star formation is a common cause for the radio and infrared emissions that is to some extent responsible for the observed FRC. In star forming environments the more massive stars emit a lot of high-energy UV-photons which heat up the surrounding dust and make it re-radiate this energy in the infrared. Hence a correlation between the SFR and infrared luminosities is plausible. On the other hand star forming regions host SNRs where cosmic rays can be accelerated
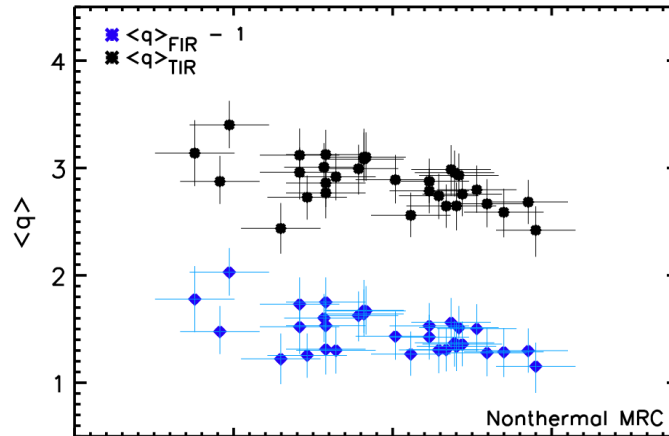
Figure 5.8: The q-parameter here is defined as the logarithmic ratio of luminosities in non-thermal mid-radio-continuum emission (MRC) and far-infrared (FIR, blue points) and total infrared (TIR, black points). The decreasing trend hints on a super-linear FRC. Plot taken from figure 9 in Tabatabaei et al. (2017).

(see section 3.2). These cosmic rays (CRs) are exposed to Lorentz forces in the omnipresent interstellar magnetic field (see section 4.3) and, due to their low mass to charge ratio (compared to protons or heavier nuclei) CR electrons are significantly affected by loosing energy via synchrotron radiation. Typically this occurs in GHz frequencies, meaning radio waves of a few tens of centimeters. Hence, this type of non-thermal radio emission depends on the product of at least two factors: first, the CR energy density, and second, the magnetic field strength. Provided that both quantities are correlated accordingly with star formation activity, and ignoring other contributions to radio and infrared emission, then this reasoning would be in agreement with the observed FRC.

However, it requires further clarification why the correlation is so tight and apparently insensitive to variations of specific properties of the observed galaxies. We are thus interested in finding an explanation which holds for a broad range of environments. Schleicher and Beck (2013) propose a model which explains the FRC by relating the SFR and the magnetic field strength via turbulent magnetic field amplification. Their model can be evaluated for disk galaxies with arbitrary redshifts and being interested in cases like our own galaxy we consider the case where $z = 0$ which allows to simplify their equations and outline the power laws connecting magnetic fields, gas surface density, and SFR surface density, such that the observed FRC is reproduced.

In this model we characterize disk galaxies with a certain average and constant volume density, ρ, and a constant ratio of disk scale height to galactic radius, $h/R \sim$ const, such that ignoring constant factors allows to express the scaling of the total gas mass with radius as $M \sim R^3$ or equivalently

$$R \sim M^{1/3}. \tag{5.22}$$

The gas surface density $\Sigma_{\text{gas}} \sim h\rho \sim R$ and consequently

$$M \sim \Sigma_{\text{gas}}^3. \tag{5.23}$$

Using the star formation law (5.18) it follows

$$M \sim \Sigma_{\text{SFR}}^{3/n}. \tag{5.24}$$

If interstellar turbulence is mainly driven by SNe we can write for the energy injection rate

$$\Gamma_{\text{inj}} \sim \Sigma_{\text{SFR}} \sim M^{n/3} \tag{5.25}$$

and provided that turbulence is in a stationary state (i.e., the energy injection rate equals the dissipation rate corresponding to a constant flux of energy via a cascade of turbulent kinetic energy as discussed in section 4.2), we have

$$\Gamma_{\text{diss}} = \epsilon \sim \frac{\Sigma \sigma^2}{\tau_h} \tag{5.26}$$

with σ being the gas velocity dispersion on scales of the disk scale height h and $\tau_h \sim h/\sigma$ being the eddy turnover time (see section 4.2). Solving for the velocity dispersion yields

$$\sigma \sim M^{n/9}. \tag{5.27}$$

For $\tau_h \ll \tau_{\text{galaxy age}}$ there is enough time for magnetic field amplification via the small scale dynamo (see section 4.3) such that equipartition can be reached for the magnetic and turbulent energy densities.[16] With turbulent kinetic energy density $\sim \rho \sigma^2$ the equipartition condition gives

$$B^2 \sim \rho \sigma^2 \tag{5.28}$$

which implies for constant ρ that the magnetic field strength follows the same scaling with mass as the velocity dispersion

$$B \sim M^{n/9}. \tag{5.29}$$

Using equation (5.23) and equation (5.24) we obtain

$$B \sim \Sigma_{\text{gas}}^{n/3} \tag{5.30}$$

and

$$B \sim \Sigma_{\text{SFR}}^{1/3}. \tag{5.31}$$

For the star formation law index $n = 1.4$ we obtain $B \sim \Sigma_{\text{gas}}^{0.47}$. These two power laws for the magnetic field, scaling with gas density and star formation rate surface density, are in reasonable agreement with results by other studies (e.g. Niklas and Beck, 1997; Heesen et al., 2014; Basu et al., 2017). Via direct numerical simulations of a supernova driven galactic dynamo, Gressel et al. (2008) discover a closely related correlation between the ratio of regular to turbulent magnetic field $B_{\text{turb}}/B_{\text{reg}} \propto$ SFR$^{0.38}$ and the star formation rate (not density), as long as the supernova rate and the SFR are proportional to another. We discuss interstellar turbulence in chapter 4 and magnetic field amplification in section 4.3.

Furthermore, in case of equipartition between the energy densities of CRs and magnetic fields the synchrotron luminosity is related to the magnetic field strength via

$$L_{\text{sync}} \sim B^{3+\alpha_{\text{sync}}} \tag{5.32}$$

---

[16]For an order of magnitude estimate for spiral galaxies we can take $\sigma \sim 10\,\text{km}\,\text{s}^{-1}$ (e.g., Mogotsi et al., 2016) and $h \sim 100\text{pc}$ and find $\tau_h \sim 10\,\text{Myr}$ which is certainly a lot smaller than $\tau_{\text{galaxy age}} \sim$ Gyr.

with synchrotron spectral index α_{sync} defined via the synchrotron flux density $S_\nu \sim \nu^{-\alpha_{\mathrm{sync}}}$ at frequency ν and related to the spectral index of the CR electron flux $N \sim E^{-p}$, with $p = 2\alpha_{\mathrm{sync}} + 1$. Using equation (5.31) thus yields

$$L_{\mathrm{sync}} \sim \Sigma_{\mathrm{SFR}}^{1+\alpha_{\mathrm{sync}}/3}. \qquad (5.33)$$

Provided that $L_{\mathrm{FIR}} \sim \Sigma_{\mathrm{SFR}}$, and the reasonable assumption for nearby galaxies (discussed in section 3.1 in Schleicher and Beck, 2013) that the radio emission L_{rad} is dominated by the synchrotron emission, L_{sync}, we can infer $b = 1 + \alpha_{\mathrm{sync}}/3$ for the FRC (5.21). Hence, for $\alpha_{\mathrm{sync}} > 0$ we obtain a super-linear FRC where the scaling is determined by the synchrotron spectral index α_{sync}.

For the given sample of nearby galaxies and the frequency range of $1 - 10$ GHz Tabatabaei et al. (2017) determined a non-thermal (contributions from thermal radio emissions were subtracted) spectral index $\alpha_{\mathrm{nt}} = 0.97 \pm 0.16$ which upon identification with α_{sync} corresponds to $b \approx 1.32$.

Apparently the power laws derived from this simple model are in good agreement with observations which provides evidence for the equipartition between magnetic field, cosmic ray and turbulent energy densities.[17]

However, a serious shortcoming of the proposed model is that it can only account for the global FRC because it involves only quantities averaged over the entire galaxy on tens of kiloparsec. A closer investigation would be required to understand the mechanisms at work on sub-kiloparsec scales responsible for the local observations of the FRC. There are also other proposed explanations for understanding the origin of the FRC (e.g. Voelk, 1989; Niklas and Beck, 1997; Bell, 2003; Lacki et al., 2010) and it remains an open issue which model comes closest to the physical reality.

---

[17]Not all observations agree with the scalings derived here. For example Tabatabaei et al. (2013) provide a detailed investigation of a nearby spiral galaxy and recover a correlation between B–Σ_{SFR} and B–Σ_{gas} however their power law indices are about half the value we derived here.

Chapter 6

Conclusion

Understanding the processes in our galaxy which give rise to the observed power laws is challenging because of the interconnectivity of all components. Figure 6.1 provides a schematic illustration of the various couplings in the galaxy which are characterized by the given power laws. In this galaxy model we consider star formation as the dominant power source which distributes energy between thermal gas, turbulent gas, cosmic rays and magnetic fields, such that an order of magnitude equipartition in energy densities is reached with $\mathcal{E} \sim 10^{-12}\,\mathrm{erg/cm^3}$. The comparable magnitude of energy densities provides yet another challenge because all components have the potential to provide feedback which changes the conditions for the evolution of the other components and the entire galaxy.

Star formation takes a central role because it converts gravitational and nuclear binding energy from small scales into radiation, magnetic energy, and kinetic energy (heat, turbulence, neutrinos, cosmic rays) which are now acting on large scales. On galactic average most of the power is carried by electromagnetic radiation which ultimately leaves the galaxy without significant losses. The fraction which becomes converted into kinetic energy, cosmic rays and magnetic fields can be further transported and interchanged between these components. Of particular importance are core collapse supernovae which is the outcome of only a small fraction of all stars which have sufficient mass. The number of stars per interval in mass is accounted for by the initial mass function, $\mathcal{N}_\star \sim M^{-2.35}$, with the power law shape valid for masses in the range of roughly one to a hundred solar masses. The steepness of this slope sets the relative amount of core collapse supernovae and therefore determines their galactic average power contribution. The origin and universality of the initial mass function can be interpreted as resulting from the density and turbulence properties of the interstellar gas out of which stars form. Turbulence increases the pressure support of gas clouds which opposes their self-gravity and thereby acts against star formation on small scales (interior of gas clouds). On the other hand, turbulence also creates over-densities which become gravitationally unstable and thereby turbulence promotes star formation on larger scales (exterior of gas clouds).

Interstellar turbulence can be traced via electron density fluctuations, for which the power spectrum became known as the Big Power Law in the Sky, characterized by $E_{\mathrm{turb}} \sim k^{-5/3}$, in agreement with Kolmogorov's hydrodynamical model for homogeneous, isotropic and stationary turbulence. Supernovae provide sufficient power in order to maintain interstellar turbulence at the observed levels and the square of the turbulent velocity (e.g., velocity dispersion of the gas) tends to correlate with the star formation rate, $v^2 \propto \mathrm{SFR}$. This observation agrees with the scenario of supernovae
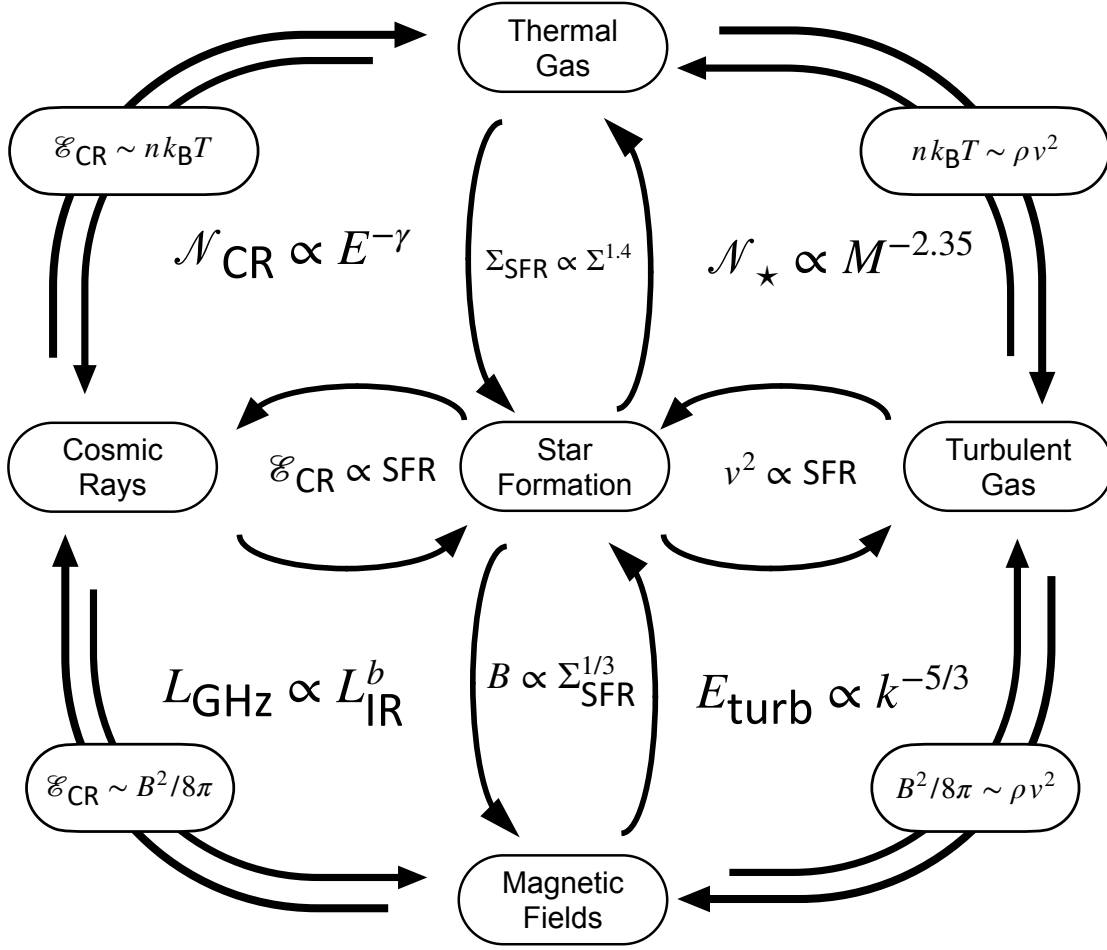
Figure 6.1: Schematic illustration of our interconnected galaxy model where the interactions between the five major components are characterized by power law relationships. Star formation continuously provides power which can be distributed among all components which ultimately leads to an order of magnitude equipartition of thermal pressure, $1.5nk_{\rm B}T$, turbulent pressure, $0.5\rho v^2$, magnetic field energy density, $B^2/8\pi$, and cosmic ray energy density, $\mathcal{E}_{\rm CR} = \int E \mathcal{N}_{\rm CR} {\rm d}E$.

being the main driver behind turbulence provided that the initial mass function is universal such that the average frequency of supernovae is directly proportional to the star formation rate. However, other drivers may contribute additionally at an extent which depends on the length scales under consideration and the location within the galaxy. The physical mechanisms responsible for dissipating the turbulent energy cannot be meaningfully discussed within a purely hydrodynamical framework because the dissipation scale appears to be a lot smaller than the mean free path of the particles. This suggests the significance of magneto-hydrodynamical waves for the dissipation of energy on the small scales and multiple potential mechanisms exist which depend on the local properties of the plasma. Interstellar turbulence also transfers kinetic energy into magnetic energy via the turbulent dynamo which is a reasonable explanation for the observed energy equipartition.

Magnetic fields are omnipresent in the interstellar medium and essential for understanding processes like dissipation of turbulence, cosmic ray acceleration and confinement. The origin of the far-infrared–radio correlation, $L_{\mathrm{GHz}} \propto L_{\mathrm{IR}}^{b}$, can be traced back to star formation being a common cause for both the radio and the infrared luminosity. However, the tightness of the relationship is surprising because of the multitude of physical processes that could potentially affect the correlation. It can be interpreted as a result of turbulent magnetic field amplification where $B \propto \Sigma_{\mathrm{SFR}}^{1/3}$. The power law exponent, b, is inferred from the spectral index of the cosmic ray electrons which are held responsible for contributing the dominant fraction of L_{GHz} via synchrotron emission. A charged particle in perpendicular motion to a magnetic field experiences the Lorentz force and therefore magnetic fields are essential for understanding the acceleration and propagation of charges in the interstellar medium.

Cosmic rays are characterized by power law energy spectra over ten orders of magnitude. The differential number density spectrum, $\mathcal{N}_{\mathrm{CR}} \propto E^{-\gamma}$, carries information about the origin and transport of cosmic rays. For the atomic nuclei among the cosmic rays two different universality classes can be identified which are characterized by $\gamma = 2.7$ for primary and $\gamma = 3.0$ for secondary cosmic rays. The difference in spectral index can be understood as an imprint of their different origin and propagation histories. We provide a novel interpretation by applying a nonequilibrium statistical model, which is called superstatistics, to the AMS data for primary (He, C, O) and secondary (Li, Be, B) cosmic rays and connect the spectral index to some effective degrees of freedom of the underlying temperature fluctuations. The model fits well to the data, however, both interpretation and methodology are discussed critically. The open questions about cosmic ray acceleration and propagation cannot be answered satisfactorily within the superstatistical model. The characteristic temperature scale, $T \sim 200\,\mathrm{MeV}$, in the superstatistical model exceeds the thermal energies of even the hottest interstellar gas by many orders of magnitude. The argument that young neutron stars would provide sufficiently high temperatures is not conclusive. Nevertheless, the energy *densities* of cosmic rays and warm interstellar medium are roughly comparable within an order of magnitude, $\mathcal{E}_{\mathrm{CR}} \sim 1.5 n k_{\mathrm{B}} T$.

Thermal gas in the interstellar medium exists in multiple phases and the warm medium is too hot to form stars. Star formation occurs only in environments where the gas is sufficiently cool and dense. The rate at which gas is turned into stellar mass, can be expressed as a star formation rate surface density which correlates with the gas surface density as $\Sigma_{\mathrm{SFR}} \propto \Sigma^{1.4}$. It is plausible that star formation is enhanced by higher gas surface densities but the physical reasons for the given power law exponent are still uncertain. Additionally, high star formation rates provide feedback that drive interstellar turbulence, heat and disperse the surrounding gas, and thereby reduce the star formation rate for the subsequent epoch. This provides a self-regulation mechanism for star formation which could be to some extent responsible for the observed overall low efficiency by which gas is turned into stars.

Apparently our galaxy is a highly organized system which is certainly not in a static equilibrium but could be rather characterized by a *dynamical* equilibrium. The energy released from star formation flows through the system in such a way that the energy densities are brought roughly into equipartition. Future work could build upon the outlined galaxy model in multiple ways. It would be interesting to create a numerical implementation where the individual components are coupled in such a way that the given power law relationships and equipartition conditions are

valid. This could enable to investigate the stability properties of the system and its sensitivity to changes in the power law exponents. Additionally, the model could be expanded to include other important properties of the galaxy as for example the gravitational energy. More generally the openness of the system should be included because in reality a galaxy is embedded in an environment with which it interacts and exchanges mass and energy. Not only electromagnetic radiation but also cosmic rays, gas and dust can leave the galactic disk, propagate through the galactic halo or even reach out the intergalactic medium. Furthermore, gas accretion onto the galactic disk is relevant for both star formation and interstellar turbulence.

In summary, power laws are typical signatures for complex systems in general and therefore also discovered for many observables associated with our galaxy. Understanding the origin of a given power law relationship is challenging because usually there are various models which produce the same result. In order to rule out a particular model one could therefore consider the implications it has on other observables. Further research in this direction would allow for a better understanding and modeling of the galaxy as a dynamical and self-regulating system. Conceptually this could be understood as a transition from doing galactic architecture to doing galactic ecology.

Bibliography

Ackermann, M. et al. (2013). In: *Science* 339.6121, pp. 807–811. DOI: `10.1126/science.1231160`.

Aguilar, M. et al. (2015). In: *Phys. Rev. Lett.* 114.17, p. 171103. DOI: `10.1103/PhysRevLett.114.171103`.

— (2016). In: *Phys. Rev. Lett.* 117.23, p. 231102. DOI: `10.1103/PhysRevLett.117.231102`.

— (2017). In: *Phys. Rev. Lett.* 119.25, p. 251101. DOI: `10.1103/PhysRevLett.119.251101`.

— (2018). In: *Phys. Rev. Lett.* 120.2, p. 021101. DOI: `10.1103/PhysRevLett.120.021101`.

— (2020). In: *Phys. Rev. Lett.* 124.21, p. 211102. DOI: `10.1103/PhysRevLett.124.211102`.

— (2021a). In: *Phys. Rev. Lett.* 126.8, p. 81102. DOI: `10.1103/PhysRevLett.126.081102`.

— (2021b). In: *Phys. Rev. Lett.* 126.4, p. 41104. DOI: `10.1103/PhysRevLett.126.041104`.

Aharonian, F. et al. (2022). In: *Science* 376.6588, pp. 77–80. DOI: `10.1126/science.abn0567`.

Amato, Elena and Pasquale Blasi (2018). In: *Adv. Sp. Res.* 62.10, pp. 2731–2749. DOI: `10.1016/J.ASR.2017.04.019`.

Amato, Elena and Sabrina Casanova (2021). In: *J. Plasma Phys.* Pp. 1–32. DOI: `10.1017/S0022377821000064`.

Arens, Tilo et al., eds. (2010). *Mathematik.* 2., korrigierter Nachdr. Spektrum, Akad. Verl. ISBN: 978-3-8274-1758-9.

Armstrong, J. W. et al. (1981). In: *Nature* 291.5816, pp. 561–564. DOI: `10.1038/291561a0`.

Armstrong, J. W. et al. (1995). In: *ApJ* 443.1, pp. 209–221. DOI: `10.1086/175515`.

Bacchini, Cecilia et al. (2019). In: *A&A* 632, A127. DOI: `10.1051/0004-6361/201936559`.

— (2020). In: *A&A* 641, A70. DOI: `10.1051/0004-6361/202038223`.

Ballesteros-Paredes, Javier et al. (2011). In: *MNRAS* 411.1, pp. 65–70. DOI: `10.1111/j.1365-2966.2010.17657.x`.

Ballesteros-Paredes, Javier et al. (2018). In: *MNRAS* 479, pp. 2112–2125. DOI: `10.1093/mnras/stz1384`.

Ballesteros-Paredes, Javier et al. (2020). In: *Space Sci. Rev.* 216.5, p. 76. DOI: `10.1007/s11214-020-00698-3`.

Bartko, H. et al. (2010). In: *ApJ* 708.1, pp. 834–840. DOI: `10.1088/0004-637X/708/1/834`.

Bastian, Nate et al. (2010). In: *ARA&A* 48, pp. 339–389. DOI: `10.1146/annurev-astro-082708-101642`.

Basu, Aritra et al. (2017). In: *MNRAS* 471.1, pp. 337–354. DOI: `10.1093/mnras/stx1567`.

Batchelor, G. K. (1950). In: *Proc. R. Soc. Lond. A* 201.1066, pp. 405–416. DOI: `10.1098/rspa.1950.0069`.

Beattie, James R et al. (2019). In: *MNRAS* 487, pp. 2070–2081. DOI: `10.1093/mnras/stz1416`.

Beck, C (2004). In: *Phys. A: Stat. Mech. Appl.* 331.1-2, pp. 173–181. DOI: `10.1016/j.physa.2003.09.025`.

— (2009). In: *Eur. Phys. J. A* 40.3, p. 267. DOI: `10.1140/epja/i2009-10792-7`.

Beck, C and E G D Cohen (2003). In: *Phys. A: Stat. Mech. Appl.* 322, pp. 267–275. DOI: `10.1016/S0378-4371(03)00019-0`.

Beck, Rainer (2012). In: *Space Sci. Rev.* 166.1-4, pp. 215–230. DOI: `10.1007/s11214-011-9782-z`.

Beck, Rainer et al. (2020). In: *Galaxies* 8, p. 4. DOI: `10.3390/galaxies8010004`.

Becker Tjus, Julia and Lukas Merten (2020). In: *Phys. Rep.* 872, pp. 1–98. DOI: `10.1016/j.physrep.2020.05.002`.

Bell, A. R. (1978). In: *MNRAS* 182, pp. 147–156. DOI: `10.1093/mnras/182.2.147`.

— (2004). In: *Monthly Notices of the Royal Astronomical Society* 353.2, pp. 550–558. DOI: `10.1111/j.1365-2966.2004.08097.x`.

Bell, Eric F. (2003). In: *ApJ* 586, pp. 794–813. DOI: `10.1086/367829`.

Beresnyak, Andrey (2019). In: *Living Rev. Comput. Astrophys.* 5.1, p. 2. DOI: `10.1007/s41115-019-0005-8`.

Berezhko, E. G. et al. (2003). In: *Astronomy & Astrophysics* 412.1, pp. L11–L14. DOI: `10.1051/0004-6361:20031667`.

Bestehorn, Michael (2006). *Hydrodynamik und Strukturbildung: mit einer kurzen Einführung in die Kontinuumsmechanik.* Springer-Lehrbuch. Springer. 392 pp. ISBN: 978-3-540-33796-6.

Bigiel, F. et al. (2008). In: *AJ* 136.6, pp. 2846–2871. DOI: `10.1088/0004-6256/136/6/2846`.

Binggeli, Bruno and Tatjana Hascher (2007). In: *Publications of the Astronomical Society of the Pacific* 119.856, pp. 592–604. DOI: `10.1086/519533`.

Binney, James and Scott Tremaine (2011). *Galactic dynamics: second edition.* Princeton university press. ISBN: 1400828724.

Blandford, Roger D and James P Ostriker (1978). In: *ApJ* 221, pp. L29–L32. DOI: `10.1086/182658`.

Blasi, Pasquale (2019a). In: *Nuovo Cim. Riv. Ser.* 42.12, pp. 549–600. DOI: `10.1393/ncr/i2019-10166-0`.

— (2019b). In: *Galaxies* 7.2. DOI: `10.3390/galaxies7020064`.

Boschini, M. J. et al. (2017). In: *ApJ* 840.2, p. 115. DOI: `10.3847/1538-4357/aa6e4f`.

Boschini, M. J. et al. (2018). In: *ApJ* 858.1, p. 61. DOI: `10.3847/1538-4357/aabc54`.

Boschini, M. J. et al. (2020). In: *ApJ* 889.2, p. 167. DOI: `10.3847/1538-4357/ab64f1`.

Boulanger, F. and M. Perault (1988). In: *ApJ* 330, p. 964. DOI: `10.1086/166526`.

Brandenburg, A. and A. Lazarian (2013). In: *Space Sci. Rev.* 178, pp. 163–200. DOI: `10.1007/s11214-013-0009-3`.

Brandenburg, Axel and Kandaswamy Subramanian (2005). In: *Physics Reports* 417.1-4, pp. 1–209. DOI: `10.1016/j.physrep.2005.06.005`.

Broniowski, Wojciech et al. (2004). In: *Phys. Rev. D* 70.11, p. 117503. DOI: 10. 1103/PhysRevD.70.117503.

Bronstein, I N et al. (1977). *Taschenbuch Der Mathematik*. 6th ed. Verlag Harri Deutsch. ISBN: 3-8171-2006-0.

Cappellari, Michele et al. (2012). In: *Nature* 484.7395, pp. 485–488. DOI: 10.1038/ nature10972.

Chabrier, Gilles (2003). In: *Publ. Astron. Soc. Pacific* 115.809, pp. 763–795. DOI: 10.1086/376392.

Chacón-Acosta, Guillermo et al. (2010). In: *Phys. Rev. E* 81.2, p. 21126. DOI: 10. 1103/PhysRevE.81.021126.

Chamandy, Luke et al. (2016). In: *ApJ* 833.1, p. 43. DOI: 10.3847/1538-4357/ 833/1/43.

Chepurnov, A. and A. Lazarian (2010). In: *ApJ* 710.1, pp. 853–858. DOI: 10.1088/ 0004-637X/710/1/853.

Chevance, Mélanie et al. (2020). In: *Space Sci. Rev.* 216.4. DOI: 10.1007/s11214- 020-00674-x.

Chomiuk, Laura and Matthew S. Povich (2011). In: *AJ* 142.6, 197, p. 197. DOI: 10.1088/0004-6256/142/6/197.

Connell, J. J. (1998). In: *ApJ* 501.1, pp. L59–L62. DOI: 10.1086/311437.

Cummings, A. C. et al. (2016). In: *ApJ* 831.1, p. 18. DOI: 10.3847/0004-637X/ 831/1/18.

Davidzon, I. et al. (2017). In: *A&A* 605, A70. DOI: 10.1051/0004-6361/201730419.

De los Reyes, Mithi A. C. and Robert C. Kennicutt (2019). In: *ApJ* 872.1, p. 16. DOI: 10.3847/1538-4357/aafa82.

De Jong, T. et al. (1985). In: *A&A* 147, pp. L6–L9.

Delvecchio, I. et al. (2021). In: *A&A* 647, A123.

Diesing, Rebecca and Damiano Caprioli (2021). In: *ApJ* 922.1, p. 1. DOI: 10.3847/ 1538-4357/ac22fe.

Dobbs, C. L. et al. (2011). In: *MNRAS* 413, pp. 2935–2942.

Dokkum, Pieter G. van and Charlie Conroy (2010). In: *Nature* 468.7326, pp. 940– 942. DOI: 10.1038/nature09578.

Dombre, Thierry et al. (1986). In: *Journal of Fluid Mechanics* 167, pp. 353–391. DOI: 10.1017/S0022112086002859.

Draine, Bruce T (2010). *Physics of the interstellar and intergalactic medium*. Vol. 19. Princeton University Press. ISBN: 1400839084.

Dumas, G. et al. (2011). In: *AJ* 141, p. 41. DOI: 10.1088/0004-6256/141/2/41.

Elmegreen, Bruce G (1997). In: *ApJ* 486.2, p. 944. DOI: 10.1086/304562.

Elmegreen, Bruce G. and Andreas Burkert (2010). In: *ApJ* 712.1, pp. 294–302. DOI: 10.1088/0004-637X/712/1/294.

Elmegreen, Bruce G. and John Scalo (2004). In: *ARA&A* 42.1, pp. 211–273. DOI: 10.1146/annurev.astro.41.011802.094859.

Elmegreen, Bruce G. et al. (2022). In: *ApJ* 928.2, p. 143. DOI: 10.3847/1538- 4357/ac559c.

Evans II, Neal J. et al. (2021). In: *ApJ* 920.2, p. 126. DOI: 10.3847/1538-4357/ ac1425.

Evans, Neal J. et al. (2022). In: *ApJLetters* 929.1, p. L18. DOI: 10.3847/2041- 8213/ac6427.

Everall, Andrew et al. (2022). In: *MNRAS* 511.3, pp. 3863–3880. DOI: 10.1093/ mnras/stac305.

Evoli, Carmelo et al. (2020). In: *Phys. Rev. D* 101.2, p. 023013. DOI: `10.1103/PhysRevD.101.023013`.

Fermi, Enrico (1949). In: *Phys. Rev.* 75.8, p. 1169. DOI: `10.1103/PhysRev.75.1169`.

Ferrer i Cancho, R. (2005). In: *EPJ B* 44.2, pp. 249–257. DOI: `10.1140/epjb/e2005-00121-8`.

Ferrière, K (2001). In: *Rev. Mod. Phys.* 73.4, pp. 1031–1066. DOI: `10.1103/RevModPhys.73.1031`.

— (2019). In: *Plasma Phys. Control. Fusion* 62.1, p. 14014. DOI: `10.1088/1361-6587/ab49eb`.

Fletcher, A. (2010). In: *The Dynamic Interstellar Medium: A Celebration of the Canadian Galactic Plane Survey*. Vol. 438. Astronomical Society of the Pacific Conference Series, p. 197.

Frisch, U (1995). *Turbulence: the legacy of A. N. Kolmogorov*. Cambridge University Press. DOI: `10.1017/CBO9781139170666`.

Gabici, Stefano et al. (2019). In: *Int. J. Mod. Phys. D* 28.15, p. 1930022. DOI: `10.1142/s0218271819300222`.

Gaensler, B M et al. (2011). In: *Nature* 478.7368, pp. 214–217. DOI: `10.1038/nature10446`.

Gaisser, Thomas K. et al. (2016). *Cosmic Rays and Particle Physics*. Cambridge University Press. ISBN: 9781139192194. DOI: `10.1017/CBO9781139192194`.

Geha, Marla et al. (2013). In: *ApJ* 771.1, p. 29. DOI: `10.1088/0004-637X/771/1/29`.

Génolini, Yoann et al. (2018). In: *Phys. Rev. C* 98.3, p. 034611. DOI: `10.1103/PhysRevC.98.034611`.

Girichidis, Philipp et al. (2020). In: *Space Sci. Rev.* 216.4, p. 68. DOI: `10.1007/s11214-020-00693-8`.

Goldreich, P and S Sridhar (1995). In: *ApJ* 438, p. 763. DOI: `10.1086/175121`.

Gressel, O. et al. (2008). In: *A&A* 486.3, pp. L35–L38. DOI: `10.1051/0004-6361:200810195`.

Großmann, Siegfried (2011). In: *Physik im 21. Jahrhundert: Essays zum Stand der Physik*, pp. 47–108. ISBN: 978-3-642-05191-3. DOI: `10.1007/978-3-642-05191-3_2`.

Guszejnov, D and P F Hopkins (2015). In: *MNRAS* 450.4, pp. 4137–4149. DOI: `10.1093/mnras/stv872`.

Guszejnov, Dávid and Philip F Hopkins (2016). In: *MNRAS* 459.1, pp. 9–20. DOI: `10.1093/mnras/stw619`.

Guszejnov, David et al. (2020). In: *MNRAS* 496.4, pp. 5072–5088. DOI: `10.1093/mnras/staa1883`.

Guszejnov, Dávid et al. (2018). In: *MNRAS* 477.4, pp. 5139–5149. DOI: `10.1093/mnras/sty920`.

Guszejnov, D et al. (2019). In: *MNRAS* 485.4, pp. 4852–4862. DOI: `10.1093/mnras/stz736`.

Hagedorn, Rolf (1965). In: *Nuovo Cimento, Suppl.* 3.CERN-TH-520, pp. 147–186.

Hanasz, Michał et al. (2021). In: *Liv. Rev. in Comput. Astroph.* 7, p. 2. DOI: `10.1007/s41115-021-00011-1`.

Hatton et al. (2021). In: *Sci. Adv.* 7.46. DOI: `10.5281/ZENODO.5520055`.

Haverkorn, M et al. (2008). In: *ApJ* 680.1, p. 362. DOI: `10.1086/587165`.

Heesen, V. et al. (2022). In: DOI: `10.48550/arXiv.2204.00635`.

Heesen, Volker et al. (2014). In: *Astron. J.* 147.5. DOI: `10.1088/0004-6256/147/5/103`.

Helou, G. et al. (1985). In: *ApJ* 298, pp. L7–L11. DOI: 10.1086/184556.

Hennebelle, Patrick and Gilles Chabrier (2008). In: *ApJ* 684.1, pp. 395–410. DOI: 10.1086/589916.

Henriksen, Richard N (2015). *Scale Invariance: Self-Similarity of the Physical World*. John Wiley & Sons. ISBN: 9783527413355.

Heyer, Mark et al. (2009). In: *ApJ* 699, pp. 1092–1103. DOI: 10.1088/0004-637X/699/2/1092.

Hopkins, A. M. (2018). In: *Publ. Astron. Soc. Aust.* 35.39. DOI: 10.1017/pasa.2018.29.

Hopkins, Philip F (2012). In: *MNRAS* 423.3, pp. 2037–2044. DOI: 10.1111/j.1365-2966.2012.20731.x.

— (2013). In: *MNRAS* 430, pp. 1653–1693.

Hosek, Matthew W. et al. (2019). In: *ApJ* 870.1, p. 44. DOI: 10.3847/1538-4357/aaef90.

Jeans, James Hopwood (1902). In: *Philosophical Transactions of the Royal Society of London. Series A, Containing Papers of a Mathematical or Physical Character* 199.312-320, pp. 1–53.

Jüttner, Ferencz (1911). In: *Annalen der Physik* 339.5, pp. 856–882. DOI: 10.1002/andp.19113390503.

Kachelriess, M. and D.V. Semikoz (2019). In: *Prog. Part. Nucl. Phys.* 109, p. 103710. DOI: 10.1016/j.ppnp.2019.07.002.

Kennicutt, R. (1998). In: *ApJ* 498, pp. 541–552. DOI: 10.1086/305588.

Kolmogorov, A N (1941). In: *Akademiia Nauk SSSR Doklady* 30, pp. 301–305.

Kroupa, Pavel et al. (2013). In: *Planets, Stars Stellar Syst. Vol. 5 Galact. Struct. Stellar Popul.* Pp. 115–242. DOI: 10.1007/978-94-007-5612-0_4.

Kruijssen, J. M. Diederik et al. (2019). In: *Nature* 569.7757, pp. 519–522. DOI: 10.1038/s41586-019-1194-3.

Krumholz, Mark R. (2014). In: *Phys. Rep.* 539.2, pp. 49–134. DOI: 10.1016/j.physrep.2014.02.001.

Krumholz, Mark R. and Christoph Federrath (2019). In: *Frontiers in Astronomy and Space Sciences* 6, p. 7. DOI: 10.3389/fspas.2019.00007.

Krumholz, Mark R. et al. (2007). In: *ApJ* 656.2, pp. 959–979. DOI: 10.1086/510664.

Krumholz, Mark R. et al. (2012). In: *ApJ* 745.1, p. 69. DOI: 10.1088/0004-637X/745/1/69.

Kulsrud, Russell M and Ellen G Zweibel (2008). In: *Reports on Progress in Physics* 71.4, p. 046901. DOI: 10.1088/0034-4885/71/4/046901.

Lacki, Brian C et al. (2010). In: *ApJ* 717.1, pp. 1–28. DOI: 10.1088/0004-637X/717/1/1.

Landau, L. D. and E. M. Lifschitz (1979). *Lehrbuch Der Theoretischen Physik - Band V, Statistische Physik Teil 1*. Vol. V. Akademie Verlag Berlin. ISBN: 3-05-500069-2.

— (1986). *Hydrodynamik*. Verlag Harri Deutsch. ISBN: 978-3-8171-1331-6.

Lang, Christian B. and Norbert Pucker (2010). *Mathematische Methoden in der Physik*. 2. Aufl., korr. Nachdr. Spektrum Akademischer Verl. 713 pp. ISBN: 978-3-8274-1558-5.

Larson, R. B. (1981). In: *MNRAS* 194.4, pp. 809–826. DOI: 10.1093/mnras/194.4.809.

Lee, K H and L C Lee (2019). In: *Nat. Astron.* 3.2, pp. 154–159. DOI: 10.1038/s41550-018-0650-6.

Lee, Yueh-Ning et al. (2020). In: *Space Sci. Rev.* 216.4, p. 70. DOI: 10.1007/s11214-020-00699-2.

Leroy, Adam K. et al. (2008). In: *AJ* 136.6, pp. 2782–2845. DOI: 10.1088/0004-6256/136/6/2782.

Lu, J. R. et al. (2013). In: *ApJ* 764.2, p. 155. DOI: 10.1088/0004-637X/764/2/155.

Mac Low, Mordecai-Mark (1999). In: *ApJ* 524.1, pp. 169–178. DOI: 10.1086/307784.

Mac Low, Mordecai-Mark and Ralf S. Klessen (2004). In: *Rev. Mod. Phys.* 76.1, pp. 125–194. DOI: 10.1103/RevModPhys.76.125.

Malkov, M A and L O C Drury (2001). In: *Reports Prog. Phys.* 64.4, pp. 429–481. DOI: 10.1088/0034-4885/64/4/201.

Mandelbrot, Benoit (1967). In: *Science* 156.3775, pp. 636–638. DOI: 10.1126/science.156.3775.636.

Marks, Michael et al. (2012). In: *MNRAS* 422.3, pp. 2246–2254. DOI: 10.1111/j.1365-2966.2012.20767.x.

Mathew, Sajay Sunny and Christoph Federrath (2021). In: *MNRAS* 507.2, pp. 2448–2467. DOI: 10.1093/mnras/stab2338.

McKee, Christopher F. and Eve C. Ostriker (2007). In: *ARA&A* 45.1, pp. 565–687. DOI: 10.1146/annurev.astro.45.051806.110602.

McKee, Christopher F and Jeremiah P Ostriker (1977). In: *ApJ* 218, pp. 148–169. DOI: 10.1086/155667.

McMillan, Paul J. (2017). In: *MNRAS* 465.1, pp. 76–94. DOI: 10.1093/mnras/stw2759.

Mogotsi, K. M. et al. (2016). In: *AJ* 151.1, p. 15. DOI: 10.3847/0004-6256/151/1/15.

Molnar, L. A. et al. (1995). In: *ApJ* 438, p. 708. DOI: 10.1086/175115.

Moraal, H. (2013). In: *Space Sci. Rev.* 176.1, pp. 299–319. DOI: 10.1007/s11214-011-9819-3.

— (2014). In: *Astropart. Phys.* 53, pp. 175–185. DOI: 10.1016/J.ASTROPARTPHYS.2013.03.002.

Morlino, G and D Caprioli (2012). In: *A&A* 538, A81. DOI: 10.1051/0004-6361/201117855.

Murphy, E J et al. (2006). In: *ApJ* 638.1, pp. 157–175. DOI: 10.1086/498636.

Nakamura, Fumitaka and Zhi-Yun Li (2008). In: *ApJ* 687.1, p. 354. DOI: 10.1086/591641.

Niklas, S. (1997). In: *A&A* 322, pp. 29–37.

Niklas, S and R Beck (1997). In: *A&A* 320, pp. 54–64.

Norman, Colin A. and Andrea Ferrara (1996). In: *ApJ* 467, p. 280. DOI: 10.1086/177603.

Offner, S. S. R. et al. (2014). In: *Protostars and Planets VI*, p. 53. DOI: 10.2458/azu_uapress_9780816531240-ch003.

Oldham, Lindsay and Matthew Auger (2018). In: *MNRAS* 474.3, pp. 4169–4185. DOI: 10.1093/mnras/stx2969.

Padoan, Paolo and Åke Nordlund (2002). In: *ApJ* 576.2, pp. 870–879. DOI: 10.1086/341790.

Padoan, Paolo et al. (2016). In: *ApJ* 822.1, p. 11. DOI: 10.3847/0004-637X/822/1/11.

Paladino, R. et al. (2006). In: *A&A* 456, pp. 847–859. DOI: 10.1051/0004-6361:20065002.

Petter, Grayson C et al. (2020). In: *ApJ* 901.2, p. 138. DOI: 10.3847/1538-4357/
    abb19d.
Press, William H. and Paul Schechter (1974). In: *ApJ* 187, p. 425. DOI: 10.1086/
    152650.
Rafelski, Johann and Torleif Ericson (2016). In: *Melting Hadrons, Boiling Quarks -
    From Hagedorn Temperature to Ultra-Relativistic Heavy-Ion Collisions at CERN:
    With a Tribute to Rolf Hagedorn*, pp. 41–48. DOI: 10.1007/978-3-319-17545-
    4_6.
Recchia, S and S Gabici (2018). In: *MNRAS Lett.* 474.1, pp. L42–L46. DOI: 10.
    1093/mnrasl/slx191.
Renaud, Florent et al. (2014). In: *MNRAS* 442.1, pp. L33–L37. DOI: 10.1093/
    mnrasl/slu050.
Ressler, Sean M. et al. (2014). In: *ApJ* 790.2, p. 85. DOI: 10.1088/0004-637x/790/
    2/85.
Reynolds, Stephen P. (2008). In: *ARA&A* 46, pp. 89–126. DOI: 10.1146/annurev.
    astro.46.060407.145237.
Richard, Denis and Jean-Paul Zahn (1999). In: *A&A* 347, pp. 734–738.
Richardson, Lewis Fry (2007). *Weather prediction by numerical process*. 2nd edition.
    Cambridge university press. ISBN: 0521680441.
Salpeter, Edwin E. (1955). In: *ApJ* 121, p. 161. DOI: 10.1086/145971.
Scalo, John (1990). In: *Phys. Process. Fragm. Star Form.* Vol. 162, pp. 151–176.
    DOI: 10.1007/978-94-009-0605-1_12.
Scalo, John M (1987). In: *Interstellar Process.* Pp. 349–392.
Schleicher, Dominik R. G. and Rainer Beck (2013). In: *A&A* 556, A142. DOI: 10.
    1051/0004-6361/201321707.
Schlickeiser, R (2002). *Cosmicray and Astrophysics*. Springer. ISBN: 978-3-642-08573-
    4. DOI: 10.1007/978-3-662-04814-6.
Schmidt, Maarten (1959). In: *ApJ* 129, p. 243.
Schober, J. et al. (2013). In: *A&A* 560, A87. DOI: 10.1051/0004-6361/201322185.
— (2016). In: *ApJ* 827.2, p. 109.
Schroer, Benedikt et al. (2021). In: *arXiv e-prints*, arXiv:2102.12576.
Schure, K. M. et al. (2012). In: *Space Sci. Rev.* 173, pp. 491–519. DOI: 10.1007/
    s11214-012-9871-7.
Semelin, B. and F. Combes (2000). In: *A&A* 360, pp. 1096–1106.
Seta, Amit and Rainer Beck (2019). In: *Galaxies* 7.2. DOI: 10.3390/galaxies7020045.
Sharda, Piyush et al. (2022). In: *MNRAS* 509, pp. 2180–2193. DOI: 10.1093/mnras/
    stab3048.
Shore, Steven N (1992). *An introduction to astrophysical hydrodynamics*. San Diego:
    Academic Press. ISBN: 0126406707.
Shu, F. H. (1977). In: *ApJ* 214, pp. 488–497. DOI: 10.1086/155274.
Shustov, B. M. and A. V. Tutukov (2018). In: *Astronomy Reports* 62.11, pp. 724–
    732. DOI: 10.1134/S1063772918110070.
Smith, Russell J. (2020). In: *ARA&A* 58.1, pp. 577–615. DOI: 10.1146/annurev-
    astro-032620-020217.
Smolla, M et al. (2020). In: *New J. Phys.* 22.9, p. 093002. DOI: 10.1088/1367-
    2630/abaa03.
Sornette, Didier (2004). *Critical Phenomena in Natural Sciences: Chaos, Fractals,
    Selforganization, and Disorder: Concepts and Tools*. 2nd ed. Springer Series in
    Synergetics. Springer. 528 pp. ISBN: 978-3-540-40754-6.

Sornette, Didier et al. (1996). In: *J. Geophys. Res. Solid Earth* 101.B6, pp. 13883–13893. DOI: 10.1029/96JB00177.

Spangler, Steven R and Carl R Gwinn (1990). In: *ApJ* 353, p. L29. DOI: 10.1086/185700.

Stinebring, Dan et al. (2019). In: DOI: 10.48550/arXiv.1903.07370.

Stone, Edward C. et al. (2019). In: *Nat. Astron.* 3.11, pp. 1013–1018. DOI: 10.1038/s41550-019-0928-3.

Strong, Andrew W. et al. (2007). In: *Annu. Rev. Nucl. Part. Sci.* 57.1, pp. 285–327. DOI: 10.1146/annurev.nucl.57.090506.123011.

Sun, Jiayi et al. (2020). In: *ApJ* 892.2, p. 148. DOI: 10.3847/1538-4357/ab781c.

Syrovat-Skii, S. I. (1961). In: *Soviet Physics JETP* 13.6, pp. 1257–1260.

Tabatabaei, F. S. et al. (2013). In: *A&A* 552, A19. DOI: 10.1051/0004-6361/201220249.

Tabatabaei, F. S. et al. (2017). In: *ApJ* 836.2, p. 185. DOI: 10.3847/1538-4357/836/2/185.

Tatischeff, Vincent and Stefano Gabici (2018). In: *Annu. Rev. Nucl. Part. Sci.* 68.1, pp. 377–404. DOI: 10.1146/annurev-nucl-101917-021151.

Tsallis, Constantino et al. (2004). In: *Astrophys. Space Sci.* 290.3, pp. 259–274. DOI: 10.1023/B:ASTR.0000032528.99179.4f.

Tutukov, A. V. and B. M. Shustov (2020). In: *Astrophysics* 63.4, pp. 552–565. DOI: 10.1007/s10511-020-09658-9.

Voelk, H. J. (1989). In: *A&A* 218, pp. 67–70.

Wang, Jianling et al. (2022). In: *MNRAS* 510.2, pp. 2242–2260. DOI: 10.1093/mnras/stab3258.

Whitworth, David J. et al. (2022). In: *MNRAS* 510, pp. 4146–4165. DOI: 10.1093/mnras/stab3622.

Wilk, Grzegorz and Zbigniew Wlodarczyk (2017). In: *Entropy* 19.12, p. 670. DOI: 10.3390/e19120670.

Wong, Cheuk Yin et al. (2015). In: *Phys. Rev. D - Part. Fields, Gravit. Cosmol.* 91.11, pp. 1–16. DOI: 10.1103/PhysRevD.91.114027.

Woosley, Stan and Thomas Janka (2005). In: *Nature Physics* 1.3, pp. 147–154.

Xu, S and A Lazarian (2016). In: *ApJ* 833.2, p. 215.

— (2022a). In: *ApJ* 927.1, p. 94. DOI: 10.3847/1538-4357/ac4dfd.

— (2022b). In: 925.1, p. 48. DOI: 10.3847/1538-4357/ac3824.

Xu, S and B Zhang (2020a). In: *ApJ* 905.2, p. 159. DOI: 10.3847/1538-4357/abc69f.

— (2020b). In: *ApJ Letters* 898.2, p. L48. DOI: 10.3847/2041-8213/aba760.

Yalcin, G C and C Beck (2018). In: *Sci. Rep.* 8.1, p. 1764. DOI: 10.1038/s41598-018-20036-6.

Yun, Min S. et al. (2001). In: *ApJ* 554, pp. 803–822. DOI: 10.1086/323145.

Danke

Diese Arbeit wurde zwar von mir alleine geschrieben, ist aber dennoch geprägt von einer Vielzahl von Menschen. Meine Eltern förderten meine Neugierde von Anfang an und beantworteten mir die ersten großen Fragen, wie z.B.: „Wie schnell fahren wir gerade?" oder „Ist eine Ecke wirklich eckig? Oder sind Ecken eigentlich rund wenn man ganz genau hinsieht?". Ich bin sehr dankbar, dass sie mich und meine Fragen schon immer ernst genommen haben und mich mein Leben lang sehr geduldig unterstützt haben und mir den Freiraum gegeben haben, um meinen Leidenschaften nach zu gehen.

Ohne meinen Doktorvater wäre ich vielleicht einen ganz anderen Weg gegangen. Der Physikunterricht in der Schule hat mich eigentlich nicht so begeistert, außer die Unterrichtsstunden in denen Alpha Centauri mit Harald Lesch lief. Das hat mich fasziniert und letztlich auch zum Physikstudium gebracht. Spätestens nach dem Master wollte ich dann allerdings raus aus dem akademischen Umfeld und mich aktiv für die Verbesserung unserer Welt einsetzen. Nun bin ich sehr dankbar, dass mich Harald für die Astrophysik und die Wissenschaft im Allgemeinen so begeistern konnte, dass ich heute überzeugt bin, dass ich mit der Vermittlung von Wissenschaft einen wertvollen Beitrag zu den Herausforderungen unserer Zeit leisten kann und dabei gleichzeitig auch noch meiner Neugierde weiter nachgehen darf.

Dankbar bin ich auch den tollen Menschen, die mich in der bisherigen Ausbildung begleitet haben. Mit Anna, Stephan und Felix zusammen hat das Studium einfach viel mehr Freude gemacht und manches Übungsblatt hätte ich ohne Felix vielleicht nie verstanden. An der Sternwarte denke ich vor allem an die vielen guten Gespräche mit Matthias, Marcel, Ludwig und Peter, der mich in seiner Rolle als Peter Python in die Welt des Programmierens eingeführt hat.

Ein besonderer Dank geht an meine Frau Mira. Während meiner vierjährigen Promotion war sie dreimal schwanger und hat unseren heute fast zweijährigen Sohn Pablo unzählige Male erklärt: „Papa muss arbeiten", damit ich auch Zuhause möglichst in Ruhe lesen und schreiben konnte. Mein Sohn Pablo hat mir geholfen in den vielen Pausen mit ihm gemeinsam das rationale Denken zu verwerfen und einfach nur den Moment zu erleben. Mira, Pablo und Kleini im Bauch, auch wenn es nicht immer einfach ist, Familie und Arbeit miteinander zu vereinen, ich bin so dankbar, dass wir gemeinsam durchs Leben gehen dürfen.

Letztlich ist diese Arbeit auch ein Produkt von knapp vierzehn Milliarden kosmischer Entwicklung. Durch unzählige Schritte der Evolution konnten wir Menschen und unsere Sprache entstehen, in der sich so eine Arbeit überhaupt erst formulieren lässt. Und auch in diesem Fall gilt: „Das Ganze ist mehr als die Summe seiner Teile".